



저작자표시-비영리-변경금지 2.0 대한민국

이용자는 아래의 조건을 따르는 경우에 한하여 자유롭게

- 이 저작물을 복제, 배포, 전송, 전시, 공연 및 방송할 수 있습니다.

다음과 같은 조건을 따라야 합니다:



저작자표시. 귀하는 원저작자를 표시하여야 합니다.



비영리. 귀하는 이 저작물을 영리 목적으로 이용할 수 없습니다.



변경금지. 귀하는 이 저작물을 개작, 변형 또는 가공할 수 없습니다.

- 귀하는, 이 저작물의 재이용이나 배포의 경우, 이 저작물에 적용된 이용허락조건을 명확하게 나타내어야 합니다.
- 저작권자로부터 별도의 허가를 받으면 이러한 조건들은 적용되지 않습니다.

저작권법에 따른 이용자의 권리는 위의 내용에 의하여 영향을 받지 않습니다.

이것은 [이용허락규약\(Legal Code\)](#)을 이해하기 쉽게 요약한 것입니다.

[Disclaimer](#)

Ph. D. DISSERTATION

**INVERTED POLYMER SOLAR CELLS
WITH METAL-DOPED OXIDE AS AN
ELECTRON EXTRACTION LAYER**

금속 도핑된 산화물을 전자추출층으로 이용한
역구조 고분자 태양전지 연구

BY

JUNYOUNG KIM

AUGUST 2014

DEPARTMENT OF ELECTRICAL ENGINEERING AND
COMPUTER SCIENCE
COLLEGE OF ENGINEERING
SEOUL NATIONAL UNIVERSITY

INVERTED POLYMER SOLAR CELLS WITH
METAL-DOPED OXIDE AS AN ELECTRON
EXTRACTION LAYER

금속 도핑된 산화물을 전자추출층으로 이용한
역구조 고분자 태양전지 연구

지도교수 이 창 희

이 논문을 공학박사 학위논문으로 제출함

2014 년 8 월

서울대학교 대학원

전기컴퓨터 공학부

김 준 영

김준영의 공학박사 학위논문을 인준함

2014 년 8 월

위 원 장 : _____ (인)
부위원장 : _____ (인)
위 원 : _____ (인)
위 원 : _____ (인)
위 원 : _____ (인)

Abstract

INVERTED POLYMER SOLAR CELLS WITH METAL-DOPED OXIDE AS AN ELECTRON EXTRACTION LAYER

JUNYOUNG KIM

**DEPARTMENT OF ELECTRICAL ENGINEERING
AND COMPUTER SCIENCE
COLLEGE OF ENGINEERING
SEOUL NATIONAL UNIVERSITY**

Inverted structures of polymer solar cells have been developed in recent years because of their superior device stability and manufacturing compatibility. In the inverted structure, a high work function metal such as Al, Ag and Au is used as hole collecting electrode, while several n-type interfacial layer such as organic layer, Cs_2CO_3 , TiO_2 and ZnO is used as a buffer layer. These buffer layers also help to redistribute the light intensity inside the devices and to protect the active layer from

degradation by oxygen or moisture. Among the many n-type electron extraction layer used in inverted devices, the metal oxide such as ZnO and TiO₂ is a promising candidate because of its relatively high electron mobility, conductivity, high transparency, environmental stability and easy to make solution and thin films.

It is well known that the physical characteristics of metal oxide thin films depend on the doping and a systematic study of the doping effect on the physical characteristics is always interesting. The doping of semiconductors with various elements is known to greatly affect many of the basic physical properties of the semiconductor, including its electrical, optical, morphological and structural properties, which are all crucial for most of the practical applications.

In this thesis, in order to improve the device performance of inverted polymer solar cells we applied metal doped oxide as an electron extraction layer. In, Al and Ga doped ZnO nanocrystalline thin films with different In, Al and Ga concentrations as well as amorphous IGZO thin films have been synthesized by the sol-gel method. The effect of In, Al, Ga doped ZnO and IGZO on the structural, morphological, optical and electrical properties have been systematically investigated. The inverted polymer solar cell with structure of ITO / In, Al, Ga doped ZnO and IGZO / Polymer:PC₇₀BM / MoO₃ / Al have been fabricated and analyzed the relationship of device performance depend on metal doping. As a result, inverted polymer solar cells with 6.74 at.% In doped ZnO, 5.83 at.% Al doped ZnO, 5.03 at.% Ga doped ZnO films and IGZO (1:1:2.5 with the ratio of In:Ga:Zn) show the high power conversion efficiency of 8.53 %, 8.67 %, 8.72 % and 9.60 % based on PTB7-Th:PC₇₀BM active layer. These efficiency values are almost 20 ~ 32 % improved as compared to ZnO based device (6.56 %). The improvement of power conversion efficiency may attributed to the enhanced optical, morphological and electrical properties. Moreover, the injection impedance values and activation energy of In, Al,

Ga doped ZnO and IGZO were lower and recombination coefficient was higher than those of ZnO based device, which indicates that electron extraction properties are enhanced.

Beside, inverted polymer solar cell containing TiO₂ and metal (Al, In, Ga, Sn and Zn) doped TiO₂ as an electron extraction layer with structure of ITO / TiO₂ or doped TiO₂ / PTB7:PC₇₀BM / MoO₃ / Al have been fabricated and analyzed about the relationship of device performance depend on metal doping. The power conversion efficiencies of inverted polymer solar cells with Al, In, Ga, Sn and Zn doped TiO₂ (~1 at.% doping concentration) device are 7.59 ~ 7.87 %, which is higher than that of TiO₂ based device (6.70 %). The results clearly demonstrate that significant improvement in power conversion efficiency can be obtained by incorporating Al, In, Ga, Sn and Zn into the TiO₂ films. However the efficiency of 7.59 ~ 7.87 % is still low as compared to doped ZnO or IGZO based devices. These results are because the electrical properties of TiO₂ such as mobility and conductivity are lower than ZnO. So, in order to improve power conversion efficiency of TiO₂ based devices, we applied polyethylene oxide (PEO) modified TiO₂ and Zn doped TiO₂. It is found that PEO modification to the TiO₂ or Zn doped TiO₂ surface can effectively passivate the surface traps present in TiO₂ or Zn doped TiO₂, and suppress the recombination loss of carriers, reduce the series resistance and improve the electrical coupling of TiO₂/active layer or Zn doped TiO₂/active layer. For PEO modified TiO₂ and PEO modified Zn doped TiO₂ based inverted polymer solar cells, the power conversion efficiencies are significantly improved from the reference 6.98% and 7.51% to 7.67% and 8.10%.

This thesis demonstrates the practical approaches to enhance power conversion efficiency of inverted polymer solar cells, covering the electron extraction layer, suitable device structure, and processing method. This approach is believed that

could be applied not only other type of solar cell such as solar cells, such as polymer-NC hybrid solar cells, dye-sensitized solar cells and perovskite solar cells but also other optoelectronic devices.

Keywords: Polymer solar cell, Inverted structure, ZnO, TiO₂, Doping, Electron extraction layer, PCDTBT, PTB7, PTB7-Th, PC₇₀BM

Student Number: 2010-30979

Contents

Abstract	i
Contents	v
List of Figures	xi
List of Tables	xviii
Chapter 1	1
1.1 Overview of Organic Solar Cells	3
1.2 Electron Extraction Layer of Inverted Polymer Solar Cells.....	5
1.3 Metal Doped Oxide as an Electron Extraction Layer...	9
1.4 Outline of Thesis.....	11
Chapter 2	12

2.1 Principles of Organic Solar Cells	12
2.1.1 Operation Principle.....	12
2.1.2 Basic solar cell Performance Parameters	13
2.2 Materials and Solution	16
2.2.1 Organic Materials	16
2.2.2 Making of Metal Oxide Precursor Solution	17
2.2.3 Making of Organic Solution.....	20
2.3 Device and Thin Film Fabrication	21
2.3.1 Device Fabrication of Polymer Solar Cells.....	21
2.3.2 Thin Film Fabrication	22
2.4 Device and Thin Film Characterization Methods.....	23
2.4.1 Device Characterization Methods.....	23
2.4.2 Thin Film Characterization Methods.....	23
Chapter 3	25
3.1 Inverted Polymer Solar Cells with In doped ZnO as an Electron Extraction Layer	27
3.1.1 Structural and Morphological Properties of In doped ZnO..	27
3.1.2 Optical Properties of In doped ZnO	35

3.1.3 Electrical Properties of In-doped ZnO	37
3.1.4 Device Characteristics with In doped ZnO	39
3.2 Inverted Polymer Solar Cells with Al doped ZnO as an Electron Extraction Layer	42
3.2.1 Structural and Morphological Properties of Al-doped ZnO	42
3.2.2 Electrical Properties of Al doped ZnO	45
3.2.3 Device Characteristics with Al doped ZnO	47
3.3 Inverted Polymer Solar Cells with Ga Doped ZnO as an Electron Extraction Layer	50
3.3.1 Optical Properties of Organic Materials and Ga doped ZnO.....	51
3.3.2 Electrical Properties of Ga doped ZnO	52
3.3.3 Device Characteristics with Ga doped ZnO.....	53
3.3.4 Structural and Morphological Properties of Ga doped ZnO	57
3.4 Inverted Polymer Solar Cells with Indium Gallium Zinc Oxide as an Electron Extraction Layer	64
3.4.1 Structural and Morphological Properties of IGZO	65
3.4.2 Electrical Properties of IGZO.....	68

3.4.3 Optical Properties of IGZO	69
3.4.4 Device Characteristics with IGZO.....	71
3.4.5 Light Intensity Dependence of Device Performance with IGZO	74
3.5 Inverted Polymer Solar Cells with Metal-Doping Dependent ZnO as an Electron Extraction Layer	76
3.5.1 Device Characteristics with Metal-Doping Dependent ZnO	76
3.5.2 Impedance Characteristics with Metal-Doping Dependent ZnO.....	80
3.5.3 Temperature and Light Intensity Characteristics with Metal-Doping Dependent ZnO.....	81
3.6 Summary	93
Chapter 4	95
4.1 Inverted Polymer Solar Cells with Al Doping Concentration of Al Doped TiO₂ as an Electron Extraction Layer	96
4.2 Inverted Polymer Solar Cells with Metal-Doping Dependent TiO₂ as an Electron Extraction Layer	98

4.2.1 Structural and Morphological Properties of Various Metal Doped TiO ₂	98
4.2.2 Electrical Properties of Metal Doped TiO ₂	103
4.2.3 Device Characteristics with Various Metal Doped TiO ₂	104
4.2.4 Temperature and Light Intensity Characteristics with Various Metal Doped TiO ₂	107
4.3 Inerted Polymer Solar Cells with Polyethylene Oxide (PEO) Modified TiO₂ as an Electron Extraction Layer .	111
4.3.1 Optical Properties of PEO Modified TiO ₂ and Zn doped TiO ₂	111
4.3.2 Electrical Properties of PEO modified TiO ₂ and Zn doped TiO ₂	115
4.3.3 Device Characteristics with PEO Modified TiO ₂ and Zn doped TiO ₂	116
4.3.4 Structural and Morphological Properties of PEO modified TiO ₂ and Zn doped TiO ₂	122
4.4 Summary	126
Chapter 5	127
Bibilography	130

Publication	143
한글초록	148

List of Figures

Figure 1.1 Projected non-hydropower renewable electricity generation, 2010 - 2035 (Source : U. S. Energy Information Administration (Feb 2012))...	2
Figure 1.2 Best research solar cell efficiencies record (Source : The National Center for Photovoltaics (NCPV) at NREL)	3
Figure 2.1 Working principles of organic solar cells.	13
Figure 2.2 Current density-voltage (J-V) curve of organic solar cell.	14
Figure 2.3 Chemical structure of used materials.	16
Figure 2.4 Device structure of inverted polymer solar cells.....	22
Figure 3.1 X-ray diffraction pattern of ZnO and In doped ZnO films.	27
Figure 3.2 FESEM images of (a) ZnO and In doped ZnO, (b) 1.98 at.% In, (c) 4.03 at.% In, (d) 6.74 at.% In, (e) 8.62 at.% In, (f) 10.48 at.% In.....	30
Figure 3.3 EDS spectra of (a) ZnO and In doped ZnO, (b) 1.98 at.% In, (c) 4.03 at.% In, (d) 6.74 at.% In, (e) 8.62 at.% In, (f) 10.48 at.% In.....	31
Figure 3.4 AFM images of (a) ZnO and In doped ZnO, (b) 1.98 at.% In, (c) 4.03 at.% In, (d) 6.74 at.% In, (e) 8.62 at.% In, (f) 10.48 at.% In.....	32
Figure 3.5 HRTEM, SAED images of (a, b, c) ZnO and (d, e, f) 6.74 at.% In doped ZnO.....	33
Figure 3.6 Optical absorption spectra of ZnO and In doped ZnO films.....	36
Figure 3.7 Plot of $(\alpha h\nu)^2$ versus $h\nu$ of ZnO and In doped ZnO films	36
Figure 3.8 Variation of resistivity and electron mobility of ZnO thin films with indium doping concentration.....	37

Figure 3.9 The current density-voltage (J-V) characteristics of the ZnO and In doped ZnO inverted polymer solar cells and (b) the IPCE spectra.....	41
Figure 3.10 X-ray diffraction patterns of ZnO and Al doped ZnO with different Al doping concentration.....	42
Figure 3.11 HRTEM images of (a, b, c) ZnO and (d, e, f) 5.83 at.% Al doped ZnO	44
Figure 3.12 Variation of resistivity and electron mobility of ZnO thin films with aluminum doping concentration.	45
Figure 3.13 (a) The density of states (DOS) for the Al doped ZnO with various Al concentration where the Fermi level is set to zero, (b) The sum of conduction bottom states in Al doped ZnO	46
Figure 3.14 (a) Current density-voltage characteristics, (b) IPCE spectra of the inverted polymer solar cell with the ZnO and Al doped ZnO with different Al doping concentration (c) J_{sc} and V_{oc} (d) FF and PCE as a function of Al doping concentration.....	48
Figure 3.15 Energy level diagrams of inverted polymer solar cells	51
Figure 3.16 Absorption spectra of (a) PCDTBT, PTB7, PC ₇₀ BM, and composite of PCDTBT:PC ₇₀ BM and PTB7:PC ₇₀ BM films (b) ZnO and Ga doped ZnO films with various Ga doping concentration	51
Figure 3.17 Variation of resistivity of ZnO films with Ga doping concentration	52
Figure 3.18 (a) J-V characteristics and (b) IPCE spectra of PCDTBT:PC ₇₀ BM devices (c) J-V characteristics and (d) IPCE spectra of PTB6:PC ₇₀ BM devices (e) dark J-V characteristics of PCDTBT:PC ₇₀ BM devices (f) dark J-V characteristics of PTB7:PC ₇₀ BM devices	56
Figure 3.19 FESEM images of (a) ZnO and Ga doped ZnO, (b) 1.50 at.% Ga, (c) 3.60 at.% Ga, (d) 5.03 at.% Ga, (e) 7.12 at.% Ga, (f) 9.08 at.% Ga.....	58

Figure 3.20 AFM images of (a) ZnO and Ga doped ZnO, (b) 1.50 at.% Ga, (c) 3.60 at.% Ga, (d) 5.03 at.% Ga, (e) 7.12 at.% Ga, (f) 9.08 at.% Ga.....	59
Figure 3.21 X-ray diffraction pattern of ZnO and Ga doped ZnO films.....	61
Figure 3.22 HRTEM, SAED images of (a, b, c) ZnO and (d, e, f) 5.03 at.% Ga doped ZnO.....	62
Figure 3.23 X-ray diffraction pattern of ZnO and IGZO films	65
Figure 3.24 FESEM images of (a) ZnO and IGZO with the ratio of In:Ga:Zn (b) 1:1:0.5 (c) 1:1:1.5 (d) 1:1:2.5 (e) 1:1:3.5	66
Figure 3.25 AFM images of (a) ZnO and IGZO with the ratio of In:Ga:Zn (b) 1:1:0.5 (c) 1:1:1.5 (d) 1:1:2.5 (e) 1:1:3.5 (f) the root mean square (RMS) surface roughness of ZnO and IGZO.....	67
Figure 3.26 Variation of resistivity of ZnO and IGZO films with different Zn concentration	68
Figure 3.27 (a) UPS spectra and (b) absorption spectra of ZnO and IGZO with different Zn concentration.....	69
Figure 3.28 XPS spectra of ZnO and IGZO films (a) Zn 2 <i>p</i> (b) O 1 <i>s</i> (c) In 3 <i>d</i> (d) Ga 2 <i>p</i>	70
Figure 3.29 (a) Device structure and (b) energy level diagrams of inverted polymer solar cells with IGZO as an electron extraction layer.	71
Figure 3.30 J-V characteristics of inverted polymer solar cell using ZnO and IGZO with different Zn concentration.....	73
Figure 3.31 (a) Dark J-V characteristics and (b) IPCE spectra of inverted polymer solar cells using ZnO and IGZO with different Zn concentration.....	74
Figure 3.32 Incident light intensity dependence of (a) J _{sc} (b) V _{oc} (c) FF and (d) PCE of inverted polymer solar cells using ZnO and IGZO with different Zn concentration.	75

Figure 3.33 Absorption spectra of PTB7-Th, PTB7-Th:PC ₇₀ BM, PTB7, PTB7:PC ₇₀ BM and PC ₇₀ BM	76
Figure 3.34 Device characteristics of inverted polymer solar cells with different electron extraction layers (a) J-V characteristics, (b) IPCE spectra based on PTB7:PC ₇₀ BM and (c) J-V characteristics, (d) IPCE spectra based on PTB7-Th:PC ₇₀ BM	78
Figure 3.35 Impedance spectra of the inverted polymer solar cell with different electron extraction layer	80
Figure 3.36 Incident light intensity dependence of (a) J _{SC} (b) V _{OC} (c) FF (d) PCE of inverted polymer solar cells with different electron extraction layers at room temperature.....	82
Figure 3.37 J _{SC} as a function of light intensity (1 ~ 100 mW/cm ²) for various temperatures (100 ~ 350 K) for inverted polymer solar cells (a) ZnO (b) In doped ZnO (c) Al doped ZnO (d) Ga doped ZnO (f) IGZO and (e) Recombination coefficient obtained in the temperature range of 100~ 350 K	84
Figure 3.38 Temperature dependence of (a) V _{OC} (b) J _{SC} (c) FF (d) PCE of inverted polymer solar cell with different electron extraction layer	85
Figure 3.39 Arrhenius plot of J _{SC} against T for the inverted polymer solar cells with different electron extraction layer (a) ZnO (b) In doped ZnO (c) Al doped ZnO (d) Ga doped ZnO (e) IGZO and (f) activation energy extracted from the data shown in (a) to (e).	87
Figure 3.40 J-V curves of the inverted polymer solar cells using ZnO under the various incident light intensity and temperature to evaluate collection voltages (V _C)	89

Figure 3.41 J-V curves of the inverted polymer solar cells using In doped ZnO under the various incident light intensity and temperature to evaluate collection voltages (V_C)	89
Figure 3.42 J-V curves of the inverted polymer solar cells using Al doped ZnO under the various incident light intensity and temperature to evaluate collection voltages (V_C)	90
Figure 3.43 J-V curves of the inverted polymer solar cells using Ga doped ZnO under the various incident light intensity and temperature to evaluate collection voltages (V_C)	90
Figure 3.44 J-V curves of the inverted polymer solar cells using IGZO under the various incident light intensity and temperature to evaluate collection voltages (V_C)	91
Figure 3.45 (a) Collection voltage (b) carrier collection length at short circuit condition (c) carrier collection efficiency at short circuit condition (d) effective $\mu\tau$ product of inverted polymer solar cells with different electron extraction layer	92
Figure 4.1 (a) J-V characteristics and (b) IPCE spectra of inverted polymer solar cell using Al doped TiO_2 with different Al doping concentration	97
Figure 4.2 X-ray diffraction pattern of TiO_2 and Al, In, Ga, Sn and Zn doped TiO_2	98
Figure 4.3 FESEM images of (a) TiO_2 (b) Al doped TiO_2 (c) In doped TiO_2 (d) Ga doped TiO_2 (e) Sn doped TiO_2 (f) Zn doped TiO_2	99
Figure 4.4 AFM images of (a) TiO_2 (b) Al doped TiO_2 (c) In doped TiO_2 (d) Ga doped TiO_2 (e) Sn doped TiO_2 (f) Zn doped TiO_2	100
Figure 4.5 HRTEM, SAED images of (a, b, c) TiO_2 , (d,e,f) Al doped TiO_2 , (g,h,i) In doped TiO_2 , (j,k,l) Ga doped TiO_2 , (m,n,o) Sn doped TiO_2 and (p,q,r) Zn doped TiO_2	102

Figure 4.6 The tip-sample current of (a) TiO ₂ and (b) Sn doped TiO ₂ surfaces measured by conductive AFM (C-AFM) at a sample bias of 550 mV	103
Figure 4.7 (a) J-V characteristics and (b) IPCE spectra of inverted polymer solar cell using pristine TiO ₂ and Al, In, Ga, Sn and Zn doped TiO ₂	104
Figure 4.8 J-V characteristics of inverted polymer solar cell using TiO ₂ and Al, In, Ga, Sn and Zn doped TiO ₂ at 2 at.% doping concentration.....	106
Figure 4.9 J _{SC} as a function of light intensity (1-100 mW/cm ²) for various temperatures (100-350 K) for inverted polymer solar cells (a) TiO ₂ (b) Al doped TiO ₂ (c) In doped TiO ₂ (d) Ga doped TiO ₂ (e) Sn doped TiO ₂ (f) Zn doped TiO ₂ and (g) Recombination coefficient obtained in the temperature range of 100-350 K.....	108
Figure 4.10 Arrhenius plot of J _{SC} against T for the inverted polymer solar cells with different extraction layer (a) TiO ₂ (b) Al doped TiO ₂ (c) In doped TiO ₂ (d) Ga doped TiO ₂ (e) Sn doped TiO ₂ (f) Zn doped TiO ₂ and (g) activation energy extracted from the data shown in (a) to (f).	110
Figure 4.11 (a) Device structure and (b) energy level diagrams of inverted polymer solar cells with TiO ₂ and Zn doped TiO ₂ as an electron extraction layer	111
Figure 4.12 UPS spectra of (a) TiO ₂ , 0.05 wt.% PEO:TiO ₂ and (b) ZTO, 0.05 wt.% PEO:ZTO films	112
Figure 4.13 Absorption spectra of (a) TiO ₂ , 0.05 wt.% PEO:TiO ₂ and (b) ZTO, 0.05 wt.% PEO:ZTO films	112
Figure 4.14 XPS spectra of TiO ₂ and ZTO films (a) Ti2p, (b) O1s and (c) Zn2p ..	114
Figure 4.15 Absorption spectra of PTB7:PC ₇₀ BM, TiO ₂ /PTB7:PC ₇₀ BM and ZTO/PTB7:PC ₇₀ BM films (b) TiO ₂ and ZTO films	115

Figure 4.16 TFT device structure and transfer characteristics of TiO ₂ and ZTO TFTs	115
Figure 4.17 J-V characteristics of inverted polymer solar cells based on PTB7:PC ₇₀ BM using TiO ₂ and PEO modified TiO ₂	117
Figure 4.18 (a) dark J-V characteristics and (b) IPCE spectra of inverted polymer solar cells based on PTB7:PC ₇₀ BM using TiO ₂ and PEO modified TiO ₂	118
Figure 4.19 J-V characteristics of inverted polymer solar cells based on PTB7:PC ₇₀ BM using ZTO and PEO modified ZTO	119
Figure 4.20 (a) dark J-V characteristics and (b) IPCE spectra of inverted polymer solar cells based on PTB7:PC ₇₀ BM using ZTO and PEO modified ZTO	120
Figure 4.21 The stability of the PTB7:PC ₇₀ BM based inverted polymer solar cells using TiO ₂ , 0.05 wt.% PEO:TiO ₂ , ZTO and 0.05 wt.% PEO:ZTO as an electron extraction layer	120
Figure 4.22 PL spectra of (a) TiO ₂ , PEO:TiO ₂ and (b) ZTO, PEO:ZTO	122
Figure 4.23 AFM images of (a) TiO ₂ (b) 0.01 wt.% PEO:TiO ₂ (c) 0.05 wt.% PEO:TiO ₂ (d) 0.1 wt.% PEO:TiO ₂ (e) 0.3 wt.% PEO:TiO ₂	124
Figure 4.24 AFM images of (a) ZTO (b) 0.01 wt.% PEO:ZTO (c) 0.05 wt.% PEO:ZTO (d) 0.1 wt.% PEO:ZTO (e) 0.3 wt.% PEO:ZTO	125

List of Tables

Table 1.1 Selected performance parameters of inverted polymer solar cells depend on electron extraction layers	7
Table 1.2 Selected performance parameters of inverted polymer solar cells with metal doped oxide interfacial layer.....	10
Table 3.1 Summary of the performance parameters of inverted polymer solar cells with ZnO and In doped ZnO as an electron extraction layer.....	41
Table 3.2 Device performance of the inverted polymer solar cell with ZnO and Al doped ZnO with different Al doping concentration under AM1.5G illumination with 100 mW/cm ² light intensity.	49
Table 3.3 Device performance of inverted structure with different active layers using ZnO and Ga doped ZnO with different Ga doping concentration.	57
Table 3.4 Device performance of inverted polymer solar cells using ZnO and IGZO with different Zn concentration.	73
Table 3.5 Summary of the performance parameters of PTB7:PC ₇₀ BM based inverted polymer solar cells with different electron extraction layers.	79
Table 3.6 Summary of the performance parameters of PTB7-Th:PC ₇₀ BM based inverted polymer solar cells with different electron extraction layers ..	79

Table 4.1 Device performance of the inverted polymer solar cells using pristine TiO ₂ and Al doped TiO ₂ with different Al doping concentration under AM1.5G illumination with 100 mW/cm ² light intensity.....	97
Table 4.2 Device performance of the inverted polymer solar cells with TiO ₂ and Al, In, Ga, Sn and Zn doped TiO ₂ at 1 at.% doping concentration under AM1.5G illumination with 100 mW/cm ² light intensity.....	104
Table 4.3 Device performance of the inverted polymer solar cells with TiO ₂ and Al, In, Ga, Sn and Zn-doped TiO ₂ at 2 at.% under AM1.5G illumination with 100 mW/cm ² light intensity.....	106
Table 4.4 Valance band, conduction band and band gap of TiO ₂ , 0.05 wt.% PEO:TiO ₂ , ZTO and 0.05 wt.% PEO:ZTO films.	113
Table 4.5 Performance parameters of the devices based on PTB7:PC ₇₀ BM using PEO:TiO ₂ and PEO:ZTO as an electron extraction layers.....	121

Chapter 1

Introduction

It is well known that the Earth's surface temperature has risen continuously since the 19th century. It is certain that the concentrations of greenhouse gases such as carbon dioxide (CO_2) have risen in Earth's due to the combustion of fossil fuels [1]. However Today's plants are unable to absorb this huge amount of CO_2 . As a result the CO_2 concentration in the atmosphere will continually increase, which influenced harmful effects of Earth's environment such as global warming. The risk of global warming has spurred interest in renewable energy sources such as geothermal, winds, hydropower, bio, ocean, solar, and so on. Among the renewable energy sources, the sun is probably the most important source of renewable energy available today, so solar energy came into the spotlight. Traditionally, the sun has provided energy for practically all living creatures on earth, through the process of photosynthesis, in which plants absorb solar radiation and convert it into stored energy for growth and development. The U.S Energy Information Administration forecasted that solar

grows rapidly, increasing nearly 7-fold by 2035 (Figure 1.1), as near-term market growth is projected to result in lower system costs. The majority of the growth in solar is with photovoltaic, a significant portion of which comes from the end-use sector (i.e., rooftop solar)

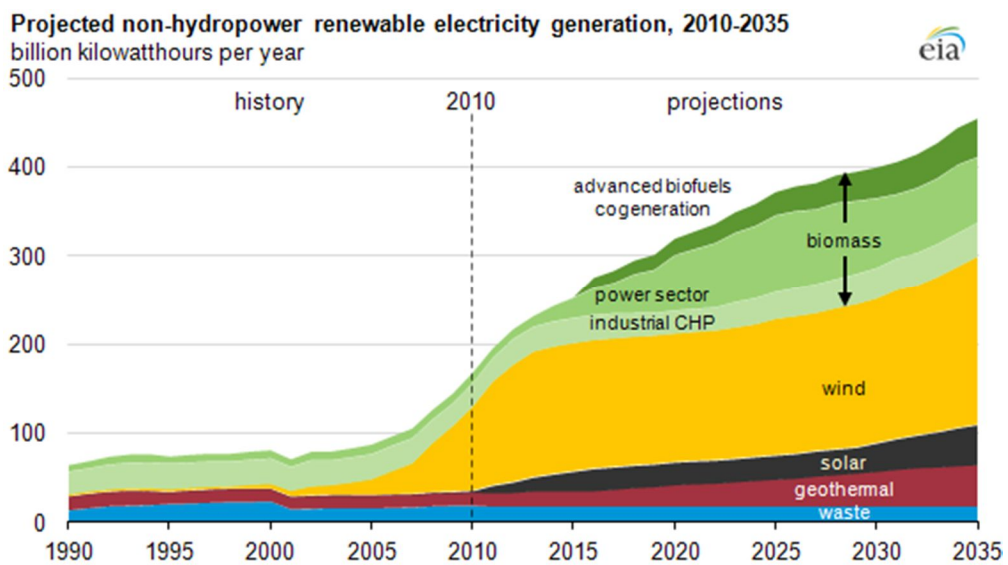


Figure 1.1 Projected non-hydropower renewable electricity generation, 2010 - 2035
(Source : U. S. Energy Information Administration (Feb 2012))

1.1 Overview of Organic Solar Cells

The solar cell is called a photovoltaic cell, which converts light energy directly into electrical energy. The solar cells can be classified into inorganic and organic solar cell. Silicon (Si) based solar cell is typical inorganic solar cell, which are widely used in the world because of high efficiency. However the raw materials of silicon are very expensive and they can't apply to widespread application such as flexible electronics, clothes and windows of building and so on. On the other hand, organic solar cells have attracted considerable attention as a promising alternative because of their potential for large area fabrication process, lightweight, flexibility, and inexpensiveness [2-4].

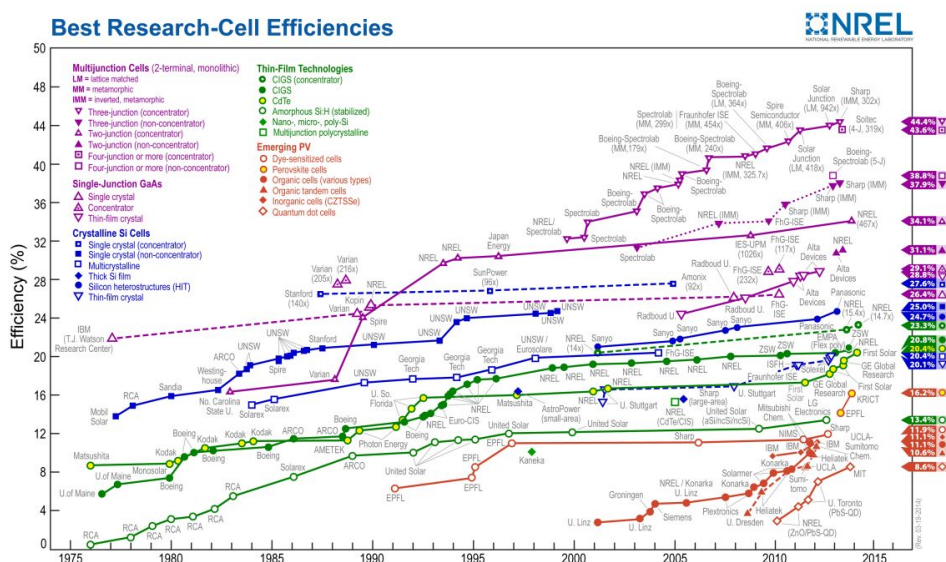


Figure 1.2 Best research solar cell efficiencies record (Source : The National Center for Photovoltaics (NCPV) at NREL)

However, organic solar cells have some disadvantages such as low chemical stability and low power conversion efficiency (PCE). But the power conversion efficiency of organic solar cell is continually improved since 2001 year as shown in Figure 1.2. Within a few years, the power conversion efficiency was increased from 2 % to 9 % and recently, power conversion efficiency has been reached over 10 % using polymer:fullerene bulk heterojunction and tandem device from UCLA [5-6].

Conjugated polymer:fullerene bulk heterojunction based single structure is made to conventional and inverted type. In most conventional structure, poly (3,4-ethylenedioxythiophene) : poly(styrenesulfonate) (PEDOT:PSS) hole transport layer and low-work-function metal electrode (Ca or Ba) are generally used. However, the strong acidic nature of PEDOT:PSS leads to degradation of the ITO electrode, which impose large problem with respect to device stability and reproducibility of solar cells. In particular, the low-work-function metal is susceptible to degradation by oxygen and water vapor [7-9]. In addition, optical loss due to absorption of the PEDOT:PSS film is significant, approaching 10% in the visible range and even higher in the near infrared region [10]. Some reports have shown that PEDOT:PSS is also an inefficient electron-blocking layer, reducing the efficiency of electronic devices through electron leakage to the anode electrode [11]. For these reasons, alternative high work function layer have been explored and demonstrated by replacing PEDOT:PSS with transition metal-oxides such as molybdenum oxide (MoO_3) [8,12], vanadium oxide (V_2O_5) [12,18] and nickel oxide (NiO) [13]. In order to overcome these problems, inverted polymer solar cells have been studied. In the inverted structure, air stable and high work function metals (e.g., Au, Ag) are used as the anode to collect holes and ITO is used as the cathode to collect electrons. Moreover, high-work function metal such as Ag, which can be formed using coating or printing technology to simplify and lower the cost of manufacturing. [14].

1.2 Electron Extraction Layer of Inverted Polymer Solar Cells

One key challenge in making efficient inverted polymer solar cells is the electron extraction layer. This layer should satisfy several criteria, such as high transparency, high electron affinity energy, and efficiently collect the electrons. Recently, a number of works have been reported about electron extraction layer in the inverted polymer solar cell as shown in Table 1.1.

In 2005, J. -M. Nunzi et al., used Au as an anode electrode instead of Al due to energy level matching and air stability, while they use BCP or perylene as an electron extraction layer. Although the device efficiency was low, it exhibits improved stability in air with respect to aluminum on top devices [15]. In order to increased power conversion efficiency, Y. Yang et al., first demonstrate an enhancement in inverted polymer solar cell efficiency by using cesium carbonate (Cs_2CO_3) as an electron extraction layer [16-18]. Afterwards, the metal oxide was used as an electron extraction layer. In 2006, J. Y. Kim and A. J. Heeger used thin TiO_x layer as an electron extraction layer. Although this TiO_x was used as an optical spacer in conversional structure, the TiO_x has outstanding electron extraction property [19]. As a result, even now TiO_x was widely used as an electron extraction layer in the inverted structure from C. J. brabec [20] and many research groups. Sometime TiO_x extended exposure in air or N_2 improved the open-circuit voltage (V_{oc}) and FF of the devices. The improvement in device characteristics over short time scales is attributed to the filling of shallow electron traps in titania [21]. Moreover, nanocrystalline titanium dioxide (nc- TiO_2) was used as well [22]. At the same time, in 2007, A. J. Janssen et al., used ZnO layer in conventional structure. Thin ZnO layer acts as an optical spacer and efficient electron extraction layer [23].

Since then nanoparticle and sol-gel type of ZnO was widely used as an electron extraction layer in the inverted polymer:fullerene bulk heterojunction structure to enhanced electron extraction property [24-26]. To top it off, some groups have study morphology control, grid structure, plasmonic of electron extraction layer and the use of conjugated polymer instead of metal oxide. In 2008, B. -Y. Yu et al., used vertical TiO₂ nanotube array in inverted polymer solar cell. As a result, both the polymer-TiO₂ and polymer-fullerene provide interfaces for charge separation, and the TiO₂ nanotubes arrays permit vertical charge transport from the absorption layer to the electrode [27]. S. K. Hau and H. -L. Yip investigated the morphological modification of electron extraction layer by self-assemble monolayer (SAM) treatment of TiO_x [28] and ZnO [29]. Y. Cao et al., used alcohol and water soluble conjugated polymer which is called PFN (poly [(9,9-bis(3'-(N,N-dimethylamino)propyl)-2,7-fluorene)-alt-2,7-(9,9-dioctylfluorene)]) as an electron extraction layer instead of metal oxide. This layer simultaneously offers ohmic contact for photogenerated charge-carrier collection and allows optimum photon harvest in the device [30]. Moreover, double layers such as metal oxide/conjugated polymer [31], organic layer/metal oxide [32] and metal oxide/metal oxide [33] were used as an electron extraction layer. This two layer help good contact and good interface adhesion between electron extraction layer and active layer, which attributed to enhanced charge transport via suppressed bimolecular recombination [31]. Beside, both favorable alignment of the nanowire π - π stacking axes parallel to the photocurrent flow and to the increased interfacial layer-active layer contact area [32]. Recently, plasmonic research was studied by insertion of Ag and Au nanoparticles in electron extraction layer, which attributed to improve absorption and current density by redistribution of incident photons [34-36].

Table 1.1 Selected performance parameters of inverted polymer solar cells depend on electron extraction layers

Electron extraction layer	Active layer	J_{sc} (mA/cm ²)	V_{oc} (V)	FF (%)	PCE (%)	Ref
BCP or perylene	MEH-PPV:PCBM	1.20	0.36	29	0.17	[15]
Cs ₂ CO ₃	P3HT:PCBM	8.42	0.56	47.78	2.25	[16]
	P3HT:PCBM	11.29	0.58	62.0	4.08	[17]
	P3HT:PCBM	8.64	0.56	55.69	2.70	[18]
TiO _x	P3HT:PCBM	9.0	0.60	57.4	3.10	[20]
	P3HT:PCBM	8.5	0.57	49.5	2.40	[21]
nc-TiO ₂	P3HT:PCBM	6.57	0.63	62.3	2.57	[22]
ZnO	P3HT:PCBM	11.17	0.62	54.3	3.78	[24]
	P3HT:PCBM	9.15	0.59	60	3.2	[25]
	PF10TBT:PCBM	6.61	0.95	59	3.7	[25]
	PCPDTBT:PCBM	9.14	0.58	50	2.6	[25]
	PCDTBT:PCBM	10.41	0.88	68.8	6.08	[26]
TiO ₂ nanotube	P3HT:PCBM	10.96	0.59	42	2.71	[27]
SAM treated TiO ₂	P3HT:PCBM	10.6	0.62	57.2	3.8	[28]
PFN	PTB7:PCBM	17.2	0.74	72	9.15	[30]
ZnO/PFN	PBDT-DTNT:PCBM	17.4	0.75	61	8.4	[21]
F ₁₆ CuPc NW/ZnO	P3HT:PCBM	10.74	0.57	58.5	3.59	[32]
F ₁₆ CuPc NW/ZnO	PTB7:PCBM	15.83	0.74	73.85	8.57	[32]
ZnO ripple/ALD-ZnO	PTB7-F20:PCBM	16.12	0.67	67.7	7.38	[33]
Cs ₂ CO ₃ + Au NPs	P3HT:PCBM	10.11	0.55	64	3.54	[34]
ZnO+ Au NPs	P3HT:PCBM	7.88	0.54	57	2.35	[35]

TiO ₂ + Au NPs	P3HT:PCBM	10.15	0.64	64.8	4.20	[36]
TiO ₂ + Au NPs	PTB7:PCBM	18.07	0.71	68.1	8.74	[36]

Among the many n-type electron extraction layer used in inverted devices, ZnO and TiO₂ is a promising candidate because of its relatively high electron mobility, high transparency and environmental stability. A variety of fabrication methods have been employed to grow thin films of ZnO and TiO₂ such as sol-gel spin coating or nanoparticle spin coating. Especially, sol-gel method has been extensively investigated as a solution based thin film deposition process [37].

1.3 Metal Doped Oxide as an Electron Extraction Layer

It is well known that the physical characteristics of metal oxide thin films depend on the doping and a systematic study of the doping effect is always interesting. The doping of semiconductors with various elements is known to greatly affect many of the basic physical properties of the semiconductor, including its electrical, optical, morphological and structural properties, which are all crucial for most of the practical applications [38-41]. Especially, metal doped oxide can intensively improve the electrical properties such as electron mobility and conductivity [42-43]. In this reason, some research groups used metal doped oxide as an anode electrode instead of ITO electrode in the organic solar cell devices [44-46] and OLED devices [47]. However, except the use of electrode, there are still not many researches about the use of metal doped oxide as an electron extraction layer in the organic solar cells and other organic devices. Table 1.2 shows the selected performance parameters of inverted polymer solar cells with metal doped oxide interfacial layer. Even if, C. J. Brabec et al., studied the use of metal doped oxide as an electron extraction layer, the power conversion efficiency is still low [48-52]. The best power conversion efficiency of polymer solar cell used metal doped oxide interfacial layer is 3.3 % [50]. Moreover, the lack of systematic research on the reason of enhanced device performance. Therefore, systematic study of metal doped oxide as an interfacial layer and correlated device physics in the polymer solar cell systems should be investigated.

Table 1.2 Selected performance parameters of inverted polymer solar cells with metal doped oxide interfacial layer.

Electron extraction layer	Active layer	J_{sc} (mA/cm ²)	V_{oc} (V)	FF (%)	PCE (%)	Ref
In doped ZnO	P3HT:PCBM	7.3	0.53	54	2.3	[11]
	P3HT:PCBM	8.41	0.56	53.9	2.56	[12]
	P3HT:PCBM	9.93	0.60	55	3.3	[13]
Al doped ZnO	P3HT:PCBM	8.36	0.57	50.8	2.42	[12]
	P3HT:PCBM	9.23	0.60	51.9	2.88	[14]
Ga doped ZnO	P3HT:PCBM	11.7	0.42	39.7	1.95	[15]

1.4 Outline of Thesis

This thesis consists of five chapters including **Introduction** and **Conclusion**. In **Chapter 1**, brief overview of organic solar cells and its research issues are introduced. The motivation of this thesis was also introduced in this chapter. In **Chapter 2**, basic organic solar cell theories, sample fabrication procedure of polymer solar cell, the experimental setup, the device characterization and analysis methods are described. Moreover, the organic materials which used in this thesis are also described. In **Chapter 3**, the effect of In, Al and Ga doping on the structural, morphological, optical and electrical properties of the ZnO thin films as well as IGZO have been systematically investigated. Besides, inverted polymer solar cell containing In, Al, Ga doped ZnO and IGZO as an electron extraction layer with the device structure of ITO/ In, Al, Ga doped ZnO and IGZO / PCDTBT:PC₇₀BM or PTB7:PC₇₀BM or PTB7-Th:PC₇₀BM / MoO₃ / Al has been fabricated and its characteristics have been studied. In **Chapter 4**, the effect of In, Al, Ga, Sn and Zn doped TiO₂ thin film properties and have fabricated inverted polymer solar cells with the structure of ITO / doped TiO₂ / PTB7:PC₇₀BM / MoO₃ / Al. Moreover polyethylene oxide (PEO) modified TiO₂ and Zn doped TiO₂ was applied as an electron extraction layer. Finally, In **Chapter 5** contains the summary and suggestion of further study and vision for this thesis.

Chapter 2

Theory and Experimental Methods

2.1 Principles of Organic Solar Cells

2.1.1 Operation Principle

The operation principle of organic solar cells is different as compared to inorganic solar cells. In case of inorganic solar cells consisted of P-N junction, the photons are directly converted into free charge carriers and then can be collected at their each of electrodes. On the other hand, this is not the case in organic solar cells. Figure 2.1 shows the working principle of organic solar cells. When light irradiates the active layer (doner/accepter) of the organic solar cells, the active layer will absorb photons (Figure 2.1 (a)) to produce electron and hole pairs, called exciton, and the excitons will diffuse toward (Figure 2.1 (b)) and dissociate at the doner and acceptor into electrons in the lowest unoccupied molecular orbital (LUMO) of the acceptor and holes in the highest occupied molecular orbital (HOMO) of the doner (Figure 2.1 (c,d)). Then, holes and electrons will transfer and collect to the each of electrodes (Figure 2.1 (e, f)).

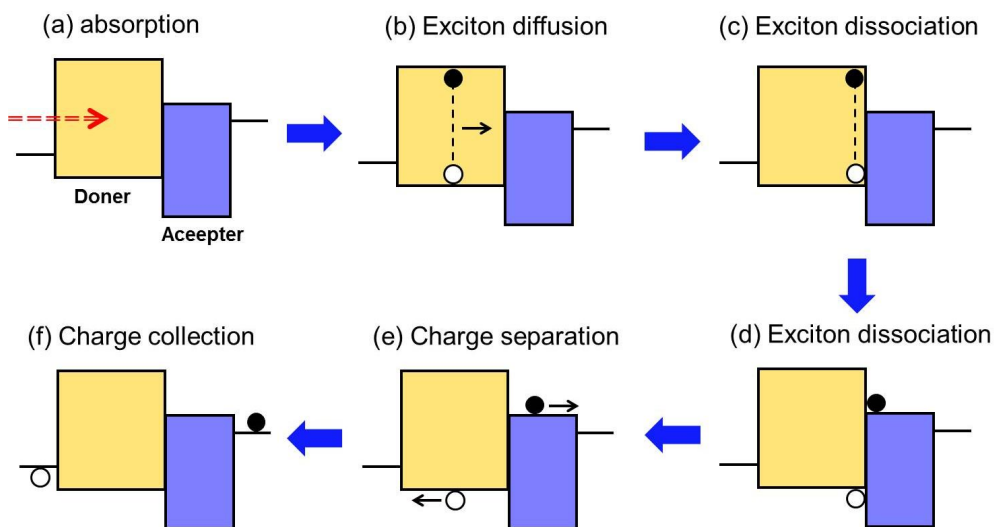


Figure 2.1 Working principles of organic solar cells.

2.1.2 Basic solar cell Performance Parameters

The organic solar cell performance can be characterized by current density-voltage (J-V) curve under illumination of a light source. This curve provides basic properties of solar cell, which is shown in Figure 2.2

The short circuit current density (J_{SC}) is measured by dividing short circuit current (I_{SC}) by the area of organic solar cell. The J_{SC} flows through the external circuit when there is no external field applied. This is related to optical and electrical properties of organic solar cell such as band gap, mobility, exciton dissociation, charge carrier transport, recombination and collection. Therefore, in order to improve J_{SC} factor, optical and electrical matching are important.

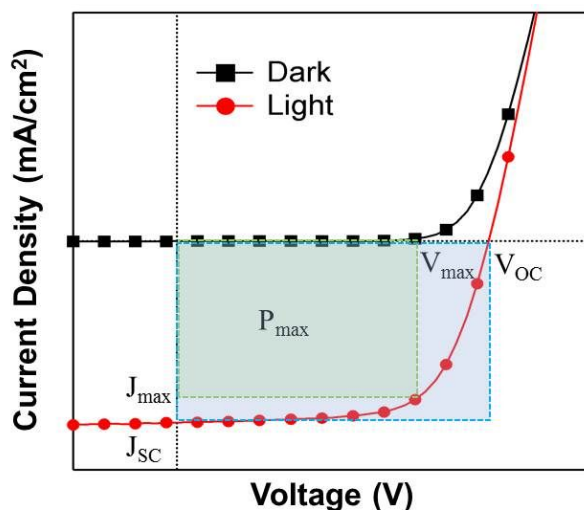


Figure 2.2 Current density-voltage (J-V) curve of organic solar cell.

The open circuit voltage (V_{OC}) is the maximum voltage delivered by organic solar cell at which no current flows through the external circuit. For organic solar cell device, V_{OC} can be estimated by the gap between the HOMO level of doner material and the LUMO level of acceptor material, which the reason to be the limiting factor. By controlling HOMO and LUMO level of doner and acceptor materials, we can improve the V_{OC} of organic solar cell.

The maximum power point (MPP, $P_{max} = J_{max} \cdot V_{max}$) is described as the area where the product of the current and the voltage reaches a maximum as shown in Figure 2.2

The fill factor (FF) is the ratio between the maximum power generated by a solar cell device and the product of open circuit voltage (V_{OC}) and short circuit current density (J_{SC}). The FF is described by the following equation:

$$FF = \frac{J_{\max} \times V_{\max}}{J_{SC} \times V_{OC}} = \frac{P_{\max}}{J_{SC} \times V_{OC}} \quad (2.1)$$

The power conversion efficiency (PCE) is the most important parameter to compare the performance of organic solar cell. The PCE is defined as follows:

$$PCE = \frac{P_{\max}}{P_{input}} = \frac{J_{\max} \times V_{\max}}{P_{input}} = \frac{J_{SC} \times V_{OC} \times FF}{P_{input}} \times 100 \quad (2.2)$$

PCE are measured under standard test conditions, which are a room temperature (25 °C) and under AM 1.5G 100mW/cm² illumination.

The external quantum efficiency (EQE) is important parameter for characterization of organic solar cells. It is calculated by the number of electrons in external circuit divided by the number of incident photons at a certain wavelength under short circuit condition

$$EQE(\%) = \frac{n_{electron}}{n_{photons}} = \frac{J_{SC}(\lambda)/e}{P_{in}(\lambda)/(hc/\lambda)} = \frac{J_{SC}(\lambda)hc}{P_{in}(\lambda)e\lambda} \quad (2.3)$$

Where λ is the wavelength, e is the elementary charge, h is the Planck constant and c is the speed of light in vacuum. The measured EQE included the reflection at the surface and transmission through the device. If we considered the fraction of the absorbed photons by the active layer, internal quantum efficiency (IQE) was developed instead of EQE. IQE is very helpful in organic solar cell to study the physical processes arising in the organic semiconductor materials.

$$IQE(\%) = \frac{EQE}{1 - \text{Reflection} - \text{Transmission}} \quad (2.4)$$

2.2 Materials and Solution

2.2.1 Organic Materials

Figure 2.3 shows the used materials of photoactive polymer and hole transport materials in this thesis.

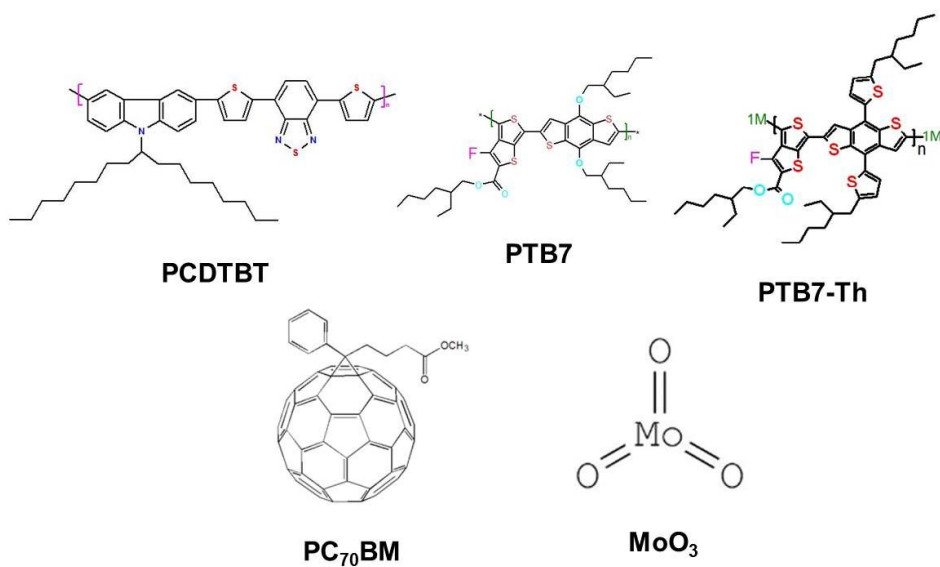


Figure 2.3 Chemical structure of used materials.

PCDTBT (Poly[[9-(1-octylnonyl)-9H-carbazole-2,7-diyl]-2,5-thiophenediyl-2,1,3-benzothiadiazole-4,7-diyl-2,5-thiophenediyl]) is widely used as an polymer (p-type) material for organic solar cell. The HOMO and LUMO levels are 5.5 eV and 3.6 eV respectively from the literature [53]. PCDTBT was purchased from 1-Material Inc and used in the inverted polymer solar cell as a photoactive doner material in the chapter 3.

PTB7 (Poly[[4,8-bis[(2-ethylhexyl)oxy]benzo[1,2-b:4,5-b']dithiophene-2,6-diyl][3-fluoro-2-[(2-ethylhexyl)carbonyl]thieno[3,4-b]thiophenediyl]]) is recently used as an polymer (p-type) material for organic solar cell. The HOMO and LUMO levels are 5.15 eV and 3.31eV respectively [54]. PTB7 was purchased from 1-Material Inc and used in the inverted polymer solar cell as a photoactive doner material in the chapter 3 and 4.

PTB7-Th is slight modified by PTB7. The HOMO and LUMO levels are 5.22 eV and 3.64eV respectively [55]. PTB7-Th was purchased from 1-Material Inc and used in the inverted polymer solar cell as a photoactive doner material in the chapter 3.

PC₇₀BM ([6,6]-phenyl C₇₀-butyric acid methyl ester (PC₇₀BM)) is one of the most widely used n-type material, which acts as an electron acceptor. The HOMO and LUMO levels are 6.1 eV and 4.3 eV respectively from the literature [54]. PC₇₀BM was purchased from 1-Material Inc and used in the chapter 3 and 4.

MoO₃ (molybdenum oxide) is commonly used as a hole transport layer in the organic solar cell and has 5.3 eV and 2.3 eV of HOMO and LUMO level [56]. By thermal evaporation under high vacuum conditions ($\sim 10^{-6}$ Torr), it can be easily deposited on the active layer. In this reason, we used MoO₃ as a hole transport layer in the inverted polymer solar cell in this chapter 3 and 4.

2.2.2 Making of Metal Oxide Precursor Solution

In chapter 3 and 4, ZnO, metal doped ZnO (In doped ZnO, Al doped ZnO, Ga doped ZnO and IGZO), TiO₂ and metal doped TiO₂ (In doped TiO₂, Al doped TiO₂, Ga doped TiO₂, Sn doped TiO₂ and Zn doped TiO₂) are used as an electron extraction layer in the inverted polymer solar cell. These layers have been prepared using a sol-gel spin coating method.

ZnO precursor solution was prepared by dissolving zinc acetate dehydrate ($\text{Zn}(\text{CH}_3\text{COO})_2 \cdot 2\text{H}_2\text{O}$, 0.25 M (0.55 g)) in ethanol (10 mL) and equal-molar ethanolamine ($\text{H}_2\text{NCH}_2\text{CH}_2\text{OH}$, 0.15 mL). The mixed solution was then stirred at room temperature for 2 hour to obtain a transparent mixture.

In doped ZnO precursor solution has been prepared using sol-gel spin coating method. Zinc acetate dihydrate ($\text{Zn}(\text{CH}_3\text{COO})_2 \cdot 2\text{H}_2\text{O}$, 0.25 M (0.55 g)) and indium (III) nitrate hydrate ($\text{In}(\text{NO}_3)_3 \cdot x\text{H}_2\text{O}$) (0.01 M (0.03 g), 0.03 M (0.09 g), 0.05 M (0.15 g), 0.07 M (0.21 g) and 0.09 M (0.27 g)) were dissolved in a mixture of ethanol (10 ml) and ethanolamine ($\text{H}_2\text{NCH}_2\text{CH}_2\text{OH}$, 0.15 mL) at room temperature. The resultant solution was stirred for 2 hour to yield a homogeneous, clear and transparent solution using magnetic stirrer.

Al doped ZnO precursor solution has been prepared using sol-gel spin coating method. Zinc acetate dihydrate ($\text{Zn}(\text{CH}_3\text{COO})_2 \cdot 2\text{H}_2\text{O}$, 0.25 M (0.55 g)) and aluminium (III) nitrate nonahydrate ($\text{Al}(\text{NO}_3)_3 \cdot 9\text{H}_2\text{O}$) (0.01 M (0.04 g), 0.03 M (0.11 g), 0.05 M (0.19 g), 0.07 M (0.26 g) and 0.09 M (0.34 g)) were dissolved in a mixture of ethanol (10 ml) and ethanolamine ($\text{H}_2\text{NCH}_2\text{CH}_2\text{OH}$, 0.15 mL) at room temperature. The resultant solution was stirred for 2 hour to yield a homogeneous, clear and transparent solution using magnetic stirrer.

Ga doped ZnO precursor solution also has been prepared using sol-gel spin coating method. Zinc acetate dihydrate ($\text{Zn}(\text{CH}_3\text{COO})_2 \cdot 2\text{H}_2\text{O}$, 0.25 M (0.55 g)) and gallium (III) nitrate hydrate ($\text{Ga}(\text{NO}_3)_3 \cdot x\text{H}_2\text{O}$) (0.01 M (0.03 g), 0.03 M (0.08 g), 0.05 M (0.13 g), 0.07 M (0.18 g) and 0.09 M (0.23 g)) were dissolved in a mixture of ethanol (10 ml) and ethanolamine ($\text{H}_2\text{NCH}_2\text{CH}_2\text{OH}$, 0.15 mL) at room temperature. The resultant solution was stirred using a magnetic stirrer for 2 hour to yield a homogeneous, clear and transparent solution.

IGZO precursor solution also has been prepared using sol-gel spin coating method. Indium (III) nitrate hydrate ($\text{In}(\text{NO}_3)_3 \cdot x\text{H}_2\text{O}$) (0.1 M (0.3 g)), gallium (III) nitrate hydrate ($\text{Ga}(\text{NO}_3)_3 \cdot x\text{H}_2\text{O}$) (0.1 M (0.25 g)), and zinc acetate dihydrate ($\text{Zn}(\text{CH}_3\text{COO})_2 \cdot 2\text{H}_2\text{O}$) (0.05 M (0.11 g), 0.15 M (0.33 g), 0.25 M (0.55 g) and 0.35 M (0.77 g)) were dissolved in a mixture of ethanol (10 mL) and ethanolamine ($\text{NH}_2\text{CH}_2\text{CH}_2\text{OH}$, 0.15 mL) at room temperature. The molar ratio of indium:gallium:zinc (In:Ga:Zn) in the precursor solution was varied as 1:1:0.5 to 1:1:3.5. The resultant solution was stirred for 2 hour to yield a homogeneous, clear and transparent solution using magnetic stirrer.

TiO₂ precursor solution has been prepared using sol-gel spin coating method. Titanium (IV) butoxide ($\text{Ti}(\text{OCH}_2\text{CH}_2\text{CH}_2\text{CH}_3)_4$, 0.45 M (1.534 mL)) was dissolved in a mixture of 2-methoxyethanol ($\text{CH}_3\text{OCH}_2\text{CH}_2\text{OH}$, 10 mL) and acetylacetone ($\text{CH}_3\text{COCH}_2\text{COCH}_3$, 0.45 M, 0.461 mL) at room temperature. The resultant solution was stirred for 2 hour to yield a homogeneous, clear and transparent (light yellowish color) solution using magnetic stirrer.

Al, In, Ga, Sn, Zn doped TiO₂ precursor solution have been prepared by dissolving each materials in TiO₂ precursor solution. The aluminium (III) nitrate nonahydrate ($\text{Al}(\text{NO}_3)_3 \cdot 9\text{H}_2\text{O}$, 0.01 M (0.04 g)), indium (III) nitrate hydrate ($\text{In}(\text{NO}_3)_3 \cdot x\text{H}_2\text{O}$, 0.01 M (0.03 g)), gallium (III) nitrate hydrate ($\text{Ga}(\text{NO}_3)_3 \cdot x\text{H}_2\text{O}$, 0.01 M (0.03 g)), tin (II) chloride dihydrate ($\text{SnCl}_2 \cdot 2\text{H}_2\text{O}$, 0.01 M (0.02 g)) and Zinc acetate dihydrate ($\text{Zn}(\text{CH}_3\text{COO})_2 \cdot 2\text{H}_2\text{O}$, 0.01 M (0.02 g)) were added.

PEO modified TiO₂ and Zn doped TiO₂ have been prepared by slowly adding Polyethylene oxide (PEO) solution in TiO₂ and Zn doped TiO₂ precursor solution. PEO solution were made by dissolving PEO power (0.01 wt.% (0.001 g), 0.05 wt.% (0.005 g), 0.1 wt.% (0.01 g) and 0.3 wt.% (0.03 g)) in chlorobenzene.

2.2.3 Making of Organic Solution

PCDTBT:PC₇₀BM blend solution was prepared by mixing PCDTBT (5 mg) and PC₇₀BM (20 mg) in 1,2-dichlorobenzene (1 mL). This solution is stirred at room temperature for overnight and used as an active layer of inverted polymer solar cell in the chapter 3.

PTB7:PC₇₀BM blend solution was prepared with a weight ratio of 1:1.5 (10 mg of PTB7 : 15 mg of PC₇₀BM) in mixed solvent of chlorobenzene/1,8-diiodooctane (97:3 vol.%). This solution is stirred at room temperature for overnight and used as an active layer of inverted polymer solar cell in the chapter 3 and 4.

PTB7-Th:PC₇₀BM blend solution was prepared with a weight ratio of 1:1.5 (10 mg of PTB7-Th : 15 mg of PC₇₀BM) in mixed solvent of chlorobenzene/1,8-diiodooctane (97:3 vol.%). This solution is stirred at room temperature for overnight and used as an active layer of inverted polymer solar cell in the chapter 3.

2.3 Device and Thin Film Fabrication

2.3.1 Device Fabrication of Polymer Solar Cells

Inverted polymer solar cells (used in chapter 3 and 4) were constructed with a device structure of the ITO / electron extraction layer / polymer:PC₇₀BM / MoO₃ / Al as shown in Figure 2.4. The patterned indium tin oxide (ITO) substrates ($\sim 15 \Omega/\square$) were cleaned using isopropyl alcohol, acetone and deionized water (in that order) in an ultrasonic bath, for 20 min each. The cleaned substrates then were dried at 120 °C for more than 2 hour. A thin layer of ZnO (Chapter 3), In doped ZnO (Chapter 3), Al doped ZnO (Chapter 3), Ga doped ZnO (Chapter 3), IGZO (Chapter 3), TiO₂ (Chapter 4), In, Al, Ga, Sn, Zn doped TiO₂ (Chapter 4), PEO modified TiO₂ (Chapter 4) and Zn doped TiO₂ (Chapter 4) were prepared by spin-coating on ITO substrate at 3500 rpm for 40 sec. The electron extraction layers of thickness 25 ~ 30 nm were formed after post annealing at 450 °C for 2 hour. Then, the PCDTBT:PC₇₀BM (Chapter 3), PTB7:PC₇₀BM (Chapter 3 and 4) and PTB7-Th-PC₇₀BM (Chapter 3) blend solution were spin coated in the glove box at 600 rpm 60 sec, 1000 rpm for 60 sec and 1000 rpm for 60 sec respectively. The thickness of all active layers are 70 ~ 80 nm. After that the organic layer was slowly dried in a vacuum for overnight, a layer of MoO₃ (10 nm) as a hole transport layer and Al (100 nm) as an electrode were thermally evaporated on top of the active layer through a shadow mask under a pressure of $\sim 10^{-6}$ Torr.

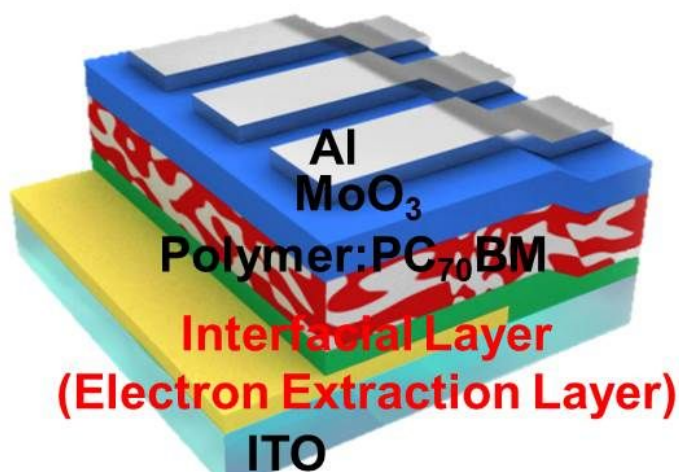


Figure 2.4 Device structure of inverted polymer solar cells

2.3.2 Thin Film Fabrication

In order to analysis thin film properties of electron extraction layer and active layer such as ZnO (Chapter 3), In doped ZnO (Chapter 3), Al doped ZnO (Chapter 3), Ga doped ZnO (Chapter 3), IGZO (Chapter 3), TiO₂ (Chapter 4), In, Al, Ga, Sn, Zn doped TiO₂ (Chapter 4), PEO modified TiO₂ (Chapter 4) and Zn doped TiO₂ (Chapter 4), PCDTBT:PC₇₀BM (Chapter 3), PTB7:PC₇₀BM (Chapter 3 and 4), the each thin films were deposited on glass substrate at same spin coating speed above mentioned.

2.4 Device and Thin Film Characterization Methods

2.4.1 Device Characterization Methods.

J-V characteristics (current density-voltage characteristics) of the devices were measured in the dark and under light illumination (AM1.5G 100 mW/cm² illumination) on the ITO side with a 300 W solar simulator (Newport 91160A), using a Keithley 237 source measurement unit. Incident light intensity was varied using neutral density filters (O. D. 0.3 ~ O. D. 2.0). In order to measure temperature dependent J-V characteristics between 100 and 300 K, the solar cells were loaded on to the cold finger of a closed-cycle He cryostat with LakeShore 331 temperature controller.

IPCE (incident photon to conversion efficiency) spectra of the devices have been measured by using a lock-in amplifier (Model 7265, Signal Recovery) a monochromatic light from a xenon lamp through the monochromator (SpectroPro-150, Acton Research Corporation) arrangement.

Impedance characteristics were measured in the frequency range of 100 Hz-10MHz by using an impedance analyzer (HP-4192A) under 100 mW/cm² illumination conditions.

2.4.2 Thin Film Characterization Methods.

UV-Visible absorption spectra were taken with a Beckman DU-70 spectrophotometer.

XRD (x-ray diffraction) studies have been carried out using x-ray diffractometer (New D8 Advance).

AFM (atomic force microscope) was used in order to measure surface morphology and phase of thin films using XE-100 (Park systems).

C-AFM (conductive atomic force microscopy, BRUKER) was performed using PtIr coated cantilevers (PPP-EFM, Nanosensors).

FESEM (field emission scanning electron microscope) images of the prepared thin films have been recorded using Zeiss Supra 55VP.

HRTEM (high resolution transmission electron microscope) images of the prepared thin films have been recorded using a JEM-3010 Electron Microscope.

XPS (X-ray photoelectron spectroscopy, AXIS-HSi) spectra were used to identify the surface elements.

UPS (Ultraviolet photoelectron spectroscopy) measurement was performed using AXIS Ultra DLD (KRATOS Inc.) with He I (21.2 eV) as monochromatic light source.

Optical Constants were performed using spectroscopic ellipsometer (M2000D) by Woollam.

PL (Photoluminescence) spectra of the samples were measured using a Monochromator (SP2150i) and an excitation wavelength 375 nm.

Chapter 3

Inverted Polymer Solar Cells with Doped ZnO as an Electron Extraction Layers

Inverted structures of polymer solar cells have been developed in recent years because of their superior device stability and manufacturing compatibility. In the inverted structure, a high work function metal such as Al, Ag and Au is used as hole collecting electrode, while several n-type metal oxides such as TiO_2 or ZnO is used as a buffer layer due to their relatively high electron mobility, environmental stability and high transparency [22,57]. These buffer layers also help to redistribute the light intensity inside the devices and to protect the active layer from degradation by oxygen or moisture [58]. Among the metal oxides used in inverted solar cells, ZnO is an excellent cathode buffer layer due to its high electron mobility, good

transparency, low cost, non-toxicity, air stability, and hole blocking properties [59-60]. It is well known that the physical characteristics of ZnO thin films depend on the doping and a systematic study of the doping effect is always interesting. The doping of semiconductors with various elements is known to greatly affect many of the basic physical properties of the semiconductor, including its electrical, optical, and structural properties, which are all crucial for most of the practical applications [52,61]. The group-III atoms such as In, Al and Ga have been investigated as n-type dopants for ZnO because they can replace the Zn sites in the ZnO crystal and more than that one free electron is generated, which exhibit not only good conductivities but also better stabilities compared to those of ZnO films [52,62]. In this chapter, we have investigated the effect of In, Al and Ga doping and properties of ZnO thin films (one element doping) as well as IGZO thin films (two element doping) and have fabricated inverted polymer solar cells. Inverted polymer solar cell containing doped ZnO and IGZO as an electron extraction layer with device structure of ITO / doped ZnO and IGZO / PCPDTBT:PC₇₀BM or PTB7:PC₇₀BM or PTB7-Th:PC₇₀BM / MoO₃ / Al has been fabricated and its characteristics have been studied.

3.1 Inverted Polymer Solar Cells with In doped ZnO as an Electron Extraction Layer

In this part, a systematic study has been carried out to understand the effect of In doping on the various properties of the ZnO nanocrystalline thin films. We report about the fabrication of inverted polymer solar cells with a device structure of ITO / In doped ZnO / PCDTBT:PC₇₀BM / MoO₃ / Al utilizing In doped ZnO as an electron extraction layer with different indium concentrations (1.98 %, 4.03 %, 6.74 %, 8.62 % and 10.48 % In).

3.1.1 Structural and Morphological Properties of In doped ZnO

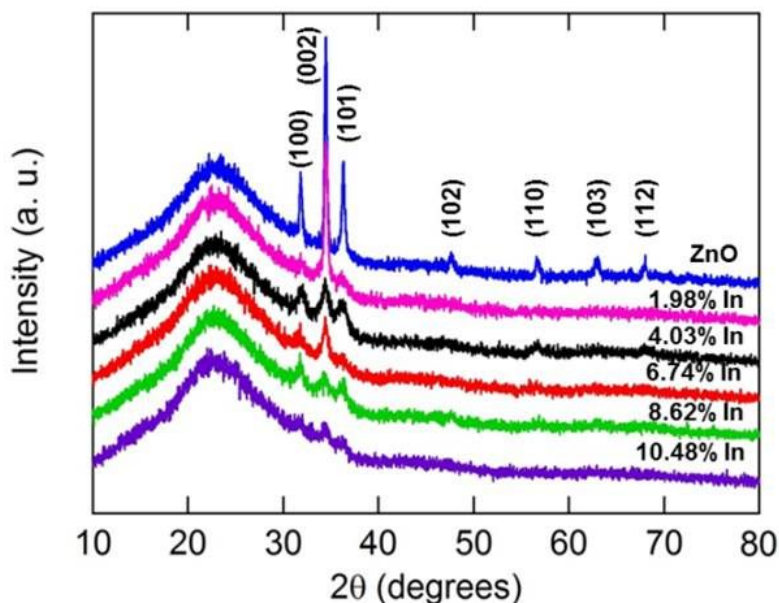


Figure 3.1 X-ray diffraction pattern of ZnO and In doped ZnO films.

Figure 3.1 shows the x-ray diffraction pattern of ZnO and In doped ZnO nanocrystalline thin films. The diffraction peaks at 2θ (degrees) of 31.76 °, 34.36 °, 36.23 °, 47.49 °, 56.61 °, 62.79 ° and 67.90 ° are indexed as (100), (002), (101), (102), (110), (103) and (112) planes corresponding to that of hexagonal wurtzite structure ZnO (space group: P6₃mc). The lattice constants a and c have been determined from interplanar spacing of different (hkl) planes using the relation.

$$(d_{hkl})^{-2} = \frac{4}{3} \frac{h^2 + hk + k^2}{a^2} + \left(\frac{l}{c}\right)^2 \quad (3.1)$$

The lattice constants have been found to be $a = 3.244 \text{ \AA}$ and $c = 5.214 \text{ \AA}$ which are in agreement with the standard JCPDS data (JCPDS No.36-1451). It is observed that the diffraction peaks of the In doped ZnO show a small shift towards higher 2θ values when compared to that of ZnO. This shift may be due to the occupation of indium ions at the zinc sites. The absence of the diffraction peaks of In₂O₃ phase in the pattern implies that indium substitutes for zinc in the prepared In doped ZnO. No other impurity phase is observed, which indicates that the indium ion successfully occupies the lattice site rather than the interstitial ones. The lattice constants have been calculated and are $a = 3.235 \text{ \AA}$ and $c = 5.194 \text{ \AA}$. The diffraction pattern reveals that the In doped ZnO films also exhibits hexagonal wurtzite structure. Doping of indium ions in ZnO does not lead to any structural phase transformation but introduces a lattice contraction. The increase in the diffraction angle corresponds to a reduction in the interplanar spacing (d). Since In³⁺ (0.81 Å) has a larger ionic radius when compared to Zn²⁺ (0.74 Å), the substitution of indium atoms for zinc atoms at their lattice sites results in the decrease of the lattice constant. In the In doped ZnO film the (002) peak has less intensity than the corresponding peak of

ZnO film [63]. This indicates that an increase in In doping content deteriorates the crystallinity of films, which may be due to the formation of stresses because of the difference in size of the Zn and the dopant ions and also due to the segregation of dopant at grain boundaries for high doping concentrations [64]. The full width at half maximum of all the peaks in the In doped ZnO pattern is wider than those of the ZnO. The grain size of ZnO and In doped ZnO films have been calculated using Scherrer's equation.

$$D = \frac{K\lambda}{\beta \cos \theta} \quad (3.2)$$

where, D is the grain size, K is a constant taken to be 0.94, λ is the wavelength of the x-ray radiation, β is the full width at half maximum and θ is the angle of diffraction. The grain size has been calculated and is found to be 22.4, 18.6, 13.7, 11.5, 9.2 and 7.3 nm for ZnO, 1.98 at.% In, 4.03 at.% In, 6.74 at.% In, 8.62 at.% In and 10.48 at.% In doped ZnO films respectively. It is observed that with increase in indium concentration, the grain size and film crystallinity are decreasing. Similar results have been observed by A. Tubtimtae et al., [65]. Similar size reduction in doped nanocrystals has also been observed in other doped nanocrystal systems. T. Ratana et al., [66] have reported that the crystallite size decreased with increasing Al concentration.

Figure 3.2 shows the surface morphology of ZnO and In doped ZnO thin films. It is observed that grains are small and are uniformly distributed throughout the surface. These results indicate that increasing In doping concentration degrades the crystallinity of the ZnO thin films due to the formation of small crystallites in the films. Figure 3.3 shows the energy-dispersive x-ray spectroscopy (EDS) spectra of the ZnO and In doped ZnO films. The EDS spectra confirm the presence of indium

along with zinc and oxygen in the synthesized thin films. The chemical constituents present in the sample according to the EDS analysis are Zn = 49.02 % and O = 50.98 % for ZnO, Zn = 47.84 %, O = 50.18 % for 1.98 at.% In, Zn = 46.05 %, O = 49.92 % for 4.03 at.% In, Zn = 44.60 %, O = 48.66 % for 6.74 at.% In, Zn = 42.81 %, O = 48.57 % for 8.62 at.% In and Zn = 40.93 %, O = 48.59 % for 10.48 at.% In doped ZnO.

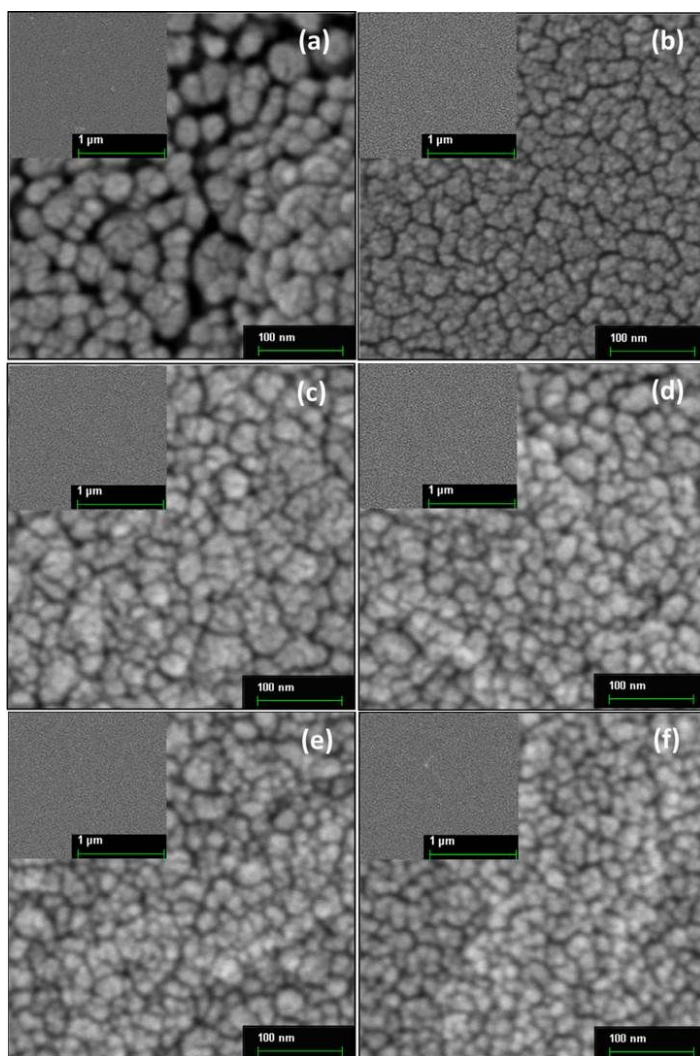


Figure 3.2 FESEM images of (a) ZnO and In doped ZnO, (b) 1.98 at.% In, (c) 4.03 at.% In, (d) 6.74 at.% In, (e) 8.62 at.% In, (f) 10.48 at.% In.

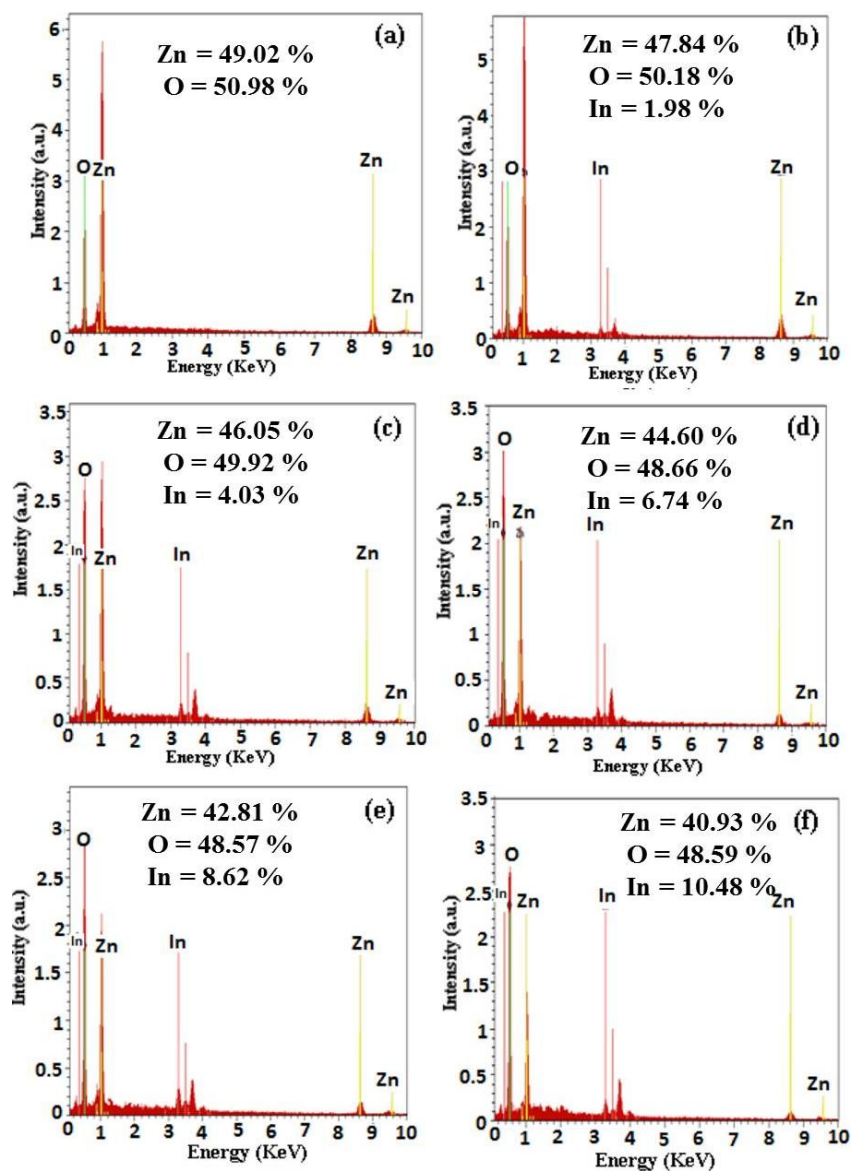


Figure 3.3 EDS spectra of (a) ZnO and In doped ZnO, (b) 1.98 at.% In, (c) 4.03 at.% In, (d) 6.74 at.% In, (e) 8.62 at.% In, (f) 10.48 at.% In.

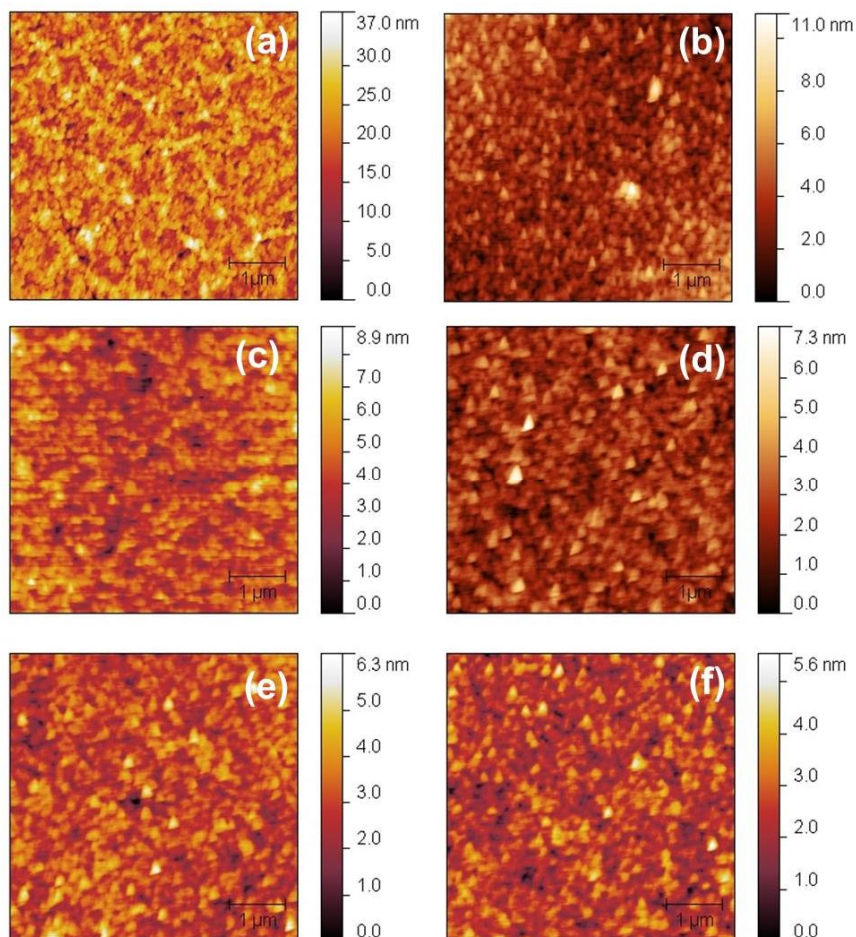


Figure 3.4 AFM images of (a) ZnO and In doped ZnO, (b) 1.98 at.% In, (c) 4.03 at.% In, (d) 6.74 at.% In, (e) 8.62 at.% In, (f) 10.48 at.% In.

Figure 3.4 shows the AFM images of ZnO and In doped ZnO nanocrystalline thin films. The root-mean-square (RMS) surface roughness is found to be 3.97, 1.20, 0.95, 0.78, 0.68 and 0.68 nm for ZnO, 1.98 at.% In, 4.03 at.% In, 6.74 at.% In, 8.62 at.% In and 10.48 at.% In doped ZnO respectively. The surface roughness of the films decreased with incorporation of indium in the doped films and this decrease in roughness is due to the decrease in grain size with increase in doping concentration.

The images also reveal that the films are homogeneous without any cracks and are continuous with very well connected grains.

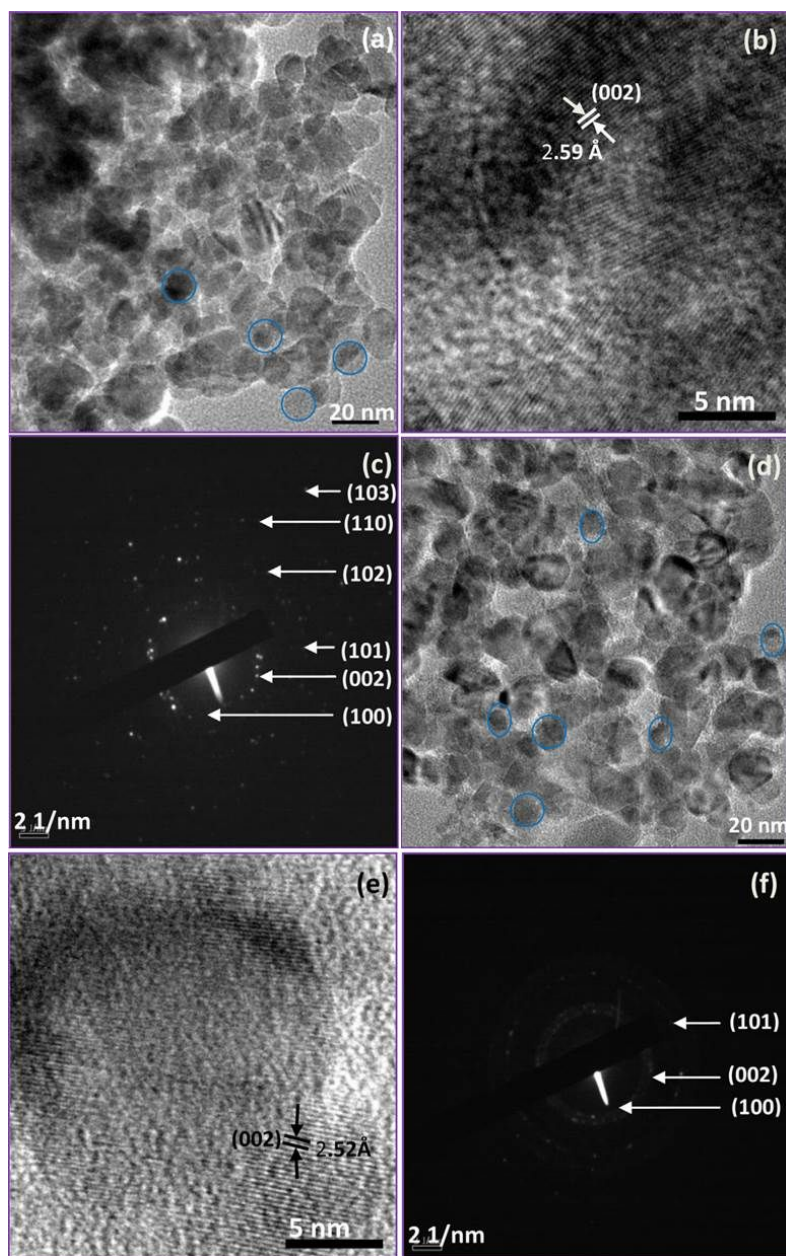


Figure 3.5 HRTEM, SAED images of (a, b, c) ZnO and (d, e, f) 6.74 at.% In doped ZnO.

HRTEM images of ZnO and 6.74 at.% In doped ZnO nanocrystalline thin films are shown in Figure 3.5. Figure 3.5 (a) shows the HRTEM image of ZnO nanocrystalline thin film. It can be seen that most of the individual particles are of spherical shape. The average grain size of ZnO is found to be 21 nm. It can be clearly observed from the HRTEM image (Figure 3.5 (b)) that the interplanar distance is 2.59 Å for ZnO, which corresponds to the (002) plane of the hexagonal ZnO. The HRTEM image of 6.74 at.% In doped ZnO nanocrystalline thin film is shown in Figure 3.5 (d). The average particle size of 6.74 at.% In doped ZnO is about 11 nm, obviously smaller than that of ZnO (21 nm). The interplanar distance of 6.74 at.% In doped ZnO (Figure 3.5 (e)) is found to be 2.52 Å. The lattice spacing of In doped ZnO is slightly less than that of ZnO because of the larger ionic radius of In when compared to that of Zn^{2+} ($r_{\text{In}^{3+}} = 0.81 \text{ Å}$, $r_{\text{Zn}^{2+}} = 0.74 \text{ Å}$). Furthermore, indium ion which exists in ZnO structure as a dopant may tend to create more nucleation centers during the deposition process and as a result the increase in indium content may cause a decrease in crystallite size. The reduction in the crystallite size implies that the indium species play an important role in the growth of the host nanocrystals. The growth rate of nanocrystals is significantly restrained by the adsorption of indium ions during the course of the reaction. The selected area electron diffraction (SAED) pattern exhibits concentric circles revealing that the ZnO (Figure 3.5 (c)) and In doped ZnO (Figure 3.5 (f)) are of nanocrystalline nature made up of small grains. The d spacing values calculated from these images are in close agreement with the values obtained from x-ray diffraction studies. The decrease of interplanar distance and grain size indicates that indium has been really incorporated into the ZnO lattice.

3.1.2 Optical Properties of In doped ZnO

Figure 3.6 shows the optical absorption spectra of ZnO and In doped ZnO films. It is found that the absorption spectra of the In doped ZnO thin films exhibit a blue shift when compared to that of the ZnO thin film. In general the blue shift of the absorption is associated with the increase of the carrier concentration blocking the lowest states in the conduction band, well known as the Burstein-Moss effect [67-68]. Burstein has pointed out that the increase in the number of electrons will make it easy to fill the lower states of the conduction band in the In doped ZnO thin films, which compels the electrons of valence band to transit to the higher states of the conduction band when the In doped ZnO thin films are excited. Corresponding to optical absorption, the UV absorption spectra shifts towards shorter wavelength. The shift of the absorption edge to the shorter wavelength also indicates that the grain size decreases with increasing indium concentration [69]. The fundamental absorption, which corresponds to the electron excitation from the valence band to the conduction band, can be used to determine the nature and value of the optical band gap. The relation between the absorption coefficient (α) and the incident photon energy ($h\nu$) can be written as

$$(\alpha h\nu) = A(h\nu - E_g)^n \quad (3.3)$$

where A is a constant, E_g is the band gap of material, ν is the frequency of the incident radiation, h is the Planck's constant and the exponent n is 0.5 for direct allowed transitions. The optical band gap of the ZnO and In doped ZnO have been determined using equation 3.3

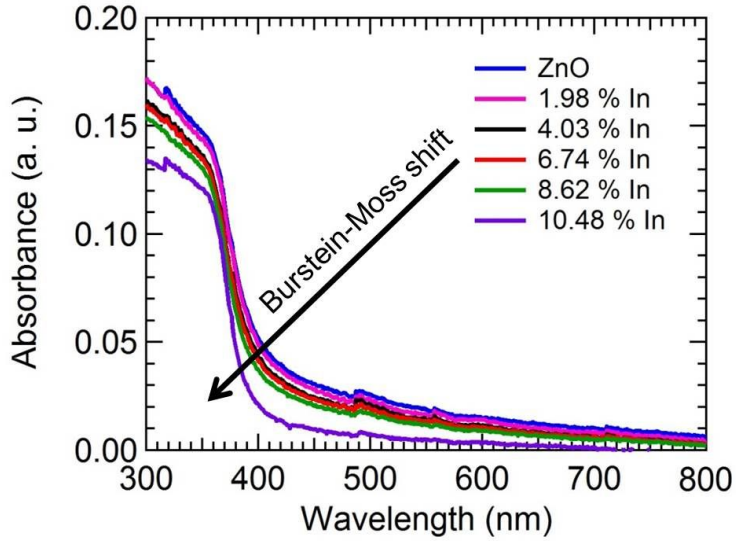


Figure 3.6 Optical absorption spectra of ZnO and In doped ZnO films.

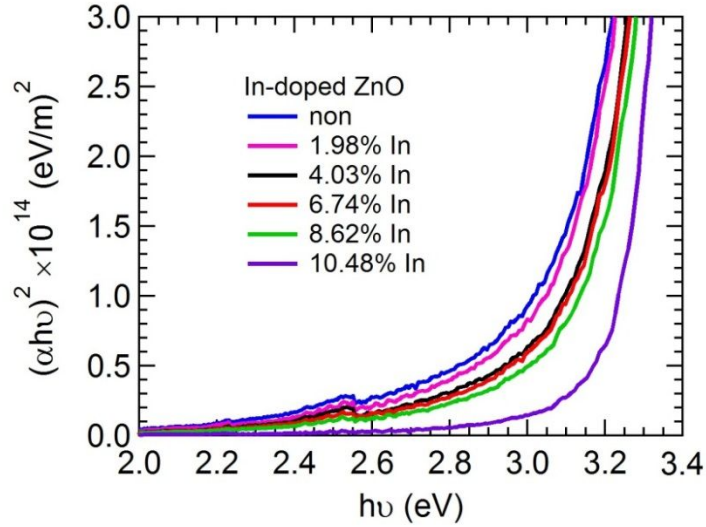


Figure 3.7 Plot of $(\alpha h\nu)^2$ versus $h\nu$ of ZnO and In doped ZnO films

Figure 3.7 shows the $(\alpha h\nu)^2$ versus $h\nu$ plot of ZnO and In doped ZnO thin films. The optical band gap of the ZnO and In doped ZnO thin films have been calculated

by extrapolating the straight linear portion of the plot between $(\alpha h\nu)^2$ and $h\nu$ to meet the energy axis. The band gap has been calculated and is found to be 3.12, 3.14, 3.16, 3.17, 3.19 and 3.23 eV for ZnO, 1.98 at.% In, 4.03 at.% In, 6.74 at.% In, 8.62 at.% In and 10.48 at.% In doped ZnO films respectively. The band gap is observed to increase from 3.12 eV corresponding to the ZnO film to 3.23 eV corresponding to 10.48 at.% In doped ZnO. The band gap of In doped ZnO thin films is larger than that of ZnO thin film and this can be explained by the Burstein-Moss shift. i.e., the Fermi level is lifted into the conduction band of the degenerated semiconductor when ZnO thin films are doped with In, which leads to the energy band broadening effect. A similar variation in the band gap for the doped ZnO thin film with indium has been reported by Young Ran Park et al., [70], which was also attributed to Burstein-Moss shift. It is seen that the slight increase in the optical band gap can be attributed to the decrease in the grain size [71].

3.1.3 Electrical Properties of In-doped ZnO

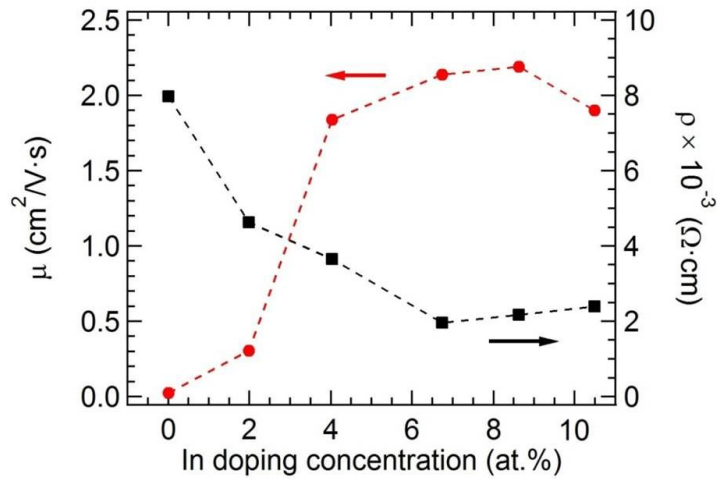


Figure 3.8 Variation of resistivity and electron mobility of ZnO thin films with indium doping concentration.

Figure 3.8 shows the variation of resistivity and electron mobility of ZnO films with indium doping concentration. The electrical resistivity and mobility of the ZnO thin films are $7.98 \times 10^{-3} \Omega\cdot\text{cm}$, $0.024 \text{ cm}^2/\text{V}\cdot\text{S}$ respectively. It is seen that as indium is added to ZnO, the electrical resistivity first decreases and then increases. The resistivity and mobility of In doped ZnO thin films are $4.63 \times 10^{-3} \Omega\cdot\text{cm}$, $0.305 \text{ cm}^2/\text{V}\cdot\text{S}$ for 1.98 at.% In, $3.65 \times 10^{-3} \Omega\cdot\text{cm}$, $1.84 \text{ cm}^2/\text{V}\cdot\text{S}$ for 4.03 at.% In, $1.95 \times 10^{-3} \Omega\cdot\text{cm}$, $2.19 \text{ cm}^2/\text{V}\cdot\text{S}$ for 6.74 at.% In, $2.17 \times 10^{-3} \Omega\cdot\text{cm}$, $2.14 \text{ cm}^2/\text{V}\cdot\text{S}$ for 8.62 at.% and $2.40 \times 10^{-3} \Omega\cdot\text{cm}$, $1.90 \text{ cm}^2/\text{V}\cdot\text{S}$ for 10.48 at.% In. At lower doping concentrations the electrons from the dopant play a dominant role in the film and as less oxygen vacancy scattering occurs, the resistivity decreases. In our case, the grain size was found to be decreasing with increase of doping concentration. Hence grain boundary scattering might have increased. But an initial decrease in resistivity is also observed. Here, the donor action of indium compensated for the grain boundary scattering leading to a reduction of resistivity. A lower resistivity value was obtained for 6.74 at.% In doped ZnO film. The lower resistivity of the film after doping with the optimum indium content can be explained by the fact that indium atom substitute for zinc atom in the crystal lattice and behave as donors and induces native n-type conductivity in ZnO film. Further increase in In doping to above 6.74 at.% raised the resistivity and reduced the mobility. At a higher In doping concentration of above 6.74 %, the disorder produced in the lattice (due to difference in the ionic radius of Zn^{2+} and In^{3+}) increases the efficiency of scattering mechanism such as phonon scattering and ionized impurity scattering which, in turn, causes an increase in resistivity [63]. However, at higher doping concentration (8.62 at.% In and 10.48 at.% In doped ZnO), the resistivity increases because the presence of more dopant atoms form some kind of neutral defects and these neutralized atoms do not contribute free electrons [71]. The effect of grain boundary scattering would

have dominated in the higher doping concentration leading to an increase in resistivity. The mobility initially increases for low doping (1.98 at.% In, 4.03 at.% In and 6.74 at.% In doped ZnO) concentration because grains are fully depleted and traps are partially filled and potential barriers at the grain boundaries have not been formed. As doping concentration (8.62 at.% In and 10.48 at.% In doped ZnO) is increased, potential barrier develops and mobility is decreased, reaching a minimum when barrier height is maximum. As the mobility is not only determined by the grain size and disorder, but also scattering effects, such as electron-electron and electron-ion scattering, it is not possible to give an explicit dependence between the crystallite size and the mobility.

3.1.4 Device Characteristics with In doped ZnO

The current density-voltage (J-V) characteristics of the inverted polymer solar cells fabricated with ZnO and In doped ZnO as an electron extraction layers is shown in Figure 3.9, which has been measured under the light intensity of AM1.5G 100 mW/cm². The short circuit current density (J_{SC}), open circuit voltage (V_{OC}), fill factor (FF), power conversion efficiency (PCE), series resistance (R_s) and shunt resistance (R_{sh}) deduced from J-V curves are summarized in Table 3.1. It is observed that inverted polymer solar cell with ZnO exhibited a power conversion efficiency of 3.63 % with J_{SC} of 8.48 mA/cm², V_{OC} of 0.87 V and a FF of 49.12 %. J-V characteristics of In doped ZnO based inverted polymer solar cells are shown in Figure 3.9 (a). Inverted polymer solar cell incorporating electron extraction layer of 1.98 at.% In doped ZnO exhibits a significantly enhanced photovoltaic response with J_{SC} of 10.61 mA/cm², V_{OC} of 0.87 V, FF of 50.84 % and thus an enhanced PCE of 4.71 %. The efficiency of the inverted polymer solar cell fabricated with 4.03 at.%

In doped ZnO was found to be 5.28 % with J_{SC} of 11.92 mA/cm², V_{OC} of 0.88 V and FF of 50.18 %. The polymer solar cell fabricated with the 6.74 at.% In doped ZnO exhibited the best photovoltaic performance among all the devices, with PCE of 5.58 %, J_{SC} of 12.28 mA/cm², V_{OC} of 0.88 V and FF of 51.72 %. As shown in Figure 3.9 (a) and Table 1, increasing the In concentration from 1.98 to 6.74 at.% In doped ZnO leads to improvement in the solar cell performance. The R_s and R_{sh} are calculated from inverse gradient of the J-V curve. The R_s decreases from 9.46 to 7.78 $\Omega \cdot \text{cm}^2$ and R_{sh} increases from 719.26 to 753.86 $\Omega \cdot \text{cm}^2$. The R_s becomes smaller and R_{sh} becomes larger with the interfacial layers, which is one of the reasons that the device performance gets improved. The results indicate that power conversion efficiency of the ZnO based devices can be easily improved through In doping. However, it is also noted that further increase of the In doping concentration to more than 6.74 at.% leads to the decrease of the device performance with lower J_{SC} , V_{OC} and FF. As the In concentration is increased from 8.62 to 10.48 at.%, the J_{SC} decreases from 12.09 to 11.41 mA/cm², R_{sh} decreases from 353.15 to 328.03 $\Omega \cdot \text{cm}^2$. R_s increased from 11.01 to 15.05 $\Omega \cdot \text{cm}^2$ and as a result, the power conversion efficiency decrease from 5.09 to 4.80 %. The reduction in device performance is because higher doping concentration introduces saturated electron barrier height and more electron trapping sites, which is disadvantageous for photocurrent transport. The IPCE spectra of inverted polymer solar cells fabricated with electron extraction layers of ZnO and In doped ZnO are shown in Figure 3.9 (b). The inverted polymer solar cells with 6.74 at.% In doped ZnO exhibited a maximum IPCE of 68 %, which is consistent with its high photocurrent. This indicates that the In doped ZnO device has better carrier extraction and carrier collection efficiency. The enhanced IPCE could result from an improved interfacial charge extraction. The J_{SC} values have been calculated by IPCE data with an AM1.5G reference spectrum. The J_{SC} is found

to be 8.30, 10.20, 11.18, 12.03, 11.68 and 10.97 mA/cm² for ZnO, 1.98 at.% In, 4.03 at.% In, 6.74 at.% In, 8.62 at.% In and 10.48 at.% In doped ZnO respectively. These values match well with those obtained from J-V measurement (Table 3.1). The increase in J_{SC} is also reflected in the incident photon to current conversion efficiency (IPCE) spectra in the spectral range of 300-800 nm.

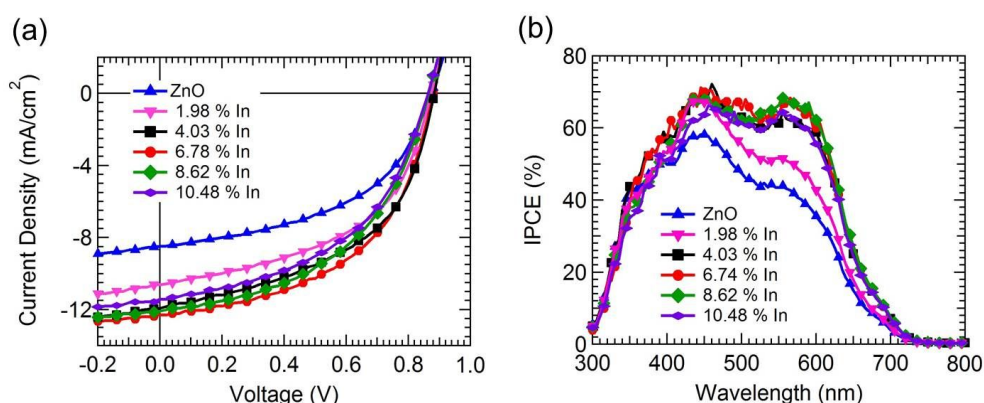


Figure 3.9 The current density-voltage (J-V) characteristics of the ZnO and In doped ZnO inverted polymer solar cells and (b) the IPCE spectra.

Table 3.1 Summary of the performance parameters of inverted polymer solar cells with ZnO and In doped ZnO as an electron extraction layer.

	ZnO	In doped ZnO				
		1.98 at.%	4.03 at.%	6.74 at.%	8.62 at.%	10.48 at.%
J _{SC} (mA/cm ²)	8.48	10.61	11.92	12.28	12.09	11.41
V _{OC} (V)	0.87	0.87	0.88	0.88	0.86	0.86
FF (%)	49.12	50.84	50.18	51.72	48.68	48.78
PCE (%)	3.63	4.71	5.28	5.58	5.09	4.80
R _s (Ω·cm ²)	16.31	9.46	7.32	7.21	11.01	15.05
R _{sh} (Ω·cm ²)	567.27	719.26	724.63	753.86	353.15	328.03

3.2 Inverted Polymer Solar Cells with Al doped ZnO as an Electron Extraction Layer

In this part, we have investigated the effects of Al doping on the structural and electrical properties of ZnO thin films and the photovoltaic performance of inverted polymer solar cells with the structure of ITO / Al doped ZnO / PCDTBT:PC₇₀BM / MoO₃ / Al utilizing Al doped ZnO as an electron extraction layer with different aluminum concentrations (1.98 at.%, 3.79 at.%, 5.83 at.%, 7.58 at.% and 9.91 at.% Al).

3.2.1 Structural and Morphological Properties of Al-doped ZnO

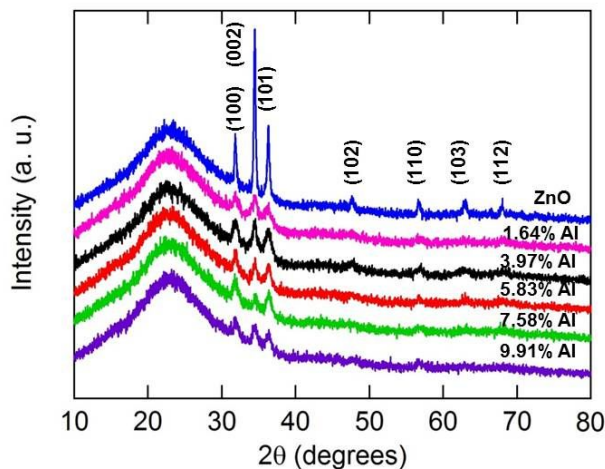


Figure 3.10 X-ray diffraction patterns of ZnO and Al doped ZnO with different Al doping concentration.

Figure 3.10 shows the x-ray diffraction pattern of ZnO and Al doped ZnO films with various Al concentrations. All the diffraction peaks can be indexed to the hexagonal phase of ZnO with lattice constants of $a=3.251 \text{ \AA}$ and $c=5.210 \text{ \AA}$, in good

agreement with the standard values (JCPDS No. 36-1451). The (002) diffraction peak is shifted to a higher angle in the Al doped ZnO thin films, compared to ZnO, due to the lattice distortion introduced by the substitution of Al^{3+} for Zn^{2+} . The lattice constants of the Al doped ZnO thin films ($a = 3.231 \text{ \AA}$ and $c = 5.193 \text{ \AA}$) are observed to be slightly smaller than those of ZnO because the ionic radius of aluminum (0.054 nm) is smaller than that of zinc (0.074 nm) [72]. As the Al doping concentration increases, the intensity of the diffraction peaks decreases and the full width at half maximum (FWHM) of the peaks increases, indicating that the film crystallinity is deteriorated. The reduced crystallinity arises from the incorporation of Al into ZnO [73]. The grain size of ZnO and Al doped ZnO is determined using the Scherrer's equation from equation 3.2. The grain size is found to be 22.5 nm for ZnO and 15.2, 14.7, 13.0, 12.5 and 11.6 nm for the Al doped ZnO film with the Al concentration of 1.64, 3.97, 5.83, 7.58 and 9.91 at.%, respectively. The HRTEM images of ZnO and 5.83 at.% Al doped ZnO are shown in Figure 3.11. It can be seen from Figure 3.11 (a, d) that the grains are spherical in nature with little agglomeration and good crystallinity. The average grain size of ZnO is found to be about 22 nm. The interplanar lattice spacing of the planes seen (Figure 3.11 (b)) in the micrograph of ZnO is found to be 2.59 Å and this corresponds to the (002) plane of hexagonal ZnO. The selected area electron diffraction (SAED) pattern (Figure 3.11 (c)) of film is indexed on the basis of hexagonal ZnO, which is in good agreement with XRD results. The lattice spacing of 5.83 at.% Al doped ZnO (Figure 3.11 (e)) is 2.53 Å and this is slightly less than that of ZnO (2.59 Å) because of the small ionic radius of Al^{3+} when compared to that of Zn^{2+} ($\text{Al} = 0.054 \text{ nm}$, $\text{Zn} = 0.074 \text{ nm}$). The average grain size of 5.83 at.% Al doped ZnO film has been obtained as 13 nm. The SAED pattern exhibits concentric circles revealing that the 5.83 at.% Al doped ZnO (Figure 3.11 (f)) is of nanocrystalline nature with the presence of small

grains. The rings in the image correspond to the (100), (002) and (101) planes of the hexagonal phase.

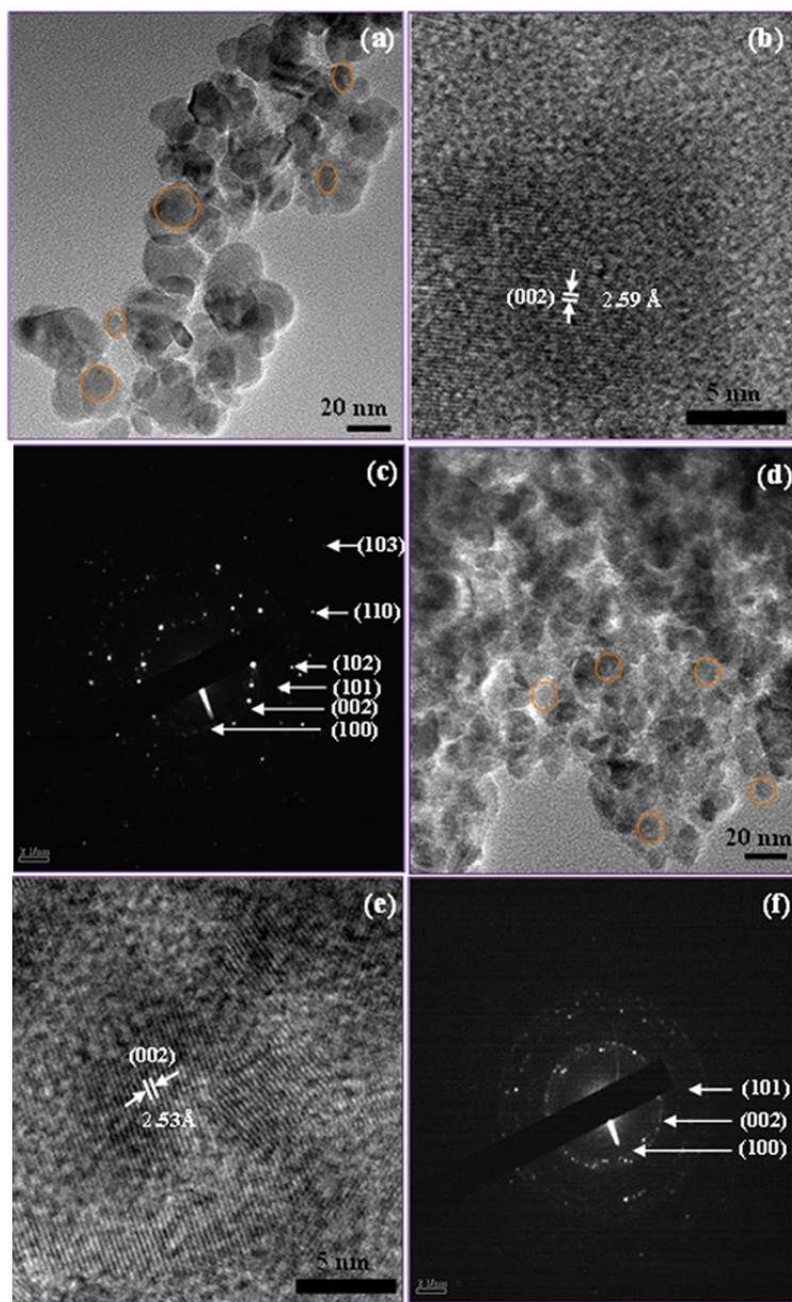


Figure 3.11 HRTEM images of (a, b, c) ZnO and (d, e, f) 5.83 at.% Al doped ZnO

3.2.2 Electrical Properties of Al doped ZnO

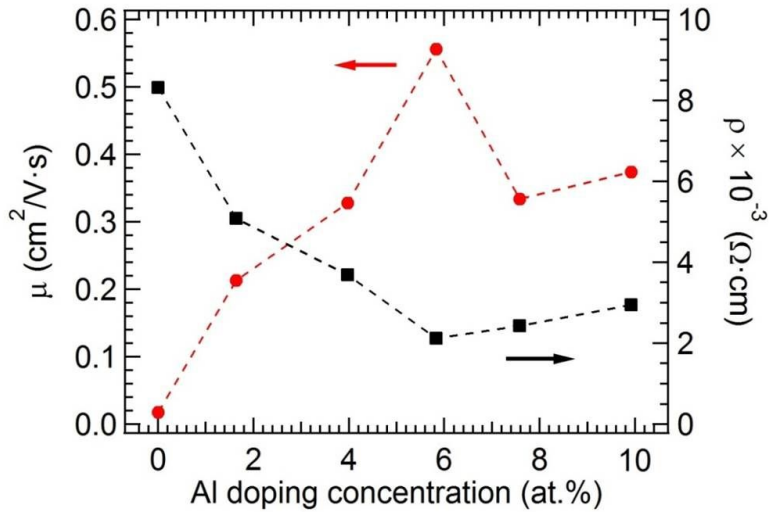


Figure 3.12 Variation of resistivity and electron mobility of ZnO thin films with aluminum doping concentration.

Figure 3.12 shows the variation of resistivity and electron mobility with doping concentration of Al doped ZnO films. Overall the resistivity and mobility of Al doped ZnO is found to be lower and higher respectively than that of ZnO. It is observed that the resistivity decreases and mobility increases first as the Al doping concentration increases up to 5.83 at.% (from $8.3 \times 10^{-3} \Omega\cdot\text{cm}$ to $2.1 \times 10^{-3} \Omega\cdot\text{cm}$ of resistivity and $0.018 \text{ cm}^2/\text{V}\cdot\text{s}$ to $0.556 \text{ cm}^2/\text{V}\cdot\text{s}$ of mobility). These results indicate that one free electron is obtained from one zinc atom replacement and carrier concentration increases with aluminum concentration because small amount of aluminum is ionized into Al^{3+} and replaces Zn^{2+} . Then, the resistivity increases and mobility decreased with further increase of the Al doping concentration, because the extra aluminum atoms might not occupy the correct places inside ZnO lattice due to

the limited solubility of aluminum inside ZnO matrix [74]. This introduces lattice distortion and they scatter electrons.

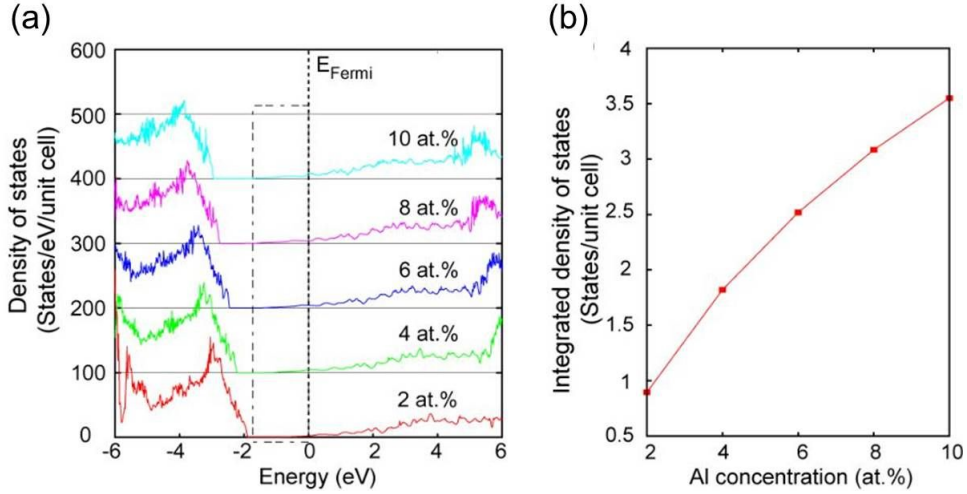


Figure 3.13 (a) The density of states (DOS) for the Al doped ZnO with various Al concentration where the Fermi level is set to zero, (b) The sum of conduction bottom states in Al doped ZnO

Figure 3.13 shows the first principles calculation result of the electronic structures and number of electrons, respectively, while Al doping concentration increases from 2 at.% up to 10 at.%, which is qualitatively consistent with the experimental result. Conductivity is basically determined by the following equation:

$$\sigma = ne\mu_e \quad (3.4)$$

where σ electrical conductivity, n is the number density of electrons for n-type semiconductor, e is the elementary charge, and μ_e is the electron mobility of bulk semiconductor, respectively. In order to understand the effect of Al concentration on the electronic structures, first-principles calculation is carrier out using VASP [75].

The electron-ion interactions were described by the projector-augmented wave pseudopotentials [76] while for the exchange correlation energies between electrons, the generalized-gradient approximation was employed [77]. To study Al doped ZnO structures, the unit cell of ZnO was expanded to a supercell with 96 atoms. A substitutional Al atom was considered to simulate doped system and doping concentrations were varied from 2 at.% to 10 at.%. Figure 3.13 (a) shows the rigid shift of the Fermi-level toward the conduction-band and the increase of the DOS at the Fermi-level as Al concentration increases. From the analysis of the spatial charge distribution, we found that the states near the conduction bottom were delocalized over the whole system and mainly distributed over Zn p and Al s. The integration of DOS at the conduction bottom is shown in Figure 3.13 (b), which is proportional to the number density of electrons so that electrical conductivity increase is expected. As a result, the higher Al doping concentration is to ZnO, the more energy states can be found at the conduction band edge. It occurs higher number density of electrons and results in conductivity augmentation [78]. Although the energy states of electrons at 10 at.% are the higher than other cases in the first principles calculation, the highest conductivity is shown at 5.83 at.% in the experimental result. It is because conductivity is also limited by electron mobility which is affected by the electron scattering that can make electron mobility at 10 at.% lower than that at 5.83 at.%.

3.2.3 Device Characteristics with Al doped ZnO

Figure 3.14 (a) and (b) show the photocurrent density-voltage characteristics and the IPCE spectra of inverted PCDTBT:PC₇₀BM solar cells with ZnO and the Al doped ZnO as an electron extraction layer. The J_{SC} , V_{OC} , FF, and PCE are plotted in

Figure 3.14 (c) and (d) as a function of the Al doping concentration. Table 3.2 summarizes all the PV parameters including the series resistance (R_s) and shunt resistance (R_{sh}) for various Al doping concentrations. The overall device performance of Al doped ZnO was found to be better compared to the ZnO device. Especially, when the ZnO was doped with 5.83 at. % of Al, where the resistivity shows a minimum, the device exhibited the highest J_{SC} , FF and PCE values: $J_{SC} = 9.94 \text{ mA/cm}^2$, $V_{OC} = 0.91 \text{ V}$, FF = 61.95 %, and PCE = 5.60 %. Moreover, R_{sh} increased from 497.21 to 957.78 $\Omega \cdot \text{cm}^2$ while R_s was almost same as that of the device fabricated using ZnO. The FF improved from 48.95 to 61.59 when 5.83 at.% Al doped ZnO was used. These improvement of the PV performance for the devices with the Al doped ZnO as an electron extraction layer can be attributed to the combined effects of the low resistivity and improved electron extraction capability.

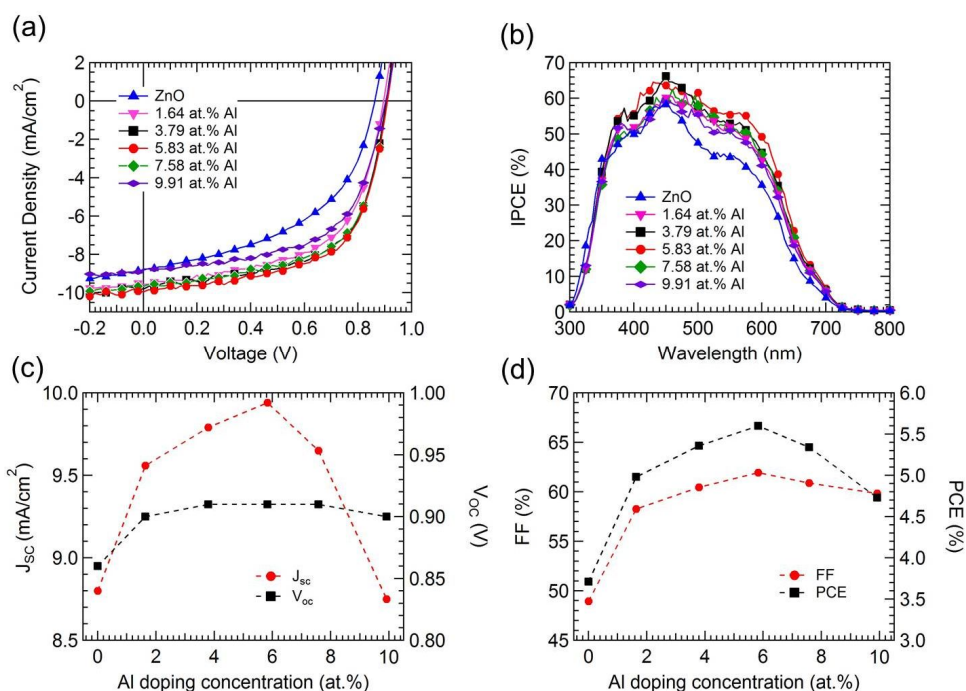


Figure 3.14 (a) Current density-voltage characteristics, (b) IPCE spectra of the inverted polymer solar cell with the ZnO and Al doped ZnO with different Al

doping concentration (c) J_{SC} and V_{OC} (d) FF and PCE as a function of Al doping concentration

Table 3.2 Device performance of the inverted polymer solar cell with ZnO and Al doped ZnO with different Al doping concentration under AM1.5G illumination with 100 mW/cm² light intensity.

	ZnO	Al doped ZnO				
		1.64 at. %	3.79 at. %	5.83 at. %	7.58 at. %	9.91 at. %
J_{SC} (mA/cm ²)	8.80	9.56	9.79	9.94	9.65	8.75
V_{OC} (V)	0.86	0.90	0.91	0.91	0.91	0.90
FF (%)	48.39	58.27	60.46	61.95	60.88	59.84
PCE (%)	3.71	4.98	5.36	5.60	5.34	4.73
R_s ($\Omega \cdot \text{cm}^2$)	15.53	7.12	6.61	6.59	6.40	7.78
R_{sh} ($\Omega \cdot \text{cm}^2$)	479.22	671.23	907.41	957.78	830.51	801.05

3.3 Inverted Polymer Solar Cells with Ga Doped ZnO as an Electron Extraction Layer

Gallium has an ionic radius of 0.62 Å and a covalent radius of 1.26 Å, which are the closest to those of Zn (0.74 and 1.31 Å) [79]. The covalent bond length of Ga-O (1.92 Å) is close to that of Zn-O (1.97 Å), which results in less lattice deformation in ZnO when Ga substitutes for Zn [80]. In this part, inverted polymer solar cells with ZnO and Ga doped ZnO as an electron extraction layers have been systematically studied using low band gap polymers based on PCDTBT:PC₇₀BM and PTB7:PC₇₀BM. The energy levels of the component materials for inverted polymer solar cells are shown in Figure 3.15. When light irradiates the photoactive layer of the solar cells through the ITO electrode, the active layer will absorb photons to produce excitons and the excitons will diffuse towards and dissociate at the PCDTBT:PC₇₀BM interface into electrons in the lowest unoccupied molecular orbital (LUMO) of the acceptor PC₇₀BM and holes in the highest occupied molecular orbital (HOMO) of the donor PCDTBT. Since the LUMO level of ZnO and Ga doped ZnO (4.06 ~ 4.16 eV) is similar as that of PC₇₀BM (4.3 eV), electrons can easily transport to the ITO electrode through ZnO. As the HOMO level of ZnO and Ga doped ZnO (7.06 ~ 7.26 eV) are much lower than that of PCDTBT (5.5 eV) and PTB7 (5.15 eV), so that it blocks the hole transport from PCDTBT and PTB7 to the ITO electrode. The HOMO level of MoO₃ (5.3 eV) is very close to the HOMO level of PCDTBT and PTB7, and this facilitates the hole transfer to the Al electrode through MoO₃. While the relatively high-lying LUMO of MoO₃ (2.3 eV) prevents the electron transfer from PC₇₀BM to the Al electrode.

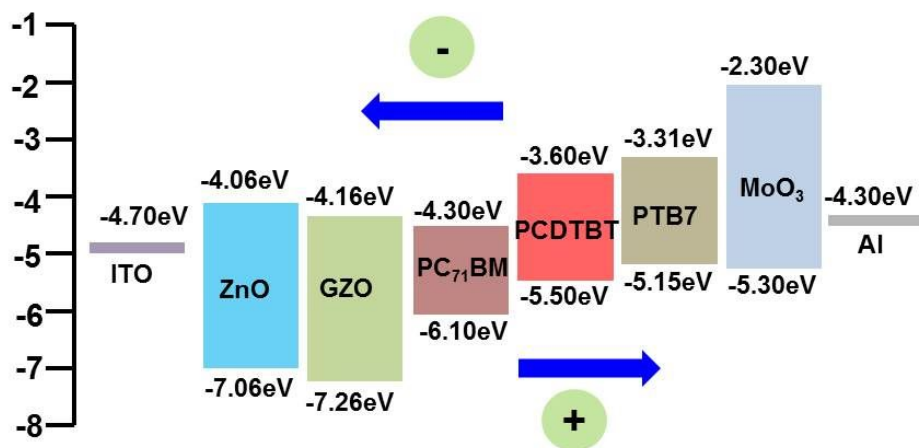


Figure 3.15 Energy level diagrams of inverted polymer solar cells

3.3.1 Optical Properties of Organic Materials and Ga doped ZnO

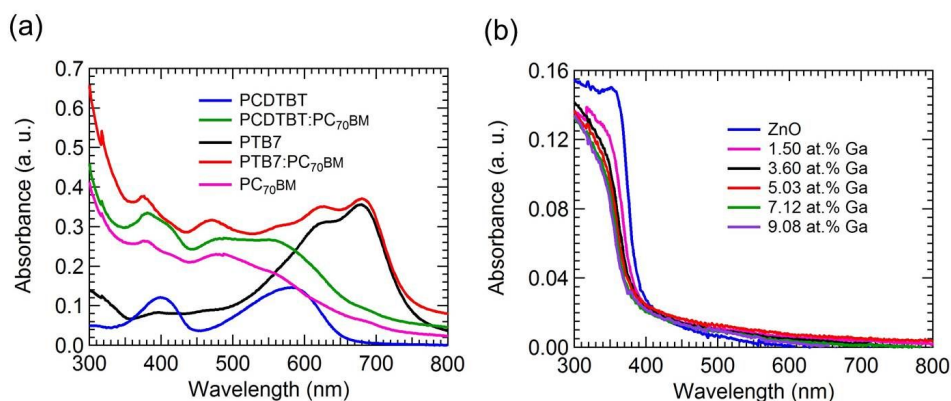


Figure 3.16 Absorption spectra of (a) PCDTBT, PTB7, PC₇₀BM, and composite of PCDTBT:PC₇₀BM and PTB7:PC₇₀BM films (b) ZnO and Ga doped ZnO films with various Ga doping concentration

Figure 3.16 (a) shows the absorption spectra of PCDTBT, PTB7, PC₇₀BM, composite of PCDTBT:PC₇₀BM and PTB7:PC₇₀BM films. PCDTBT shows absorption from 400 to 700 nm and PC₇₀BM shows absorption from 400 nm to 800

nm. The absorption spectrum of the PCDTBT:PC₇₀BM composite is the superposition of PCDTBT and PC₇₀BM which implies that both PCDTBT and PC₇₀BM will contribute photocurrent for polymer solar cells fabricated using PCDTBT:PC₇₀BM. PTB7 shows strong absorption from 540 to 750 nm. However the absorption from 300 to 500 nm is relatively weak. To compensate the absorption of PTB7, PC₇₀BM, which has strong absorption in the visible range, is used as the acceptor. The resulting PTB7:PC₇₀BM blend film exhibits a strong absorption covering a range from 300 to about 800 nm. The absorption spectra of ZnO and Ga doped ZnO with different doping concentrations are shown in Figure 3.16 (b). Absorption spectra of Ga doped ZnO show that the absorption edge is slightly shifted towards the shorter wavelength (blue shift) when compared to ZnO. This is mainly attributed to the Burstein-Moss effect, since the absorption edge of a degenerate semiconductor is shifted to shorter wavelengths with increasing carrier concentration [81].

3.3.2 Electrical Properties of Ga doped ZnO

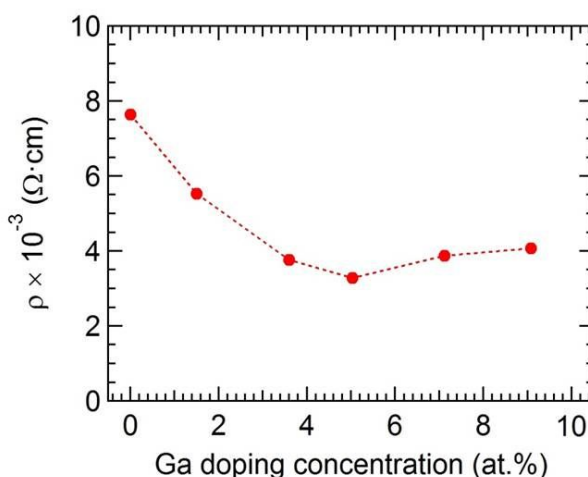


Figure 3.17 Variation of resistivity of ZnO films with Ga doping concentration

It is well known that the electrical properties of the interfacial layers are very important for the performance of the devices because they will affect charge extraction at the interface. Figure 3.17 shows the variation of resistivity of ZnO films with Ga doping concentration. The resistivity is found to be 7.63, 5.53, 3.76, 3.27, 3.87 and $4.06 \times 10^{-3} \Omega\cdot\text{cm}$ for ZnO, 1.50, 3.60, 5.03, 7.12 and 9.08 at.% Ga doped ZnO. The resistivity values of Ga doped ZnO films are small when compared to that of ZnO. It is observed that the resistivity decreases continuously as the Ga concentration is increased up to 5.03 at.%, beyond which the resistivity was found to increase again. The trend of these results is almost similar as compared to In and Al doped ZnO above mentioned. At lower doping concentrations the electrons from the dopant play a dominant role in the film and as less oxygen vacancy scattering occurs, the resistivity decreases. At a higher Ga doping concentration of above 5.03 at.%, the disorder produced in the lattice (due to difference in the ionic radius of Zn^{2+} and Ga^{3+}) increases the efficiency of scattering mechanisms such as phonon scattering and ionized impurity scattering which, in turn, causes an increase in resistivity [82-83]. However, at higher doping concentration, the resistivity increases because an increase in the number of dopant atoms leads to some kind of neutral defects and these neutralized Ga atoms do not contribute free electrons [84].

3.3.3 Device Characteristics with Ga doped ZnO

The current density-voltage (J-V) characteristics of the inverted polymer solar cells based on PCDTBT:PC₇₀BM fabricated using ZnO and Ga doped ZnO are shown in Figure 3.18 (a) and this has been measured under 100 mW/cm² air mass 1.5 global (AM1.5G) illumination. The solar cell parameters in terms of the short circuit current density (J_{SC}), open circuit voltage (V_{OC}), fill factor (FF), power

conversion efficiency (PCE), series resistance (R_s) and shunt resistance (R_{sh}) are summarized in Table 3.3. The PCDTBT:PC₇₀BM based device with ZnO exhibits a J_{SC} of 8.85 mA/cm², V_{OC} of 0.86 V, FF of 50.27 % and PCE of 3.72 %. The PCDTBT:PC₇₀BM based inverted polymer solar cell with 5.03 at.% GZO exhibited the best photovoltaic performance among all the devices with a PCE of 5.56 %, J_{SC} of 10.46 mA/cm², V_{OC} of 0.90 V and FF of 59.03 %. The overall device performance of Ga doped ZnO was found to be better when compared to the ZnO based device. The incident photon to current conversion efficiency (IPCE) spectra of PCDTBT: PC₇₀BM based devices are shown in Figure 3.18 (b). The Ga doped ZnO layers exhibited a substantially enhanced response from 350 to 650 nm as compared with that of ZnO. The maximum IPCE value of the 5.03 at.% Ga doped ZnO based device is 68 % in comparison with 55 % for the ZnO device. The IPCE spectra are consistent with the measured J_{SC} in the devices. The J-V characteristics of the PTB7:PC₇₀BM based inverted polymer solar cells are shown in Figure 3.18 (c). The 5.03 at.% Ga doped ZnO based devices shows photovoltaic performance with a J_{SC} of 14.96 mA/cm², V_{OC} of 0.75 V, FF of 64.9 5% and PCE of 7.34 %. As shown in Figure 3.18 (c) and Table 3.3, increasing the Gallium concentration from 1.50 to 5.03 at.% Gallium leads to improvement of the solar cell performance. The R_s decreases from 10.81 to 6.94 $\Omega \cdot \text{cm}^2$ and R_{sh} increases from 665.51 to 1809.52 $\Omega \cdot \text{cm}^2$. The decrease in R_s indicates the electron collection and transportation benefits from the high quality contact between the PTB7:PC₇₀BM active layer and Ga doped ZnO layer. The decreased R_s and increased R_{sh} contribute to the device performance by improving the FF. From Table 3.3, it is observed that a further increase of the doping concentration to 7.12 and 9.08 at.% Gallium leads to increased R_s . The increased R_s (10.45 to 12.75 $\Omega \cdot \text{cm}^2$) leads to the decrease of FF from 60.40 to 58.36 % respectively. It is evident that this decrease in FF results in the decrease of the PCE

from 5.13% to 4.86 %. The IPCE spectra of PTB7:PC₇₀BM based inverted polymer solar cells are shown in Figure 3.18 (d). It is observed that the 5.03 at.% Ga doped ZnO device showed a maximum IPCE of 70 %, which is higher than 57 % of the ZnO device. The J_{SC} values have been calculated by IPCE data with an AM1.5G reference spectrum. The J_{SC} is found to be 13.77, 13.87, 14.74, 15.42, 14.43 and 13.72 mA/cm² for ZnO, 1.5, 3.60, 5.03, 7.12 and 9.08 at.% Ga doped ZnO respectively. These values match well with those obtained from J-V measurement (Table 3.3). The dark J-V characteristics shown in Figure 3.18 (e) and (f) shows that the Ga doped ZnO device exhibited excellent diode characteristics and lower leakage current under reverse bias than the device based on the ZnO.

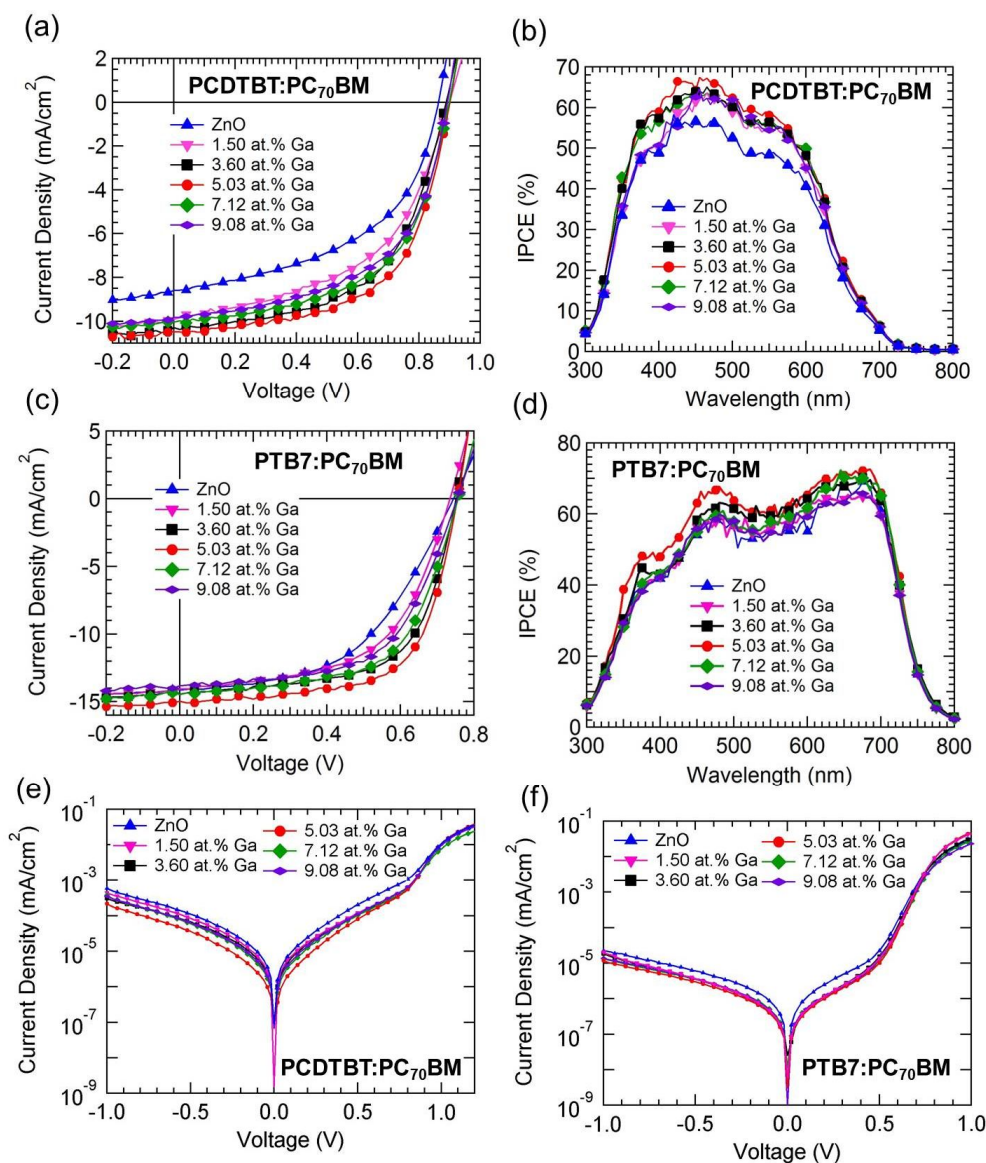


Figure 3.18 (a) J-V characteristics and (b) IPCE spectra of PCDTBT:PC₇₀BM devices (c) J-V characteristics and (d) IPCE spectra of PTB6:PC₇₀BM devices (e) dark J-V characteristics of PCDTBT:PC₇₀BM devices (f) dark J-V characteristics of PTB7:PC₇₀BM devices

Table 3.3 Device performance of inverted structure with different active layers using ZnO and Ga doped ZnO with different Ga doping concentration.

PCDTBT :PC ₇₀ BM	ZnO	Ga-doped ZnO				
		1.50 at. %	3.60 at. %	5.03 at. %	7.12 at. %	9.08 at. %
J _{SC} (mA/cm ²)	8.85	9.91	10.30	10.46	10.04	9.82
V _{OC} (V)	0.86	0.90	0.89	0.90	0.90	0.89
FF (%)	50.27	50.66	56.47	59.03	56.91	55.43
PCE (%)	3.72	4.51	5.17	5.56	5.13	4.86
R _s (Ω·cm ²)	15.40	7.55	7.03	6.81	7.73	8.64
R _{sh} (Ω·cm ²)	366.43	451.24	810.24	1083.42	707.96	660.93
PTB7 :PC ₇₀ BM	ZnO	Ga-doped ZnO				
		1.50 at. %	3.60 at. %	5.03 at. %	7.12 at. %	9.08 at. %
J _{SC} (mA/cm ²)	14.14	14.04	14.45	14.96	14.48	13.82
V _{OC} (V)	0.74	0.74	0.75	0.75	0.75	0.75
FF (%)	50.44	56.20	62.34	64.95	64.95	58.36
PCE (%)	5.31	5.80	6.77	7.34	7.34	6.08
R _s (Ω·cm ²)	17.38	10.81	7.61	6.94	6.94	12.75
R _{sh} (Ω·cm ²)	382.07	655.51	745.82	1809.52	1288.75	733.19

3.3.4 Structural and Morphological Properties of Ga doped ZnO

Another factor influencing the performance of these devices is the interfacial morphology properties. Figure 3.19 shows the surface morphology of ZnO and Ga doped ZnO thin films. It is observed that grains are small and are uniformly distributed throughout the surface. These results indicate that increasing Ga doping concentration degrades the crystallinity of the ZnO thin films due to the formation of small crystallites in the films.

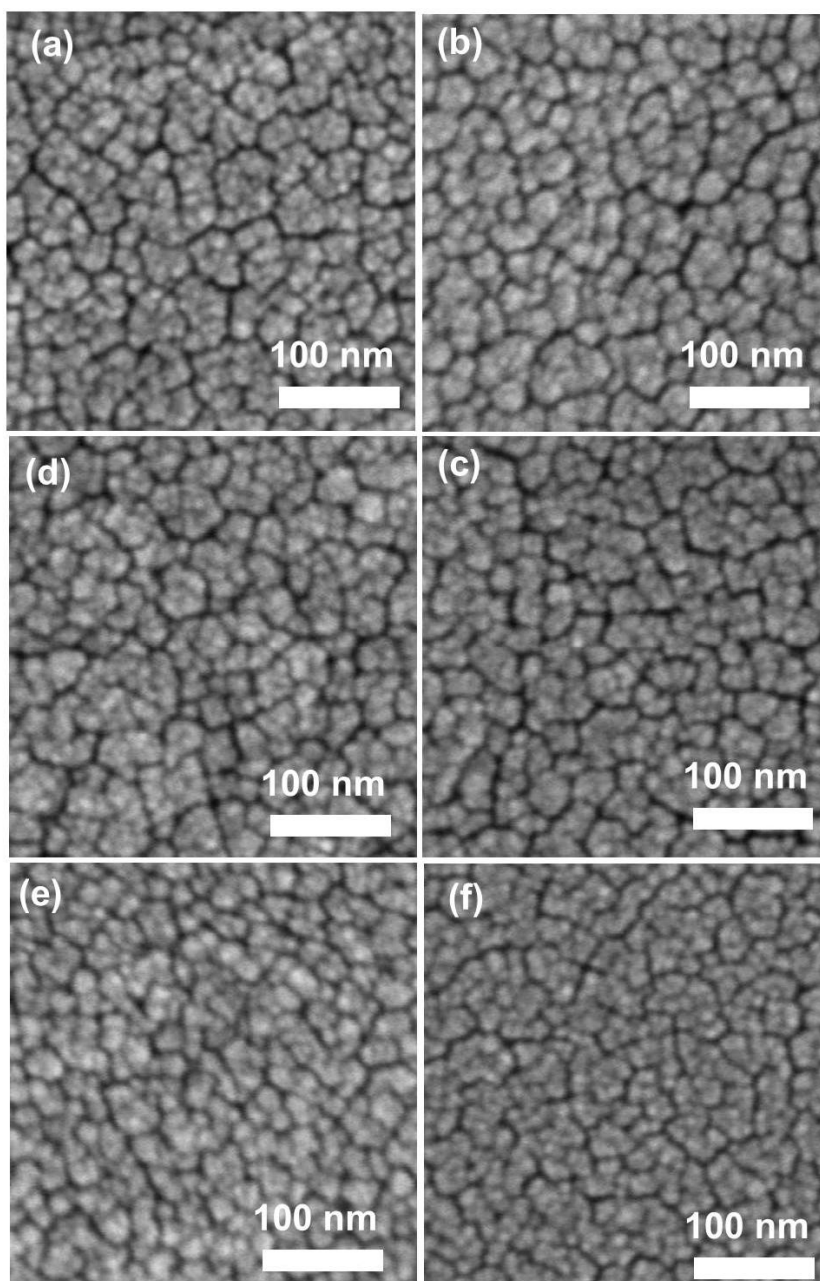


Figure 3.19 FESEM images of (a) ZnO and Ga doped ZnO, (b) 1.50 at.% Ga, (c) 3.60 at.% Ga, (d) 5.03 at.% Ga, (e) 7.12 at.% Ga, (f) 9.08 at.% Ga

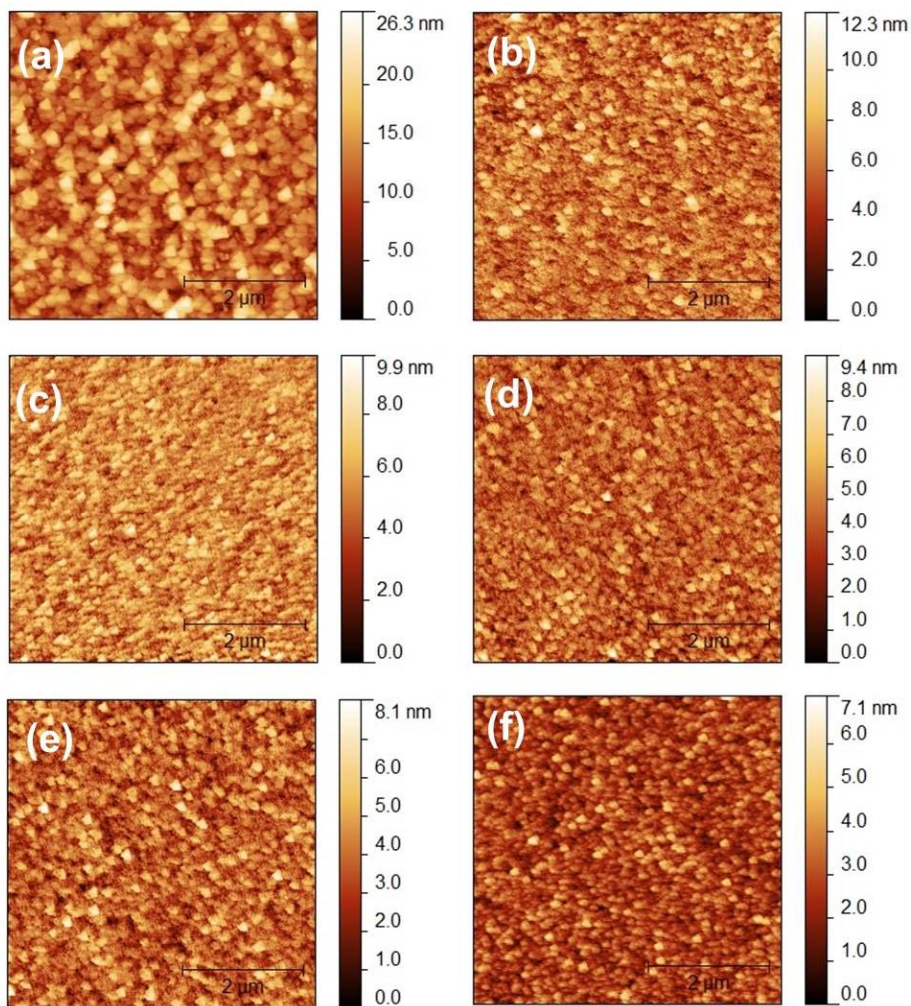


Figure 3.20 AFM images of (a) ZnO and Ga doped ZnO, (b) 1.50 at.% Ga, (c) 3.60 at.% Ga, (d) 5.03 at.% Ga, (e) 7.12 at.% Ga, (f) 9.08 at.% Ga

The surface topography of the interfacial layer may influence the electron extraction layer/active layer contact. The atomic force microscopy (AFM) images of ZnO and Ga doped ZnO films with different doping concentrations are shown in Figure 3.20. It reveals that the films are uniform without any cracks and are continuous with very well connected grains. The root-mean-square (RMS) surface

roughness is found to be 2.69, 1.12, 0.83, 0.82, 0.80 and 0.76 nm for ZnO, 1.50, 3.60, 5.03, 7.12 and 9.08 at.% Ga doped ZnO respectively. The smoother surface should enable a more uniform interfacial contact between the electron extraction layers and active layers, which could increase the electron extraction efficiency. The higher surface roughness may indicate non uniform coverage, which may in turn affect the contact resistance. It is observed that the morphology improvement of the electron extracting interface after doping is responsible for the better performance of the device. Figure 3.21 shows the x-ray diffraction pattern of ZnO and Ga doped ZnO nanocrystalline thin films. The diffraction peaks at 2θ (degrees) of 31.77° , 34.40° , 36.26° , 47.51° , 56.55° , 62.79° and 67.89° are indexed as (100), (002), (101), (102), (110), (103) and (112) planes of ZnO. All the diffraction peaks can be indexed to the hexagonal phase of ZnO with lattice constants $a = 3.248 \text{ \AA}$ and $c = 5.207 \text{ \AA}$, which are in good agreed with the reported standard values (JCPDS No.36-1451). It is observed that the diffraction peaks of the Ga doped ZnO show a small shift towards higher 2θ value when compared to that of ZnO. This shift may be due to occupation of Gallium ions at zinc sites. The lattice constants have been calculated and are $a = 3.245 \text{ \AA}$ and $c = 5.200 \text{ \AA}$. The diffraction pattern reveals that the Ga doped ZnO films also exhibits hexagonal wurtzite structure. It indicates the decrease of lattice constant, because the radius of Ga^{3+} ion (0.62 \AA) is smaller than that of Zn^{2+} ion (0.72 \AA). The decrease of lattice parameters could be caused by the increase of the number of substitutional Ga^{2+} ions into Zn^{2+} sites. Doping of Ga in ZnO does not lead to any structural phase transformation but introduces a lattice contraction. No characteristic diffraction peak corresponding to Ga compound impurity phase is observed, indicating that all gallium ions come into the crystal lattice of ZnO to substitute for zinc ions. In addition, the full width at half maximum of diffraction peaks increases with an increase of Ga doping level, which means that

the grain size decreases with the increase of Ga content. The grain size of ZnO and Ga doped ZnO are calculated using Scherrer's equation from equation 3.2. The grain size has been calculated and is found to be 22.3, 18.3, 13.0, 12.0, 11.2 and 10.7 nm for ZnO, 1.50, 3.60, 5.03, 7.12 and 9.08 at.% Ga doped ZnO respectively. It is observed that the grain size of the ZnO thin films decreased with increase Ga dopant concentration.

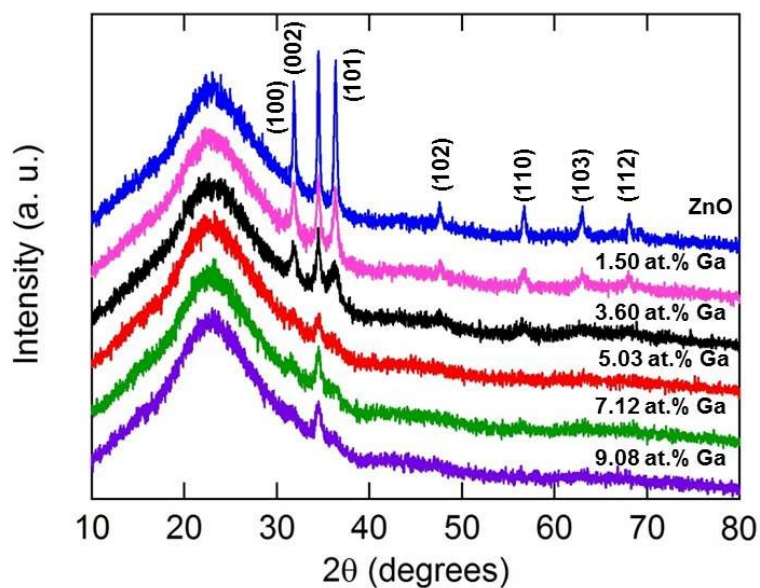


Figure 3.21 X-ray diffraction pattern of ZnO and Ga doped ZnO films

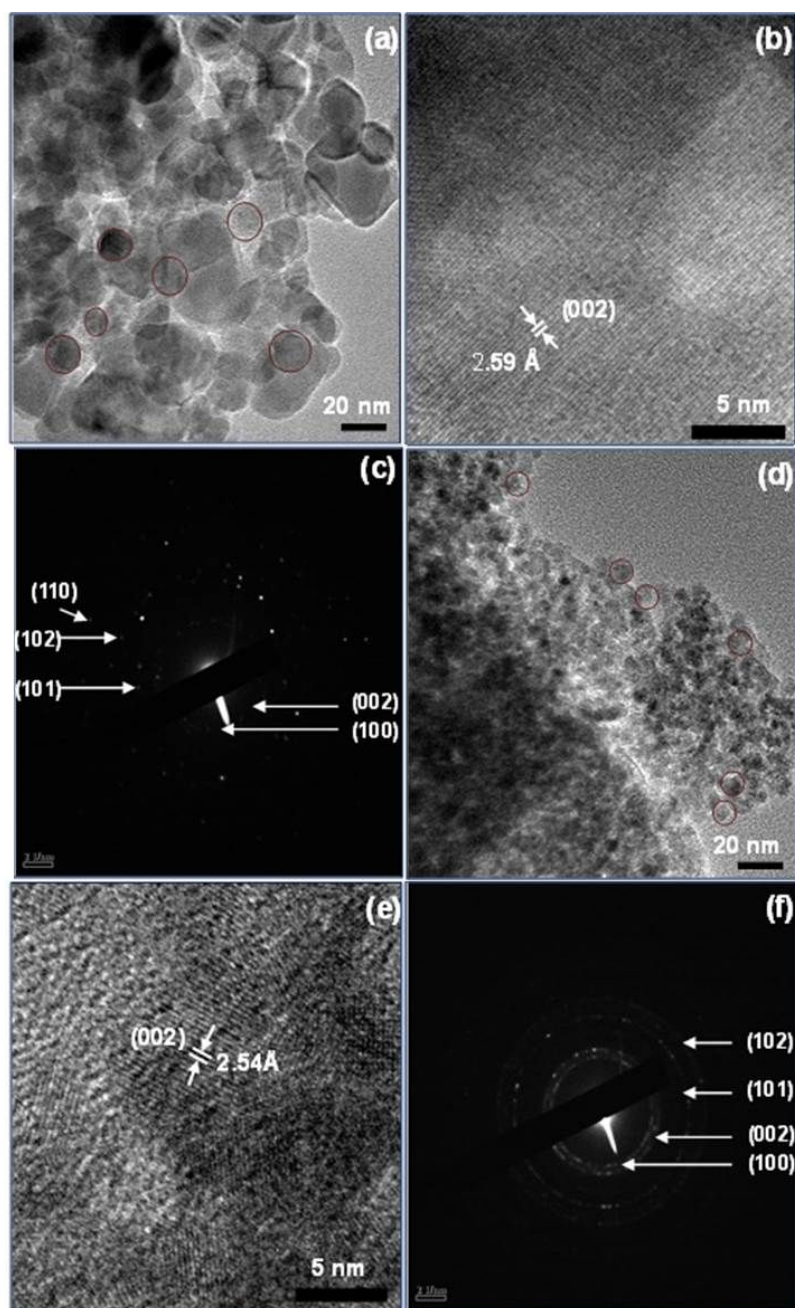


Figure 3.22 HRTEM, SAED images of (a, b, c) ZnO and (d, e, f) 5.03 at.% Ga doped ZnO

The size of the ZnO and Ga doped ZnO has been studied using high resolution transmission electron microscope (HRTEM). It can be seen from Figure 3.22 (a) and (d) that the grains are of nearly spherical shape with little agglomeration. The grain size of ZnO and 5.03 at.% Ga doped ZnO are found to be 22 and 12 nm. The Figure 3.22 (b) and (e) exhibit lattice fringes and the lattice spacing have been determined using these fringes. The HRTEM images of ZnO and 5.03 at.% Ga doped ZnO shows the lattice spacing of the (002) plane to be 2.59 Å for ZnO and 2.54 Å for 5.03 at.% Ga doped ZnO. The lattice spacing of 5.03 at.% Ga doped ZnO is slightly less than that of ZnO and this is because of the small ionic radius of Ga^{3+} when compared to that of Zn^{2+} ($r_{\text{Ga}^{3+}} = 0.62 \text{ Å}$, $r_{\text{Zn}^{2+}} = 0.72 \text{ Å}$). Selected area electron diffraction (SAED) was performed to identify the crystallite structure of ZnO. Figure 3.22 (c) and (f) shows the SAED pattern of ZnO and 5.03 at.% Ga doped ZnO films. The d spacing values calculated from these images are in close agreement with the values obtained from x-ray diffraction studies.

3.4 Inverted Polymer Solar Cells with Indium Gallium Zinc Oxide as an Electron Extraction Layer

It is well known that indium gallium zinc oxide (IGZO) has attracted much attention due to their wide bandgap, high electron mobility and carrier concentration, transparency in the thin film transistors (TFT) devices. IGZO has many issues such as deposition process, low temperature and ratio of indium, gallium and zinc element [85-86]. Especially, the relative ratio of indium, gallium and zinc is important in controlling the properties of the IGZO [87]. Indium acts as a free-electron supplier and improves the mobility, gallium suppresses the carrier generation via the formation of oxygen vacancies, and electrical conductivity is controlled by zinc atoms or oxygen vacancies [85,88]. Although IGZO have attracted much attention and outstanding properties in the TFT devices, none of the researcher is apply to organic solar cell. In this part, we have investigated the effect of zinc concentration on the performance of solution processed IGZO as an electron extraction layer for the inverted polymer solar cell based PTB7:PC₇₀BM and their thin films properties.

3.4.1 Structural and Morphological Properties of IGZO

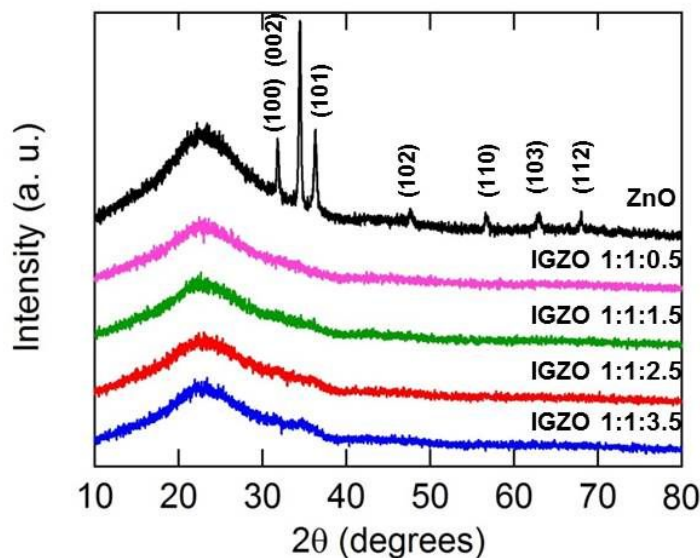


Figure 3.23 X-ray diffraction pattern of ZnO and IGZO films

Figure 3.23 shows x-ray diffraction (XRD) patterns of ZnO and IGZO thin films with different zinc concentration. The diffraction peaks at 2θ of 31.77° , 34.40° , 36.26° , 47.51° , 56.55° , 62.79° and 67.89° are indexed as (100), (002), (101), (102), (110), (103) and (112) planes corresponding to that of hexagonal wurtzite structure of ZnO. All the diffraction peaks could be indexed to the hexagonal phase of ZnO with lattice constants $a = 3.248 \text{ \AA}$ and $c = 5.207 \text{ \AA}$, which are in good agreement with the reported standard values (JCPDS No.36-1451). The grain size of ZnO has been calculated using Scherrer's equation (equation 3.2), which is found to be 22 nm. The x-ray diffraction profile (Figure 3.23) confirms the amorphous nature of the IGZO films. Figure 3.24 shows the field emission scanning electron microscope (FESEM) images of ZnO and IGZO thin films with different zinc concentration. In

IGZO thin films, the grains are small in size and are uniformly distributed throughout the surface

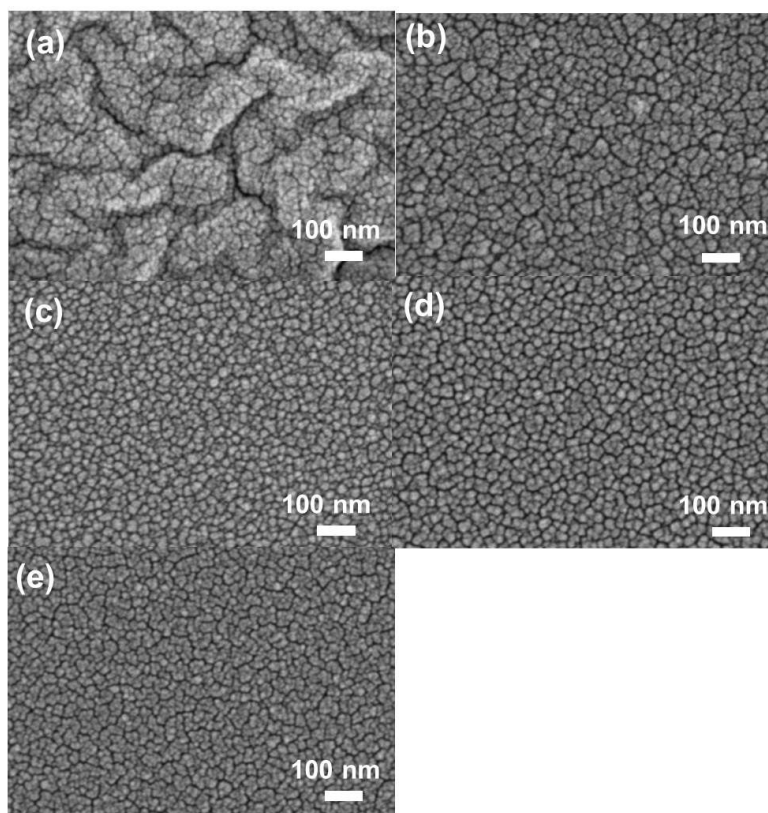


Figure 3.24 FESEM images of (a) ZnO and IGZO with the ratio of In:Ga:Zn (b) 1:1:0.5 (c) 1:1:1.5 (d) 1:1:2.5 (e) 1:1:3.5

Figure 3.25 shows the atomic force microscopy (AFM) images of ZnO and IGZO thin films with different zinc concentration. The root mean square (RMS) surface roughness was found to be 6.03, 2.18, 1.53, 1.48 and 1.61 nm for ZnO and for the different molar ratio of IGZO films (1:1:0.5, 1:1:1.5, 1:1:2.5 and 1:1:3.5) as shown in Figure 3.25 (f). It reveals that the IGZO films are much smoother surface than that of the ZnO film. These results indicate that much smoother surface

contribute to more uniform interfacial contact between IGZO and PTB7:PC₇₀BM layer, which could improve the electron extraction properties.

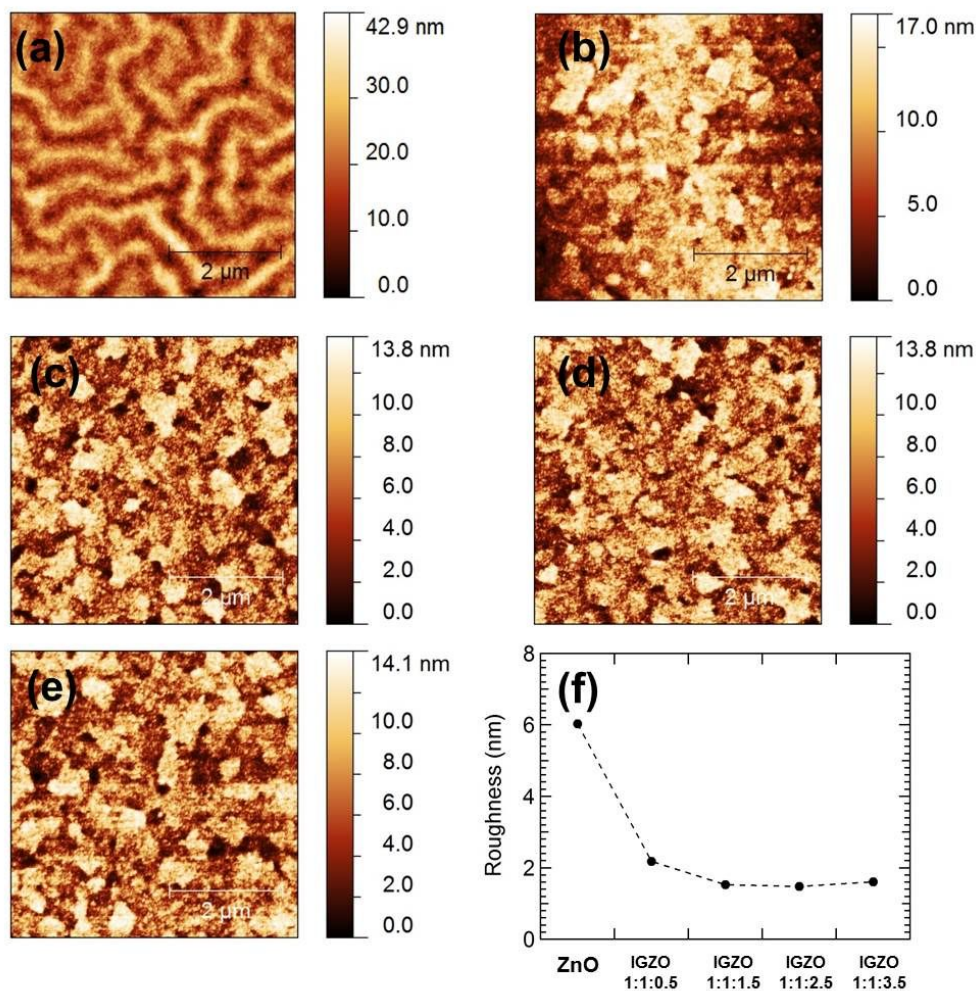


Figure 3.25 AFM images of (a) ZnO and IGZO with the ratio of In:Ga:Zn (b) 1:1:0.5 (c) 1:1:1.5 (d) 1:1:2.5 (e) 1:1:3.5 (f) the root mean square (RMS) surface roughness of ZnO and IGZO

3.4.2 Electrical Properties of IGZO

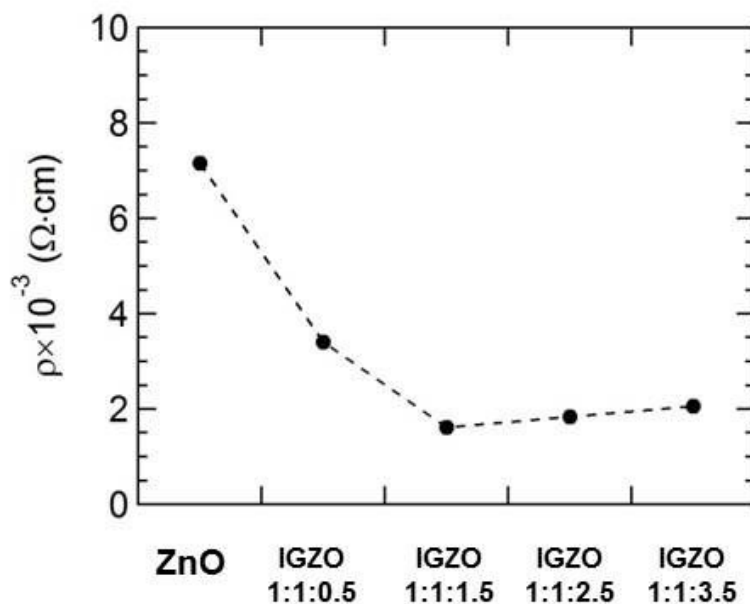


Figure 3.26 Variation of resistivity of ZnO and IGZO films with different Zn concentration

It is well known that the electrical properties of the interfacial layers are very important for the performance of the devices because they will affect charge extraction at the interface. Figure 3.26 shows the variation of resistivity of IGZO films with different zinc concentration. The electrical resistivity is found to be $7.16 \times 10^{-3} \Omega \cdot \text{cm}$, $3.41 \times 10^{-3} \Omega \cdot \text{cm}$, $1.62 \times 10^{-3} \Omega \cdot \text{cm}$, $1.84 \times 10^{-3} \Omega \cdot \text{cm}$ and $2.06 \times 10^{-3} \Omega \cdot \text{cm}$ for ZnO, 1:1:0.5, 1:1:1.5, 1:1:2.5 and 1:1:3.5 molar ratio of IGZO films respectively. It is observed that the resistivity of IGZO is much lower than that of the ZnO.

3.4.3 Optical Properties of IGZO

The work function of ZnO and IGZO films (-7.44 eV and -7.40 eV respectively) were measured using the ultraviolet photoelectron spectroscopy (UPS) shown in Figure 3.27 (a). The optical band gap (E_g) was obtained from the UV absorption spectra and are as shown in Figure 3.27 (b). It is found that the absorption spectra of the IGZO thin film exhibit a blue shift when compared to that of the ZnO thin film. In general the blue shift of the absorption onset of the IGZO is associated with the increase in the carrier concentration blocking the lowest states in the conduction band, well known as the Burstein-Moss effect.

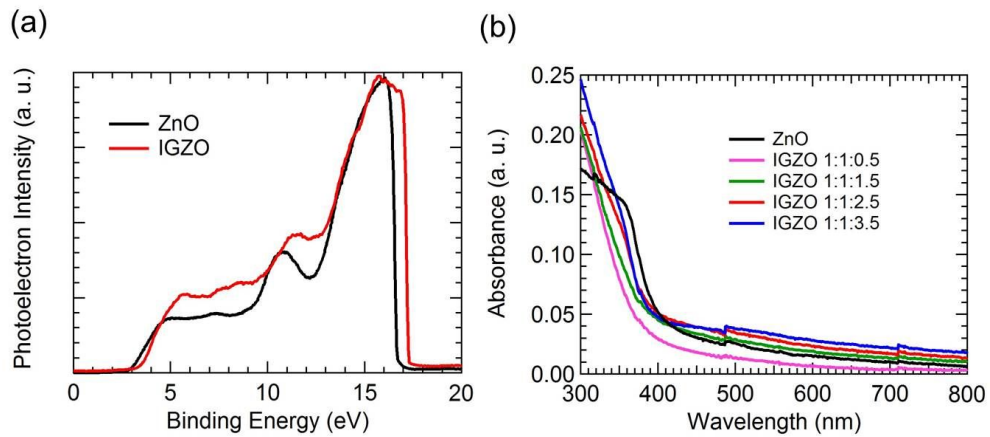


Figure 3.27 (a) UPS spectra and (b) absorption spectra of ZnO and IGZO with different Zn concentration

In order to investigate the composition of ZnO and IGZO films, the x-ray photoelectron spectroscopy (XPS) measurements were carried out. Figure 3.28 shows the XPS spectra of ZnO and IGZO films. The binding energies of IGZO are 528.61 eV, 1019.49 eV and 1042.54 eV for O $1s$, Zn $2p_{3/2}$ and Zn $2p_{1/2}$ respectively.

These binding energies are shifted towards the higher binding energy compared to ZnO (528.02 eV, 1019.29 eV and 1042.18 eV for O $1s$, Zn $2p_{3/2}$ and Zn $2p_{1/2}$ respectively). This result indicates that indium and gallium are incorporated into the ZnO. Figure 3.28 (c) and (d) show the peaks at 442.52 eV, 449.96 eV and 1115.79 eV corresponding to the In $3d_{5/2}$, In $3d_{3/2}$ and Ga $2p_{3/2}$ respectively.

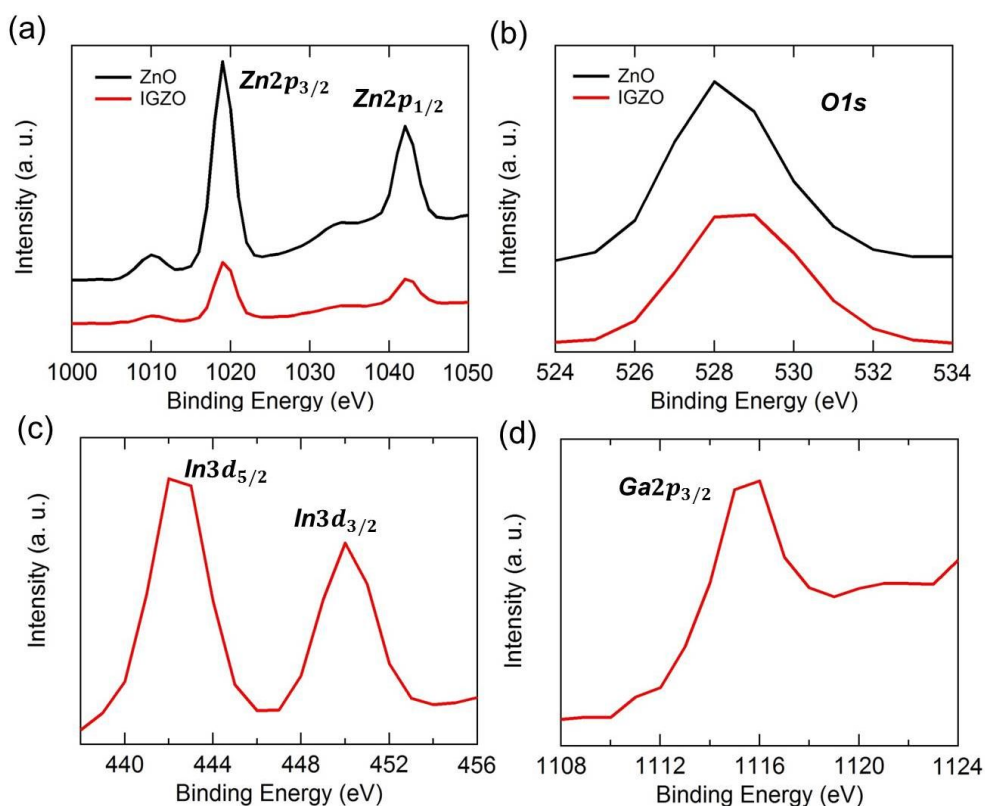


Figure 3.28 XPS spectra of ZnO and IGZO films (a) Zn $2p$ (b) O $1s$ (c) In $3d$ (d) Ga $2p$

3.4.4 Device Characteristics with IGZO

The polymer solar cell consists of ITO / ZnO or IGZO / PTB7:PC₇₀BM / MoO₃ / Al shown in Figure 3.29. When light illuminates the solar cell through ITO electrode, the incident light is absorbed by the PTB7:PC₇₀BM photoactive layer and the generated excitons will diffuse and dissociate at the PTB7:PC₇₀BM interface. Then the generated electrons and holes move easily towards ZnO or IGZO and MoO₃ layer because the LUMO of ZnO and IGZO and the HOMO of MoO₃ are close to the LUMO of PC₇₀BM and HOMO of PTB7 respectively. Moreover as the HOMO level of ZnO and IGZO is much lower than that of PTB7 and LUMO level of MoO₃ is much higher than that of PC₇₀BM, it blocks the hole transport from PTB7 to the ITO electrode and electron transport from PC₇₀BM to the Al electrode.

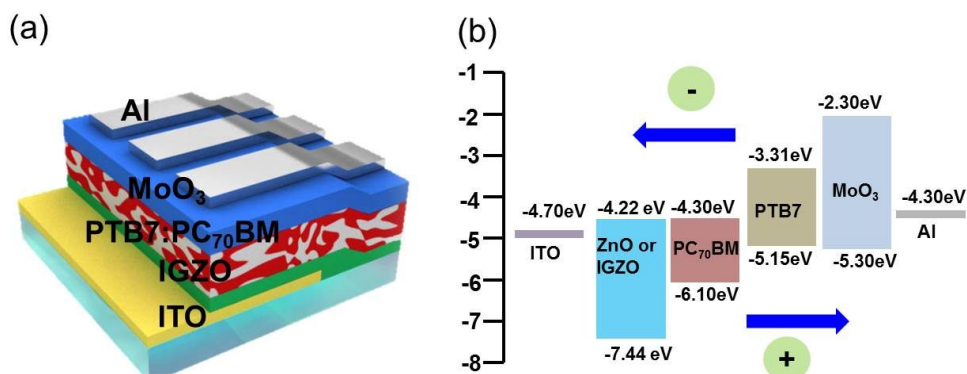


Figure 3.29 (a) Device structure and (b) energy level diagrams of inverted polymer solar cells with IGZO as an electron extraction layer.

Figure 3.30 shows the current density-voltage (J-V) characteristics of inverted polymer solar cells fabricated using ZnO and IGZO with different zinc concentration. This has been measured under 100 mW/cm² AM 1.5G light

illumination. The solar cell parameters short circuit current density (J_{SC}), open circuit voltage (V_{OC}), fill factor (FF), power conversion efficiency (PCE), series resistance (R_s) and shunt resistance (R_{sh}) are summarized in Table 3.4. As can be seen, the reference device using ZnO as an electron extraction layer shows a J_{SC} of 14.83 mA/cm^2 , V_{OC} of 0.75 V , FF of 56.12% and PCE of 6.22% . It is observed that the inverted PTB7:PC₇₀BM device performance with IGZO as an electron extraction layer was found to be better as compared to ZnO based device. Especially, inverted polymer solar cell fabricated with IGZO (molar ratio of 1:1:2.5) exhibited the best photovoltaic performance among all the devices, with a J_{SC} of 17.47 mA/cm^2 , V_{OC} of 0.76 V , FF of 65.36% and PCE of 8.72% . When the IGZO ratio was increased up to 1:1:3.5, the device showed a reduced J_{SC} of 17.34 mA/cm^2 and a reduced FF of 61.53% , giving a final PCE of 8.11% . From the J-V curve, we can extract the series resistance (R_s) and shunt resistance (R_{sh}). The reference device fabricated using ZnO shows a R_s of $14.15 \Omega \cdot \text{cm}^2$ and R_{sh} of $284.96 \Omega \cdot \text{cm}^2$. The IGZO (1:1:2.5) device showed the smallest R_s of $1.92 \Omega \cdot \text{cm}^2$ and highest R_{sh} of $1411.35 \Omega \cdot \text{cm}^2$. The decrease in R_s and increase in R_{sh} indicate that the electron extraction is favorable and there is a decrease in leakage current and there are responsible for the enhanced J_{SC} and FF. As a result, the dark J-V characteristics (Figure 3.31 (a)) shows that the IGZO device exhibited excellent diode characteristics and lower leakage current under reverse bias as compared to the device based on the ZnO. The incident photon to charge carrier efficiency (IPCE) spectra are shown in (Figure 3.31 (b)) clearly indicates that the overall IPCE of the device fabricated using IGZO is higher than that of the device constructed using ZnO. The J_{SC} values have been calculated by IPCE data with an AM 1.5G reference spectrum. The J_{SC} is found to be 14.62 , 15.69 , 17.29 , 17.35 and 16.76 mA/cm^2 for ZnO, 1:1:0.5, 1:1:1.5, 1:1:2.5 and 1:1:3.5 molar

ratio of IGZO based solar cells respectively. These values match well with obtained J_{SC} from J-V measurement (Table 3.4).

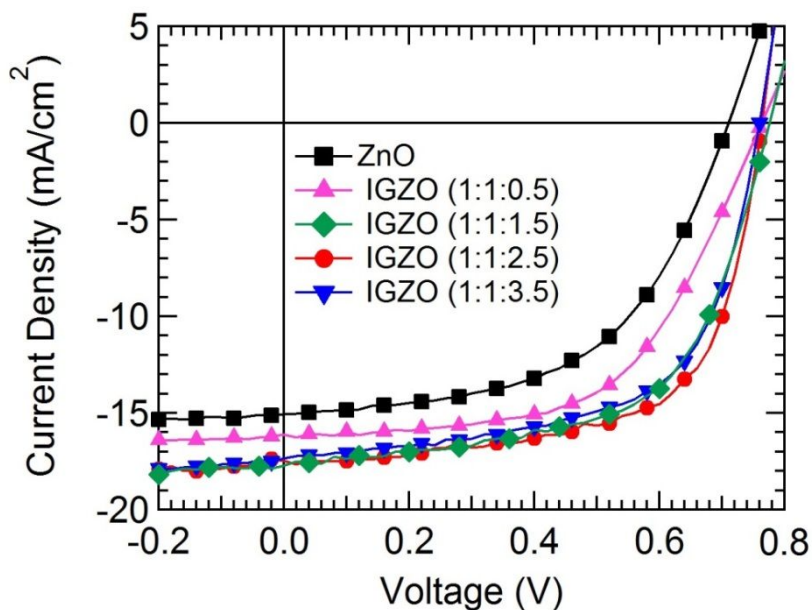


Figure 3.30 J-V characteristics of inverted polymer solar cell using ZnO and IGZO with different Zn concentration

Table 3.4 Device performance of inverted polymer solar cells using ZnO and IGZO with different Zn concentration.

	ZnO	IGZO			
		1:1:0.5	1:1:1.5	1:1:2.5	1:1:3.5
J_{SC} (mA/cm ²)	15.06	16.12	17.71	17.47	14.34
V_{OC} (V)	0.71	0.76	0.77	0.76	0.76
FF (%)	53.95	57.22	59.93	65.36	61.53
PCE (%)	5.77	7.04	8.23	8.72	8.11
R_s ($\Omega \cdot \text{cm}^2$)	14.15	11.41	5.04	1.92	2.90
R_{sh} ($\Omega \cdot \text{cm}^2$)	284.96	836.37	1108.41	1851.35	1390.75

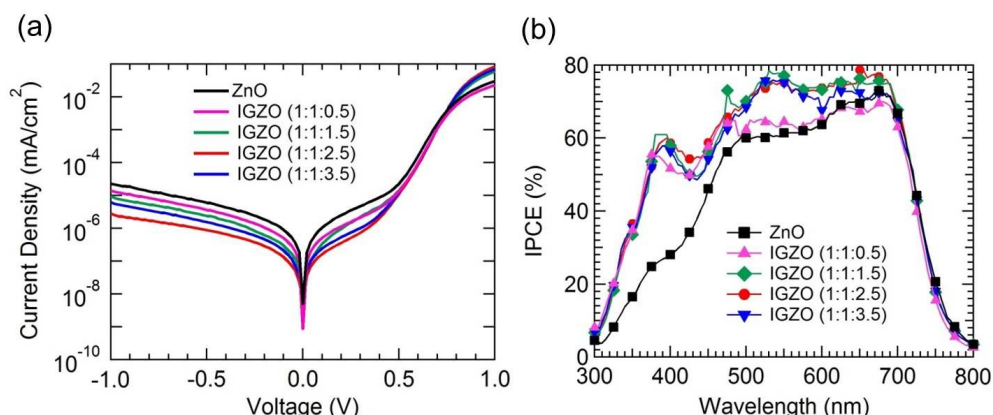


Figure 3.31 (a) Dark J-V characteristics and (b) IPCE spectra of inverted polymer solar cells using ZnO and IGZO with different Zn concentration

3.4.5 Light Intensity Dependence of Device Performance with IGZO

In order to study the influence of IGZO for inverted polymer solar cell performance, we carried out light intensity dependent J-V measurements ($1 \sim 100 \text{ mW/cm}^2$) at room temperature (293 K) and analyzed the device characteristics. Figure 3.32 exhibits incident light intensity dependence of inverted polymer solar cells. The J_{SC} and V_{OC} exhibit linearly increase with light intensity. From Figure 3.32 (a), we can extract recombination coefficient (α) that are 0.813, 0.851, 0.870, 0.907 and 0.875 for ZnO, IGZO (1:1:0.5), IGZO (1:1:1.5), IGZO (1:1:2.5) and IGZO (1:1:3.5). This result indicates that the bimolecular recombination process is less in the device with the IGZO as an electron extraction layer. Overall device performance (J_{SC} , V_{OC} , FF and PCE) using IGZO 1:1:2.5 is better than that of the device with ZnO.

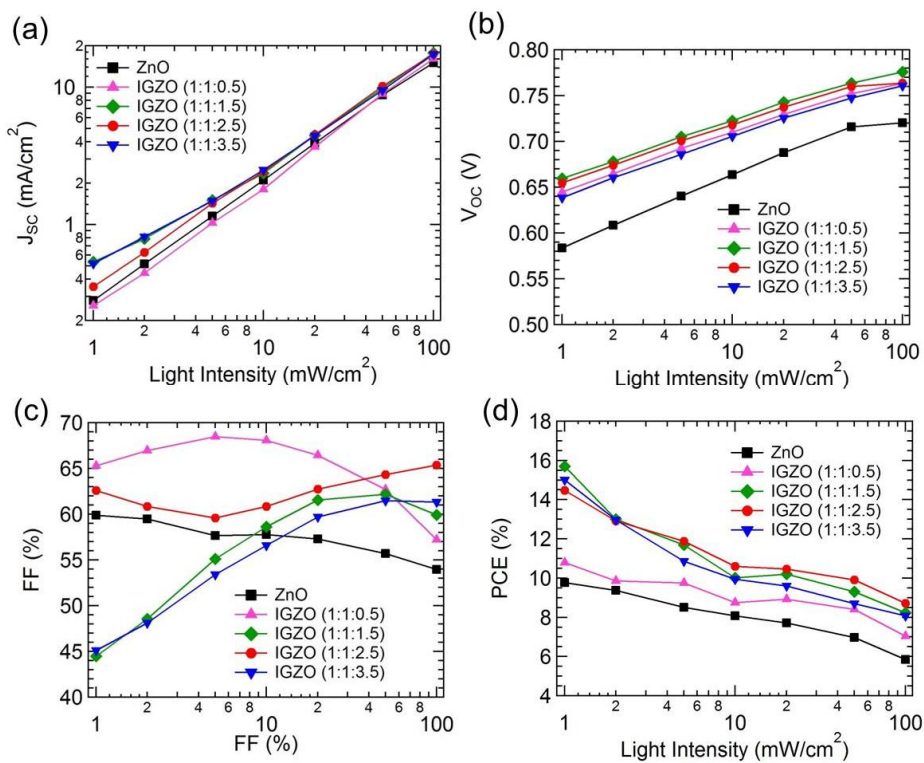


Figure 3.32 Incident light intensity dependence of (a) J_{sc} (b) V_{oc} (c) FF and (d) PCE of inverted polymer solar cells using ZnO and IGZO with different Zn concentration.

3.5 Inverted Polymer Solar Cells with Metal-Doping Dependent ZnO as an Electron Extraction Layer

In the chapter 3.1 ~ 3.4, the electrical, optical, structural and morphological properties of In, Al, Ga doped ZnO and IGZO are much better than pristine ZnO. Although metal doping has greatly effect of electron extraction properties, we need to verify which dopant is more efficient as an electron extraction layer in the devices. In this part, we have investigated the effect of metal doping dependent ZnO as an electron extraction layer in the inverted polymer solar cell based on PTB7:PC₇₀BM and PTB7-Th:PC₇₀BM.

3.5.1 Device Characteristics with Metal-Doping Dependent ZnO

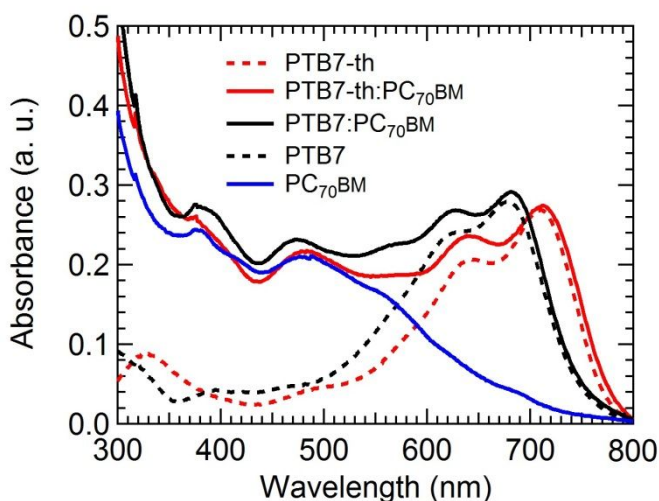


Figure 3.33 Absorption spectra of PTB7-Th, PTB7-Th:PC₇₀BM, PTB7, PTB7:PC₇₀BM and PC₇₀BM

As shown in Figure 3.33, the absorption range of PTB7 and PTB7-Th are 500 to 745 nm and 500 to 785 nm. In other words, the absorption spectra of PTB7-Th:PC₇₀BM is longer than PTB7:PC₇₀BM. This result indicates that incident lights are more absorbed in PTB7-Th:PC₇₀BM than PTB7:PC₇₀BM. In the experiment data as shown in Figure 3.34 (a) to (d) and Table 3.5 and Table 3.6, the overall J_{SC} and IPCE spectra of the PTB7-Th:PC₇₀BM based devices are much better than those of PTB7:PC₇₀BM based devices. Moreover, the HOMO level of PTB7-Th (5.22 eV) is higher than PTB7 (5.15 eV). So the V_{OC} of PTB7-Th:PC₇₀BM based devices are much higher than that of PTB7:PC₇₀BM based devices.

Figure 3.34 shows the J-V characteristics and IPCE spectra of inverted polymer solar cells with the structure of ITO / electron extraction layer / PTB7:PC₇₀BM or PTB7-Th:PC₇₀BM / MoO₃ / Al. The solar cell parameters are summarized in Table 3.5 and Table 3.6. In others, the overall device performance of In, Al, Ga doped ZnO (one element doping) and IGZO (two element doping) was found to be better as compared to pristine ZnO due to improvement of optical, structural and morphological properties as well as electron extraction property as mentioned above. Especially, the best device performance is with IGZO electron extraction layer. The PTB7:PC₇₀BM based devices show photovoltaic performance with a J_{SC} of 17.48 mA/cm², V_{OC} of 0.76 V, FF of 65.25% and PCE of 8.71 % and PTB7-Th:PC₇₀BM based devices show photovoltaic performance with a J_{SC} of 18.99 mA/cm², V_{OC} of 0.81 V, FF of 62.09% and PCE of 9.60 %. In case we compared to one element doping (In, Al and Ga doped ZnO), the power conversion efficiencies are almost similar (PCE of PTB7:PC₇₀BM = 7.51 ~ 7.86 %, PCE of PTB7-Th:PC₇₀BM = 8.53 ~ 8.72 %). But individual solar cell parameters are little different. Especially, higher J_{SC} values are In doped ZnO (16.56 mA/cm²), Al doped ZnO (16.15 mA/cm²) and Ga doped ZnO (15.83 mA/cm²) based devices in the order named. On the other hand,

higher FF values are Ga doped ZnO (64.79 %), Al doped ZnO (62.23 %) and In doped ZnO (59.75 %) in the order named. J_{SC} is related the electrical properties such as electron mobility and conductivity of electron extraction layer. As mentioned above in the chapter 3.1 ~ 3.3, the electron mobility and conductivity of In doped ZnO are better than those of other doped ZnO. In this reason, the J_{SC} of In doped ZnO is more higher. The FF is related to the impedance, recombination process and activation energy, which we explained below.

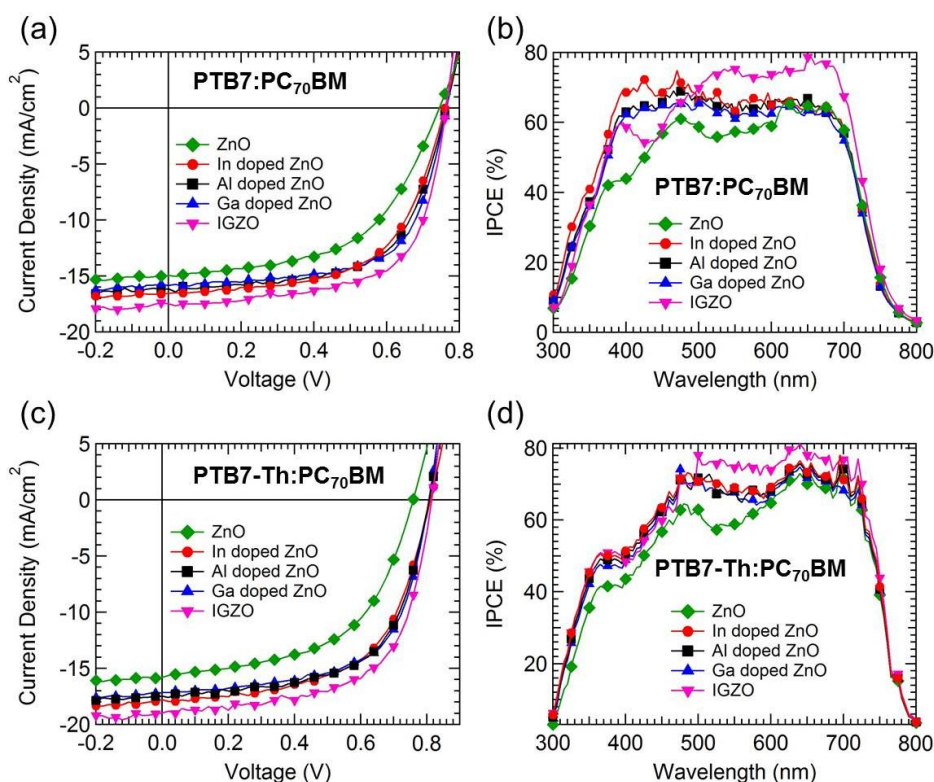


Figure 3.34 Device characteristics of inverted polymer solar cells with different electron extraction layers (a) J-V characteristics, (b) IPCE spectra based on PTB7:PC₇₀BM and (c) J-V characteristics, (d) IPCE spectra based on PTB7-Th:PC₇₀BM

Table 3.5 Summary of the performance parameters of PTB7:PC₇₀BM based inverted polymer solar cells with different electron extraction layers.

	ZnO	In doped ZnO	Al doped ZnO	Ga doped ZnO	IGZO
J _{SC} (mA/cm ²)	14.92	16.56	16.15	15.83	17.48
V _{OC} (V)	0.74	0.76	0.76	0.76	0.76
FF (%)	54.26	59.75	62.23	64.97	65.25
PCE (%)	6.03	7.51	7.67	7.86	8.71
R _s (Ω·cm ²)	15.93	5.97	5.60	5.44	2.69
R _{sh} (Ω·cm ²)	519.34	1533.62	1631.64	1755.01	1819.23

Table 3.6 Summary of the performance parameters of PTB7-Th:PC₇₀BM based inverted polymer solar cells with different electron extraction layers

	ZnO	In doped ZnO	Al doped ZnO	Ga doped ZnO	IGZO
J _{SC} (mA/cm ²)	16.34	17.78	17.48	17.16	18.99
V _{OC} (V)	0.76	0.81	0.81	0.81	0.81
FF (%)	52.89	59.18	61.67	62.07	62.39
PCE (%)	6.56	8.53	8.67	8.72	9.60
R _s (Ω·cm ²)	16.69	5.98	5.72	5.68	4.36
R _{sh} (Ω·cm ²)	496.60	1501.47	1583.48	1603.07	1686.49

3.5.2 Impedance Characteristics with Metal-Doping Dependent ZnO

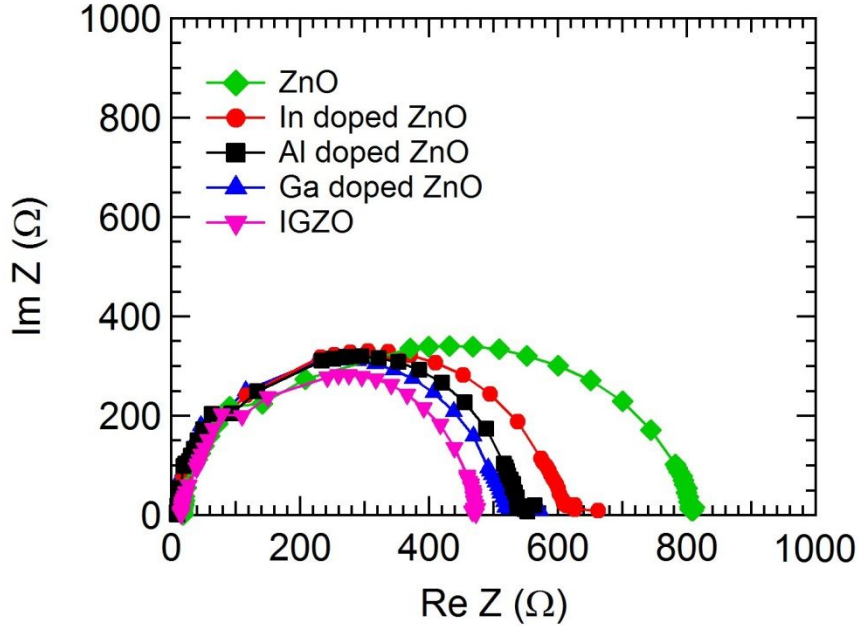


Figure 3.35 Impedance spectra of the inverted polymer solar cell with different electron extraction layer

Figure 3.35 shows a Cole-Cole plot, $\text{Im}(Z)$ vs $\text{Re}(Z)$, of each device under AM1.5G solar radiation at 100 mW/cm^2 . The impedance of the devices can be modeled as a combination of resistance and capacitance values [89-90].

$$Z = Z' + Z'' = R_C + \frac{R_p}{1 + \omega^2 R_p^2 C_p^2} + \frac{\omega^2 R_p^2 C_p}{1 + \omega^2 R_p^2 C_p^2} \quad (3.5)$$

$$Z' = R_C + \frac{R_p}{1 + \omega^2 R_p^2 C_p^2}, Z'' = \frac{\omega^2 R_p^2 C_p}{1 + \omega^2 R_p^2 C_p^2} \quad (3.6)$$

Where, R_C is contact resistance and R_p is junction resistance. The contact resistance (R_C) is almost same for all devices ($2 \sim 5 \Omega$), because R_C is related to ITO contact properties. On the other hand, R_p is different depending on with and without doping. As shown in Figure 3.35, R_p using In doped ZnO, Al doped ZnO, Ga doped ZnO and IGZO are 620.6, 550.3, 520.9 and 480.1 Ω which are lower by 25 ~ 35 % than $R_p = 800.3 \Omega$ for the device with pristine ZnO. This result indicates that the doped ZnO and IGZO can enhance the electron extraction property in the inverted polymer solar cells.

3.5.3 Temperature and Light Intensity Characteristics with Metal-Doping Dependent ZnO

The charge carriers in the organic solar cells under investigation are efficiently photo generated via ultrafast electron transfer between donor and acceptor materials. The fate of the photo generated electrons and holes are crucial for the device performance, therefore, the influence of light intensity on the J-V characteristics is important [91]. In order to examine the influence of doping effect of ZnO for inverted polymer solar cell performance, we carried out temperature (T) dependent J-V measurements (100 ~ 350 K) at different light power (P_{Light} , 1 ~ 100 mW/cm²) and analyzed the device characteristics. Figure 3.36 exhibits incident light intensity (P_{Light}) dependence of inverted polymer solar cells with different electron extraction layers at room temperature (293 K). The J_{SC} and V_{OC} exhibit linearly increase with light intensity. Figure 3.37 shows the light intensity dependence of J_{SC} at various temperature (100 ~ 350 K) in a log-log plot. The J_{SC} follows a power law dependence.

$$J_{SC} = P_{Light}^{\alpha} \quad (3.8)$$

where α is the exponent, which is correlated to the recombination processes in organic solar cells. According to literature, the scaling exponent can be related to either the ratio of monomolecular to bimolecular recombination [92] or the relative imbalance between electron and hole mobility of the acceptor and donor materials [93]. Since the donor and acceptor materials of all the devices are same, the scaling exponent is strongly related to recombination processes.

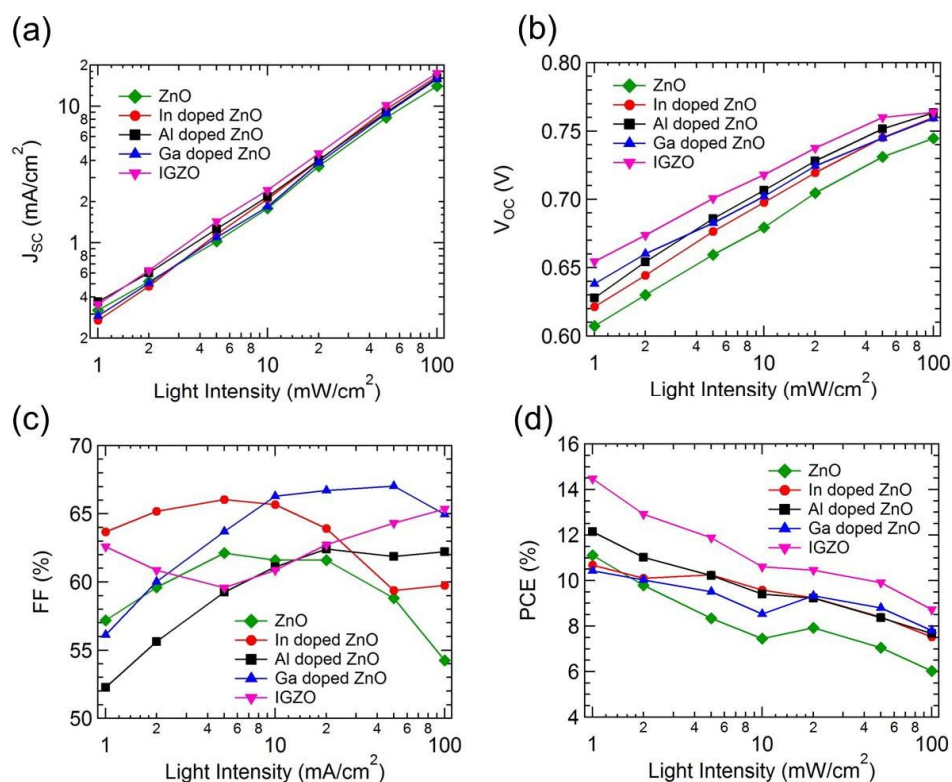


Figure 3.36 Incident light intensity dependence of (a) J_{SC} (b) V_{OC} (c) FF (d) PCE of inverted polymer solar cells with different electron extraction layers at room temperature

It is known that the linear dependence ($\alpha = 1$) of the J_{SC} on P_{Light} indicates ideal monomolecular recombination process via defects, while bimolecular recombination process of electrons and holes, reflected by a square-root photocurrent light intensity dependence ($\alpha = 0.5$). In the case of the inverted polymer solar cell with the different electron extraction layers, α are 0.845 - 0.886 for In doped ZnO, 0.873 ~ 0.881 for Al doped ZnO, 0.866 ~ 0.897 for Ga doped ZnO and 0.861 ~ 0.900 for IGZO in the temperature range of 100 ~ 350 K. However in case of the device using ZnO, α is 0.767 ~ 0.857 in the temperature range of 100 ~ 350 K. This result indicates that the bimolecular recombination process is less in the device with the In, Al, Ga doped ZnO and especially IGZO electron extraction layer. Therefore, the insertion of the doped ZnO and IGZO layer reduces the bimolecular recombination loss owing to enhanced carrier extraction efficiency, resulting in enhanced device performance [91-92].

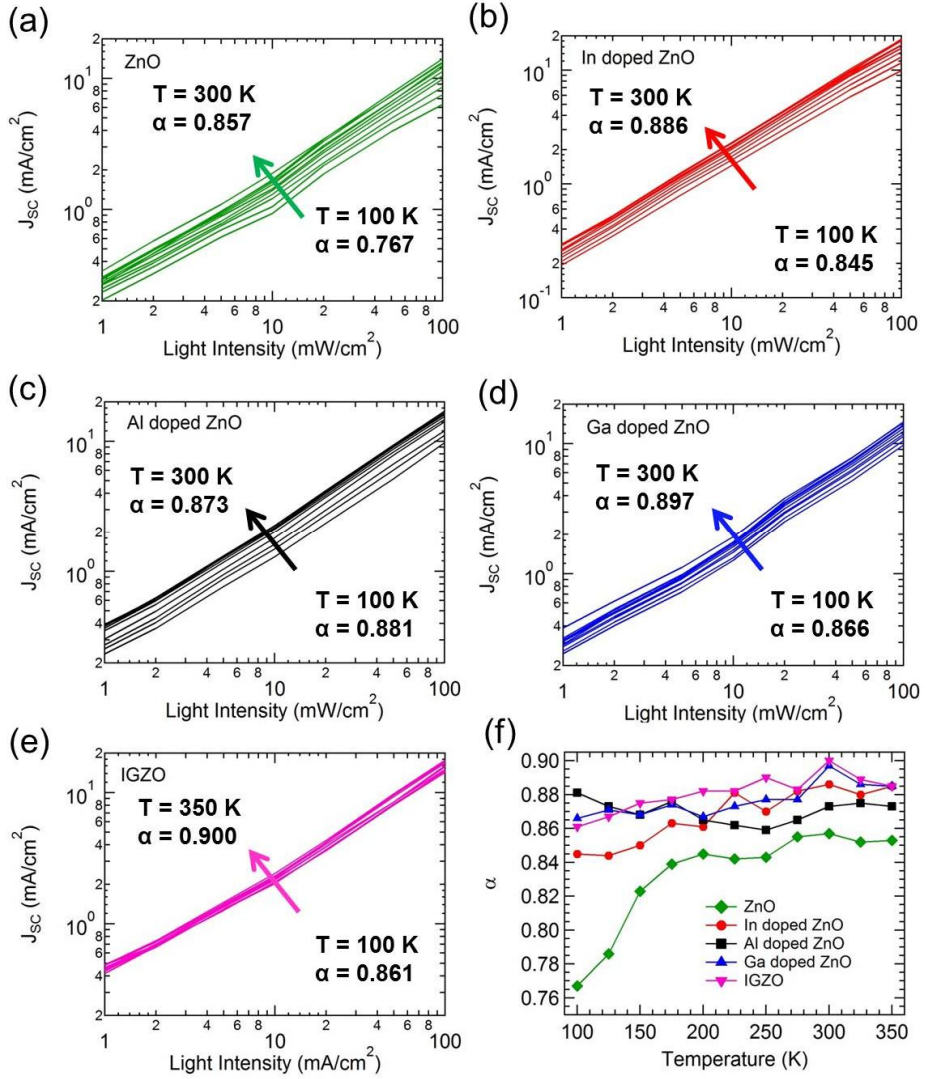


Figure 3.37 J_{sc} as a function of light intensity ($1 \sim 100$ mW/cm²) for various temperatures (100 ~ 350 K) for inverted polymer solar cells (a) ZnO (b) In doped ZnO (c) Al doped ZnO (d) Ga doped ZnO (e) IGZO and (f) Recombination coefficient obtained in the temperature range of 100~ 350 K

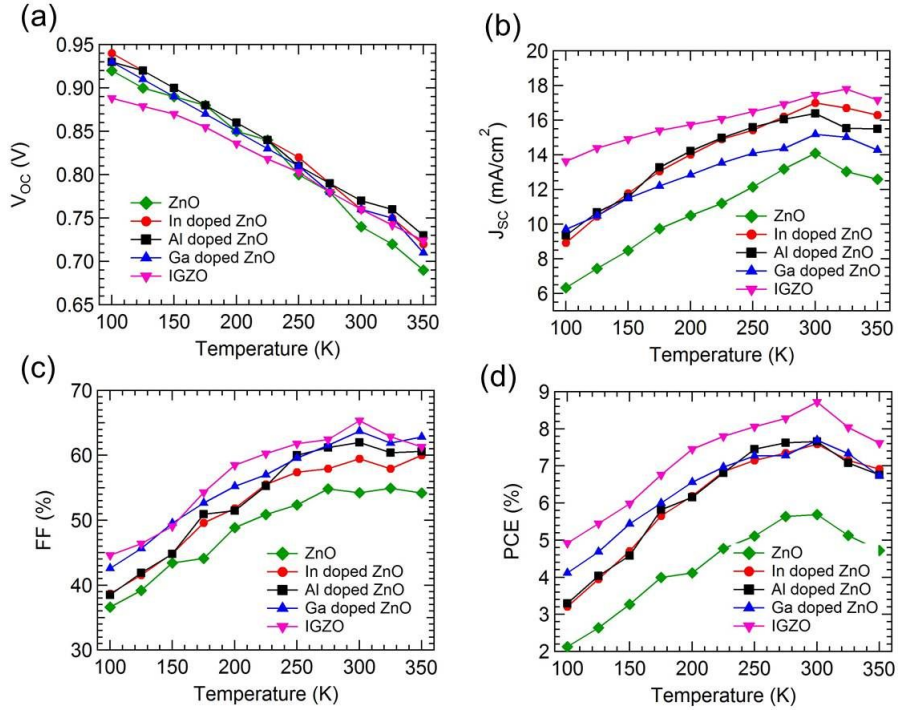


Figure 3.38 Temperature dependence of (a) V_{OC} (b) J_{SC} (c) FF (d) PCE of inverted polymer solar cell with different electron extraction layer

Figure 3.38 shows the V_{OC} , J_{SC} , FF and PCE in the temperature range from 100 to 350 K for the inverted polymer solar cell with different electron extraction layer. The overall device performance adopting a In, Al, Ga doped ZnO and IGZO electron extraction layer is higher than that of the device using ZnO layer. The V_{OC} of all devices decreases linearly with increasing temperature, as shown in Figure 3.38 (a). This result is consistent with the well-known equation 3.9 for a p-n junction solar cell [94].

$$V_{OC} = \frac{E_g}{e} - \frac{k_B T}{e} \ln \frac{I_{0,max}}{I_{SC}} \quad (3.9)$$

where E_g is the energy band gap of the materials, I_{SC} is the short-circuit current, $I_{0,max}$ is the maximum saturation current, k_B is the Boltzmann constant, T is the absolute temperature, and e is the electronic charge. This behavior is also consistent with a simulation result reported previously [95]. The V_{OC} is not very different between all devices; the device with In, Al and Ga doped ZnO shows about a 0.01-0.04 V higher V_{OC} than that using ZnO. However, the device with In, Al, Ga doped ZnO and IGZO shows an enhanced J_{SC} and FF for the entire temperature range compared with that with ZnO, as shown in Figure 3.38 (b) and (c). The enhanced J_{SC} and FF are attributed to the ease of carrier extraction by using doping. Meanwhile, both J_{SC} and FF increase with increasing temperature regardless of the existence of the doping. It is well known that the mobility of organic semiconductors increases when the temperature increases since the hopping probability of carriers and thermal release from trap states increase. As a result, the PCE of the device with In, Al, Ga doped ZnO and IGZO is higher than that with ZnO for the entire temperature range as shown in Figure 3.38 (d).

Figure 3.39 shows the current density continually increases with temperature. This temperature dependence of the short circuit current is a result of either temperature dependent mobility or a result to overcoming shallow trap states. However, as described above, we attribute the light intensity scaling exponent to primarily monomolecular recombination rather than electron and hole mobility imbalance, the temperature dependence is likely a result of overcoming shallow trap states, rather than temperature dependent mobility. Using equation 3.10 we can model the temperature dependence of the short circuit current, where P_{Light} is the light intensity, k_B is the Boltzman constant, T is the temperature, and Δ is the energetic depth of the trap state or activation energy [91].

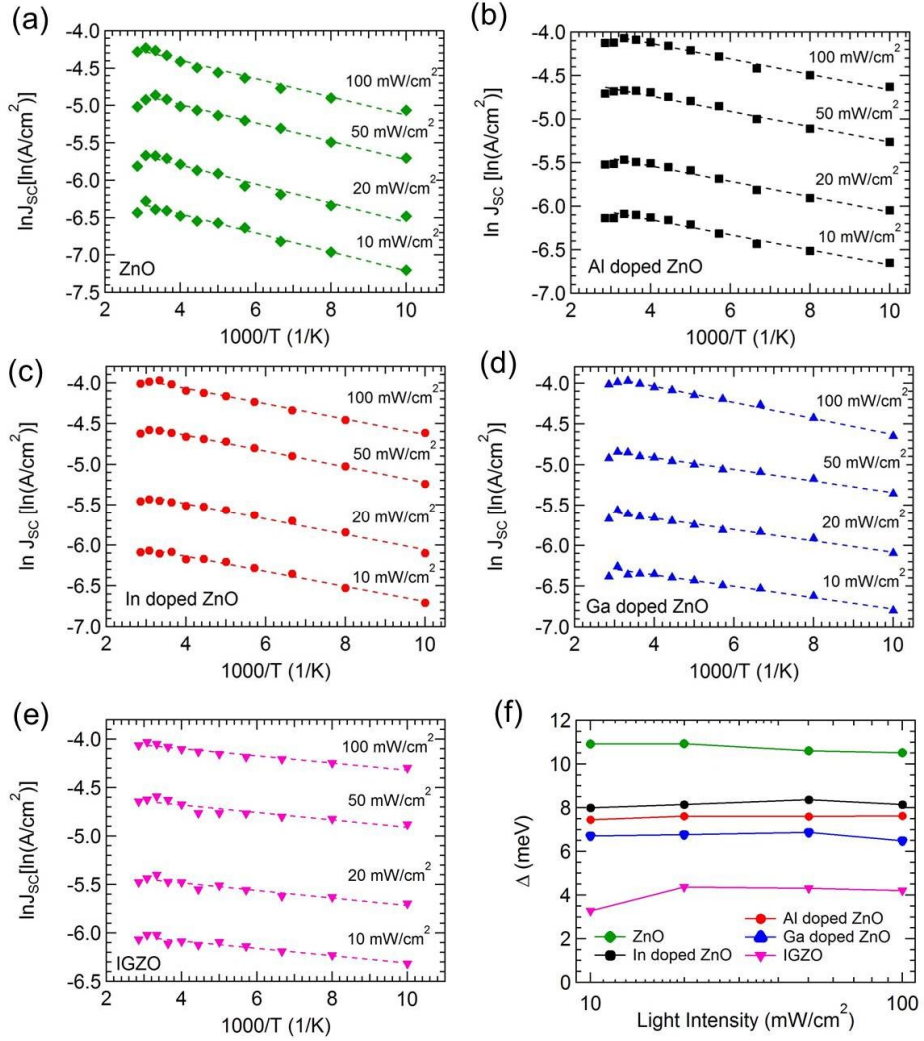


Figure 3.39 Arrhenius plot of J_{SC} against T for the inverted polymer solar cells with different electron extraction layer (a) ZnO (b) In doped ZnO (c) Al doped ZnO (d) Ga doped ZnO (e) IGZO and (f) activation energy extracted from the data shown in (a) to (e).

$$J_{SC}(T, P_{Light}) = J_0(P_{Light}) \cdot \exp\left(-\frac{\Delta}{k_B T}\right) \quad (3.10)$$

Plotting $\ln(J_{SC})$ vs. $1000/T$ and taking the slope gives the activation energy, or energy required to escape the traps (Figure 3.39). The activation energy is related to

the height of the potential barrier; thus, carrier transport is more difficult in a device with a larger activation energy. The activation energy of the device using doped ZnO (8.00 ~ 8.35 meV, 7.45 ~ 7.62 meV, 6.48 ~ 6.87 meV and 3.27 ~ 4.30 meV for In doped ZnO, Al doped ZnO, Ga doped ZnO and IGZO) is lower than that of the device with ZnO (10.52 ~ 10.92 meV) in the whole illumination intensity range, as depicted in Figure 3.39 (f). This result indicates that the carrier transport and extraction are enhanced in the device with In, Al, Ga doped ZnO and especially IGZO, consistent with the enhanced J_{sc} and FF for the device with In, Al, Ga doped ZnO and IGZO shown in Figure 3.38.

A more detailed analysis of the recombination mechanisms in bulk heterojunction solar cells is necessary to understand the physical meaning. Recently, C. Voz *et al.* calculated the collection voltage from J-V characteristic at different incident light illumination. From collection voltage value, they can extract the carrier collection length (l_{c0}), which is the maximum distance that the hole and electron of dissociated excitons can separate apart driven by the electric field before recombination, carrier collection efficiency (η_{c0}) as well as $\mu\tau_{eff}$ of organic solar cells [96].

$$V_c = \left(\frac{l_{c0}}{L/2} - 1 \right) V_{bi} \quad (3.11)$$

$$\eta_{c0} = 1 - \frac{L/2}{l_{c0}} \quad (3.12)$$

$$\mu\tau_{eff} = l_{c0} \frac{L}{V_{bi}} = \frac{L^2}{2V_{bi}} \left(\frac{V_c}{V_{bi}} + 1 \right) \quad (3.13)$$

where V_{bi} is built-in potential, L is thickness of active layer

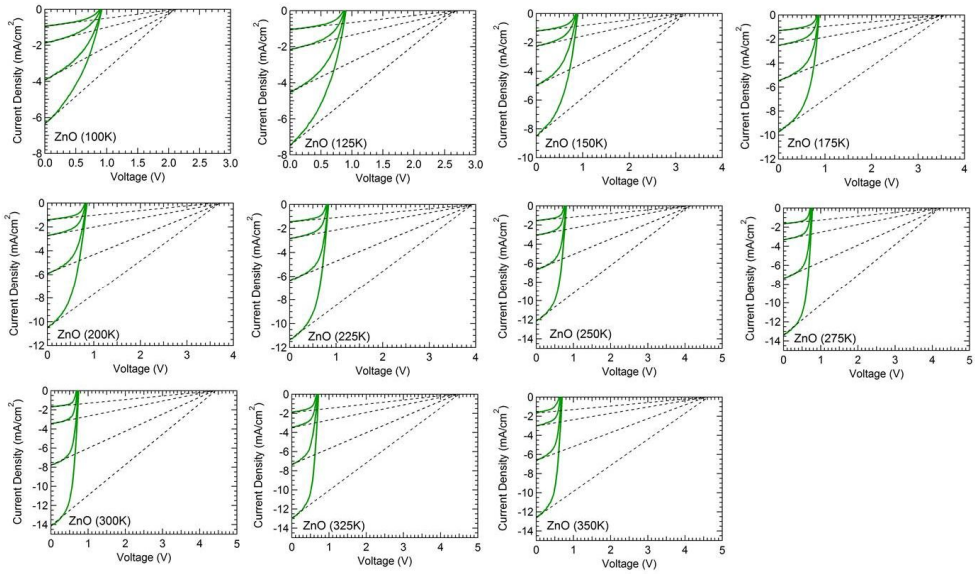


Figure 3.40 J-V curves of the inverted polymer solar cells using ZnO under the various incident light intensity and temperature to evaluate collection voltages (V_C)

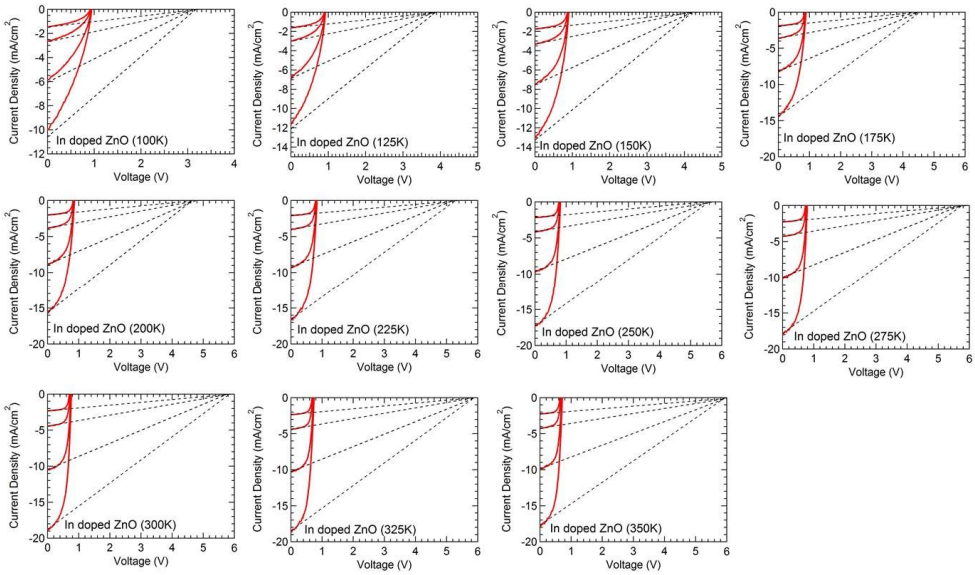


Figure 3.41 J-V curves of the inverted polymer solar cells using In doped ZnO under the various incident light intensity and temperature to evaluate collection voltages (V_C)

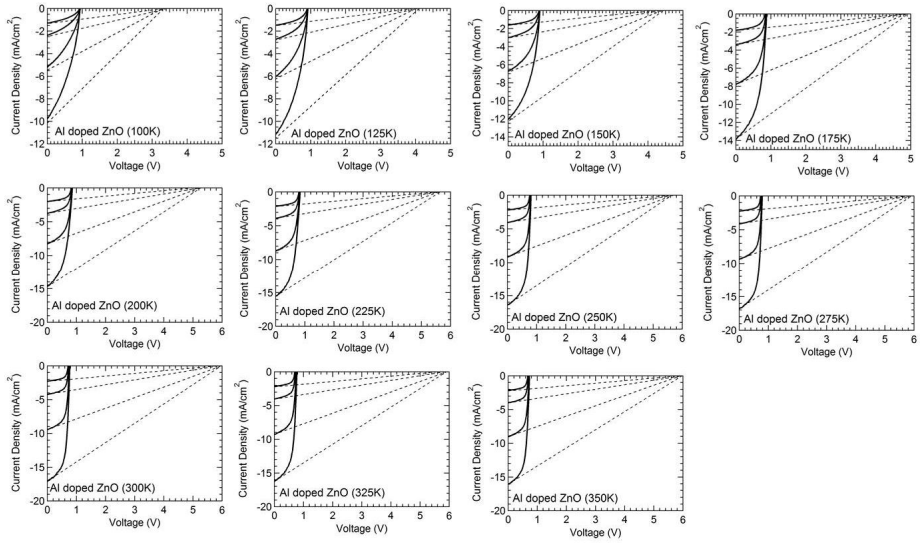


Figure 3.42 J-V curves of the inverted polymer solar cells using Al doped ZnO under the various incident light intensity and temperature to evaluate collection voltages (V_C)

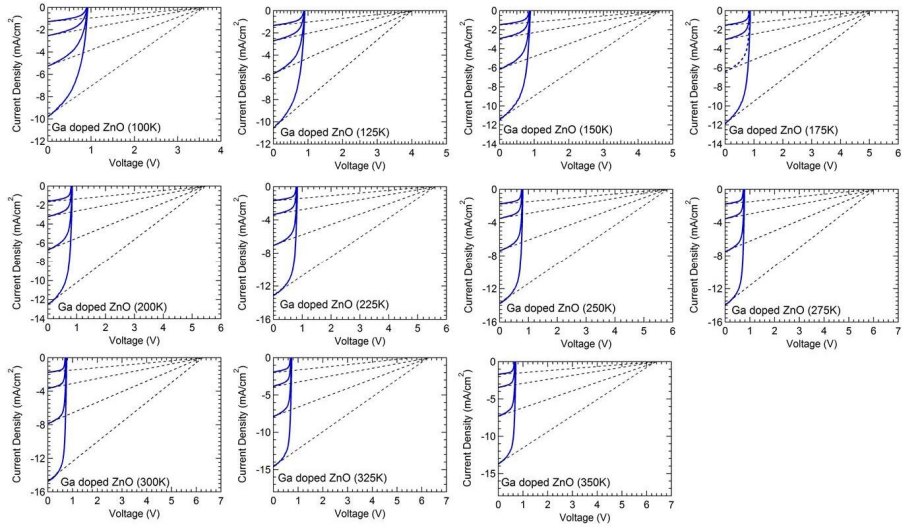


Figure 3.43 J-V curves of the inverted polymer solar cells using Ga doped ZnO under the various incident light intensity and temperature to evaluate collection voltages (V_C)

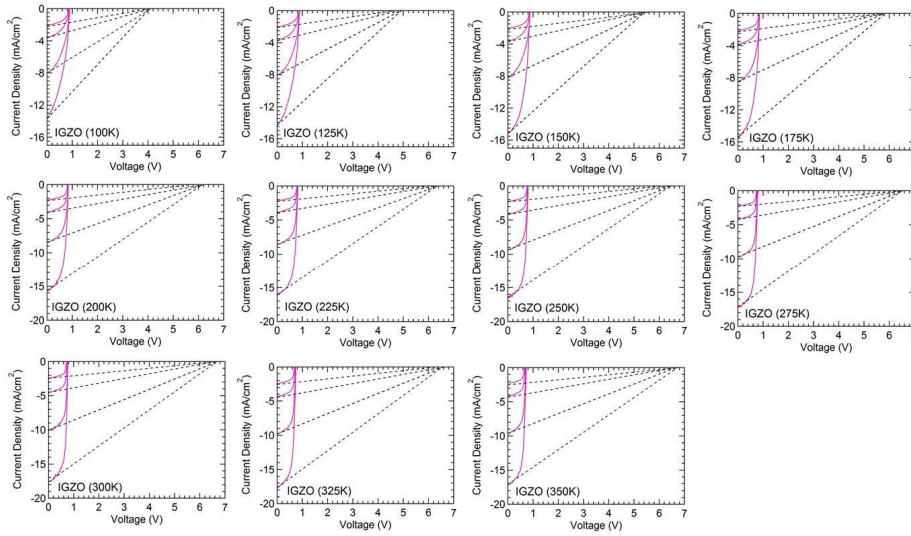


Figure 3.44 J-V curves of the inverted polymer solar cells using IGZO under the various incident light intensity and temperature to evaluate collection voltages (V_C)

Figure 3.40 ~ Figure 3.44 display the J-V curves of the inverted polymer solar cells with different electron extraction layers under various incident light and temperature. All linear fit of J-V curves of various incident light intensity at short circuit conditions ($V=0$), intersect the x-axis at a single point of voltage. This point can be defined as a collection voltage V_C , in the sense that higher values of V_C would mean lower recombination losses [97]. From these V_C data we can calculate the carrier collection length (l_{C0}), carrier collection efficiency (η_{C0}) and $\mu\tau_{eff}$ of our studied inverted polymer solar cells as shown in Figure 3.45. Collection voltages of inverted polymer solar cells with In, Al, Ga doped ZnO and especially IGZO electron extraction layer exhibits the highest temperature dependence as compared to that of ZnO layer. Moreover, the tendency of l_{C0} , η_{C0} and $\mu\tau_{eff}$, have similar. These results are indicate that charge carriers of In, Al, Ga doped ZnO and especially IGZO based devices are efficiently extracted to the electrode without large

recombination between the interfacial and active layer. As a result, because the carrier extraction properties are improved, the J_{SC} , FF and PCE of In, Al, Ga doped ZnO and especially IGZO based devices are better than that of the ZnO based device.

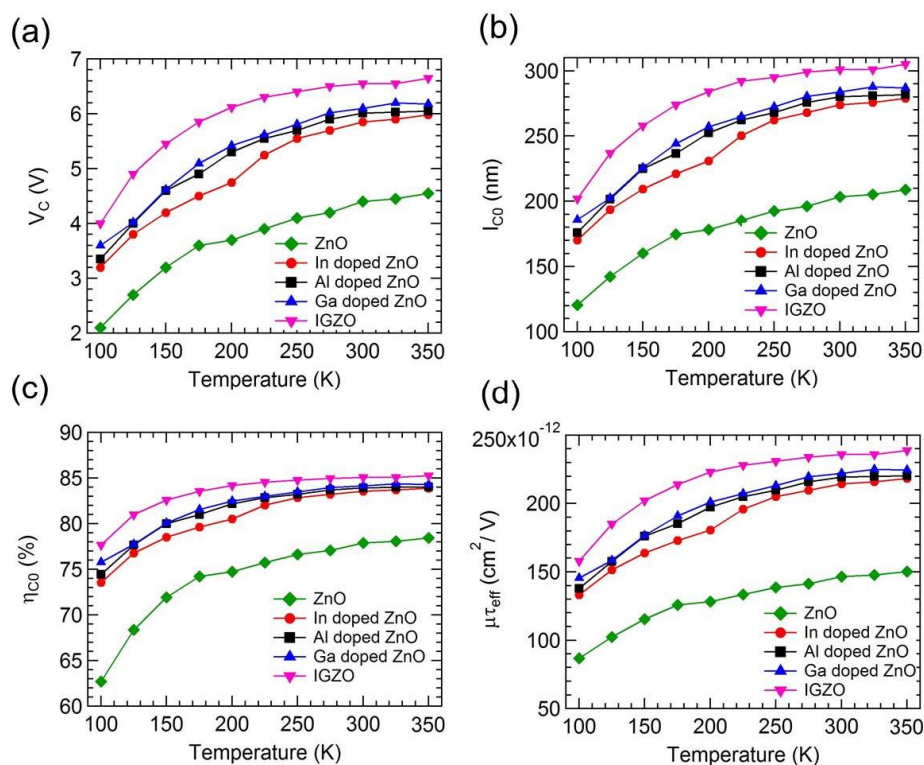


Figure 3.45 (a) Collection voltage (b) carrier collection length at short circuit condition (c) carrier collection efficiency at short circuit condition (d) effective $\mu\tau$ product of inverted polymer solar cells with different electron extraction layer

3.6 Summary

In, Al, Ga doped ZnO nanocrystalline thin films with different In, Al, Ga concentrations and amorphous IGZO thin films with different Zn concentrations have been synthesized by the sol-gel method. The effect of In, Al, Ga doping on the structural, morphological, optical and electrical properties of the ZnO thin films as well as IGZO have been systematically investigated. The grain size and surface roughness values of the In, Al, Ga doped ZnO and IGZO thin films are observed to be smaller than those of the ZnO thin films. Inverted polymer solar cell devices with structure of ITO / In, Al, Ga doped ZnO and IGZO / Polymer:PC₇₀BM / MoO₃ / Al have been fabricated, in which In, Al, Ga doped ZnO and IGZO serves as an electron extraction layer. The PCDTBT:PC₇₀BM based inverted polymer solar cell fabricated with 6.74 at.% In doped ZnO, 5.83 at.% Al doped ZnO and 5.03 at.% Ga doped ZnO films showed a significantly increased power conversion efficiency of 5.58 %, 5.60 % and 5.56 compared to that of ZnO film (3.63 %). The improvement in J_{SC} and PCE of the 6.74% In doped ZnO, 5.83 at.% Al doped ZnO and 5.03 at.% Ga doped ZnO may attributed to the optimal presence of indium in the In doped ZnO, aluminum in the Al doped ZnO and gallium in the Ga doped ZnO thin films.

In order to enhanced power conversion efficiency more, we used PTB7 and PTB7-Th as a doner materials by incorporating high-quality optimized metal oxides such as In, Al, Ga doped ZnO and IGZO. As a result, the PTB7:PC₇₀BM based inverted polymer solar cells with 6.74 at.% In doped ZnO, 5.83 at.% Al doped ZnO and 5.03 at.% Ga doped ZnO and IGZO (ratio of In:Ga:Zn = 1:1:2.5) show the high efficiency of 7.51 %, 7.67 %, 7.86 % and 8.71 % respectively. Moreover, the PTB7-Th:PC₇₀BM based inverted polymer solar cells with 6.74 at.% In doped ZnO, 5.83 at.% Al doped ZnO and 5.03 at.% Ga doped ZnO and IGZO (ratio of In:Ga:Zn =

1:1:2.5) show the high efficiency of 8.53 %, 8.67 %, 8.72 % and 9.60 % respectively. These PCE values are nearly 25 ~ 35 % improved value as compared to the device with pristine ZnO. This enhanced performance is mainly due to the enhanced optical, morphological and electrical properties of electron extraction layer. Moreover, the injection impedance values and activation energy of In, Al, Ga doped ZnO and IGZO were lower and recombination coefficient was higher than those of ZnO based device, which indicates that electron extraction properties are enhanced.

Chapter 4

Inverted Polymer Solar Cells with Doped TiO_2 as an Electron Extraction Layer

TiO_2 is a well-known semiconductor with a wide band gap (3.0 eV for rutile and 3.2 eV for anatase structure), it only absorbs in the UV regime (less than 5% over the full solar energy) and thus significantly limits its widespread applications [98-99]. A number of works have been carried out in inverted organic solar cells using TiO_2 film as an electron selective layer, owing to its superior air stability as compared to other semiconductor oxides. In this chapter we have investigated the effect of Al, In, Ga, Sn and Zn doping and properties of TiO_2 thin films and have fabricated inverted polymer solar cells. Inverted polymer solar cell containing doped TiO_2 as an electron extraction layer with the device structure of ITO / doped TiO_2 / PTB7:PC₇₀BM / MoO_3 / Al has been fabricated and its characteristics have been studied. Moreover, in order to improve the device performance of inverted polymer solar cell, we report about the development by polyethylene oxide (PEO) modification to the TiO_2 and doped TiO_2 surface.

4.1 Inverted Polymer Solar Cells with Al Doping

Concentration of Al Doped TiO₂ as an Electron Extraction Layer

In the chapter 3.1 to 3.3, we have investigated the effect of In, Al and Ga doping concentration of In doped ZnO, Al doped ZnO and Ga doped ZnO as an electron extraction layer for inverted polymer solar cells. As a result, nearly at 5 ~ 6 at.% doped ZnO, the power conversion efficiency is best. In this part, a systematic study has been carried out to understand the effect of Al doping concentration of Al doped TiO₂ electron extraction layer for inverted polymer solar cells with a device structure of ITO / Al doped TiO₂ (different Al doping concentration) / PTB7:PC₇₀BM / Al. Figure 4.1 shows the current density-voltage characteristics and the IPCE spectra of inverted PTB7:PC₇₀BM solar cells with pristine TiO₂ and the Al doped TiO₂ with different Al doping concentration as an electron extraction layer. Table 4.1 summarizes all the photovoltaic parameters. Among the devices, when the TiO₂ was doped with 1 at. % of Al, device exhibited the highest J_{SC}, FF and PCE values: J_{SC} = 15.34 mA/cm², V_{OC} = 0.76 V, FF = 65.85 %, and PCE = 7.68 %. At 1 at.% condition, The Al and TiO₂ were appropriate combined, which formed the good electron transport path. However, when the Al was doped over 1 at.% in TiO₂, the power conversion efficiencies were decreased. It is observed that a further increase of the doping concentration to 3 and 9 at.% aluminum leads to increased R_s (8.17 to 22.03 Ω·cm²) and decreased R_{sh} (815.59 to 490.89 Ω·cm²). These results lead to the decrease of FF from 60.57 to 44.87 % respectively. It is evident that this decrease in FF results in the decrease of the PCE from 7.07 % to 4.99 %

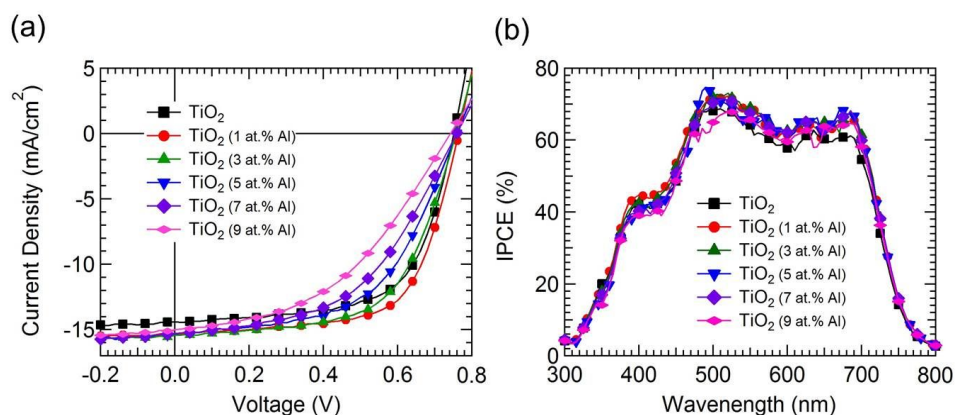


Figure 4.1 (a) J-V characteristics and (b) IPCE spectra of inverted polymer solar cell using Al doped TiO₂ with different Al doping concentration

Table 4.1 Device performance of the inverted polymer solar cells using pristine TiO₂ and Al doped TiO₂ with different Al doping concentration under AM1.5G illumination with 100 mW/cm² light intensity.

	TiO ₂	Al-doped TiO ₂				
		1 at. %	3 at. %	5 at. %	7 at. %	9 at. %
J _{SC} (mA/cm ²)	14.31	15.34	15.43	15.39	15.30	14.99
V _{OC} (V)	0.75	0.76	0.76	0.76	0.76	0.74
FF (%)	63.92	65.58	60.57	54.60	49.85	44.87
PCE (%)	6.98	7.68	7.07	6.38	5.79	4.99
R _s (Ω·cm ²)	6.41	6.03	8.17	17.69	20.37	22.03
R _{sh} (Ω·cm ²)	1135.03	1417.96	815.59	753.46	502.15	490.89

4.2 Inverted Polymer Solar Cells with Metal-Doping Dependent TiO_2 as an Electron Extraction Layer

In case of TiO_2 , the best metal doping concentration is 1 at.%. In this part, we have investigated the effects of Al, Ga, In, Sn and Zn doping on the structural and morphological properties of TiO_2 thin films and the photovoltaic performance of inverted polymer solar cells with the structure of ITO / In, Al, Ga, Sn and Zn doped TiO_2 / PTB7:PC₇₀BM / MoO₃ / Al.

4.2.1 Structural and Morphological Properties of Various Metal Doped TiO_2

Figure 4.2 shows the x-ray diffraction pattern of pristine TiO_2 and Al, In, Ga, Sn and Zn doped TiO_2 films. The (101) diffraction peaks are almost similar.

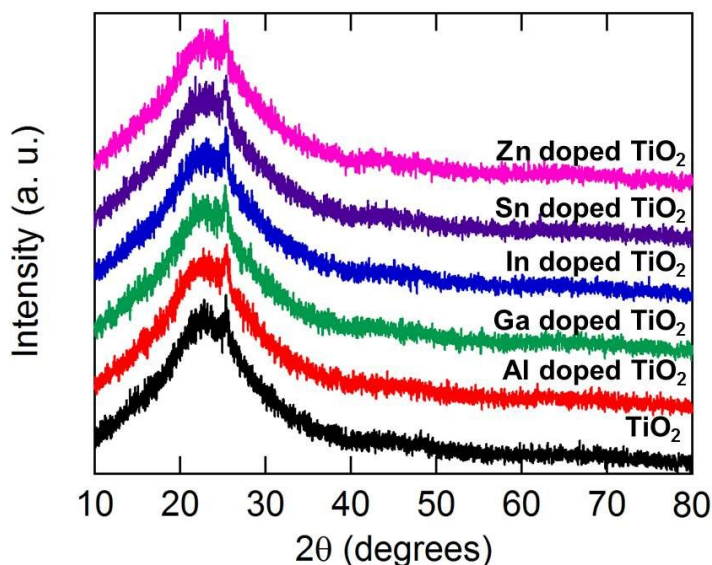


Figure 4.2 X-ray diffraction pattern of TiO_2 and Al, In, Ga, Sn and Zn doped TiO_2

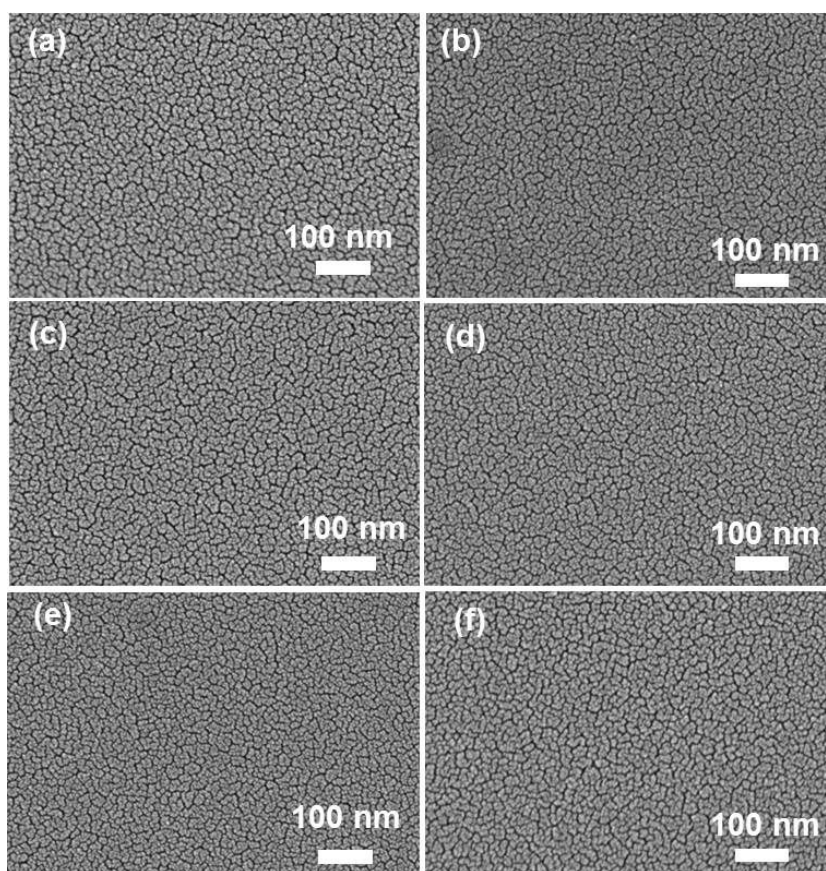


Figure 4.3 FESEM images of (a) TiO_2 (b) Al doped TiO_2 (c) In doped TiO_2 (d) Ga doped TiO_2 (e) Sn doped TiO_2 (f) Zn doped TiO_2

Figure 4.3 shows the FESEM images of TiO_2 and Al, In, Ga, Sn and Zn doped TiO_2 thin films. It is observed that grains are small and are uniformly distributed throughout the surface. The atomic force microscopy (AFM) images of pristine TiO_2 and Al, In, Ga, Sn and Zn doped TiO_2 films are shown in Figure 4.4. It reveals that the films are uniform without any cracks and is continuous with very well connected grains. The root-mean-square (RMS) surface roughness is found to be 2.82, 2.68, 2.53, 2.62, 2.61 and 2.70 nm for TiO_2 , Al doped TiO_2 , In doped TiO_2 , Ga doped TiO_2 , Sn doped TiO_2 and Zn doped TiO_2 respectively. The smoother surface should enable

a more uniform interfacial contact between the electron extraction layers and active layers, which could benefit the increase of the electron extraction and collection efficiency. The higher surface roughness may indicate non-uniform coverage, which may in turn affect the contact resistance. It is observed that the morphology improvement of the electron extracting interface after doping is responsible for the better performance of the device.

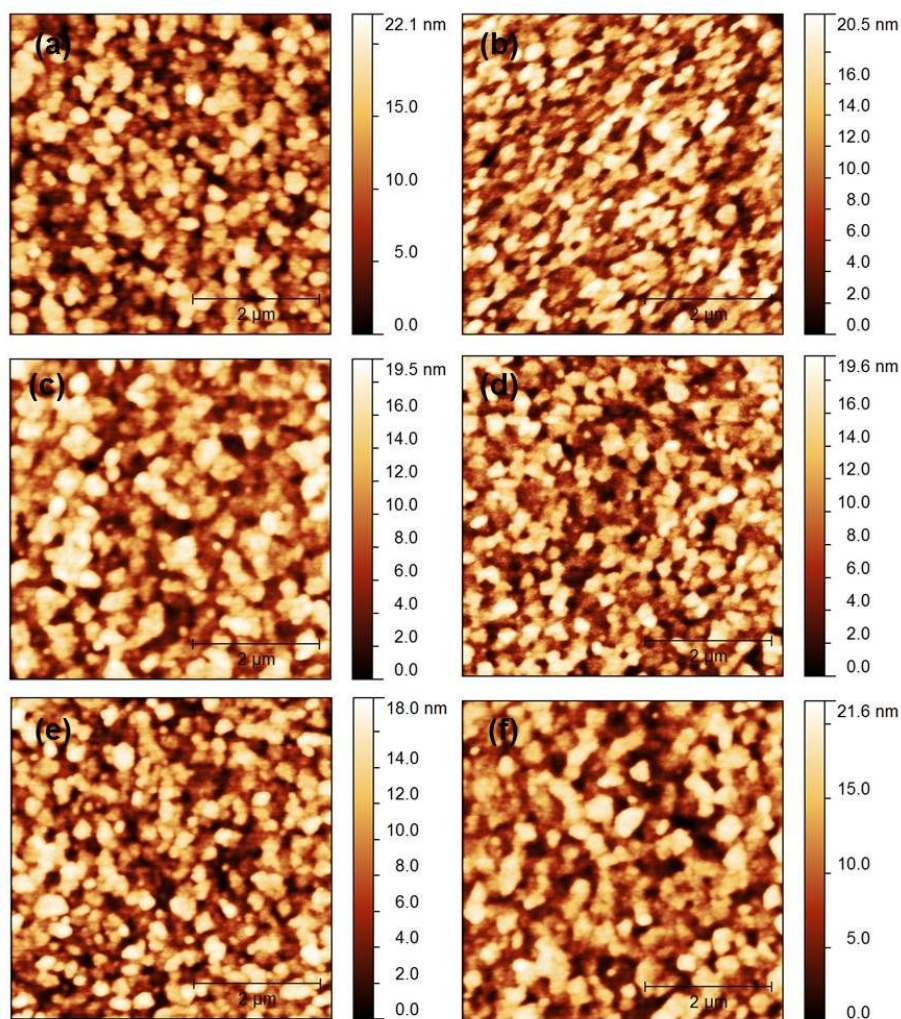


Figure 4.4 AFM images of (a) TiO_2 (b) Al doped TiO_2 (c) In doped TiO_2 (d) Ga doped TiO_2 (e) Sn doped TiO_2 (f) Zn doped TiO_2

The size of the particles in Al, In, Ga, Sn and Zn doped TiO₂ films have been studied using high resolution transmission electron microscope (HRTEM). The HRTEM image clearly shows (Figure 4.5 (a)) that pristine TiO₂ particles have agglomerated. The particle size of TiO₂ has been obtained as 12.7 nm. Figure 4.5 (d, g, j, m, p) shows HRTEM image of Al, In, Ga, Sn and Zn doped TiO₂. It is observed that all the particles have agglomerated. The average particle size of Al, In, Ga, Sn and Zn doped TiO₂ are found to be 11 ~ 12 nm. The HRTEM image shown in Figure 4.5 (b, e, h, k, n, q)) exhibit lattice fringes and the lattice spacing has been calculated using these fringes. The lattice spacing is found to be 3.51 Å and 3.47 ~ 3.49 Å for TiO₂ and Al, In, Ga, Sn and Zn doped TiO₂ and this corresponds to the (101) plane of anatase TiO₂. The selected area electron diffraction (SAED) pattern exhibits concentric circles revealing that the TiO₂ (Figure 4.5 (c)) and Al, In, Ga, Sn and Zn-doped TiO₂ (Figure 4.5 (f, i, l, o, r))) are of nanocrystalline nature made up of small grains. The rings correspond to the (101), (004), (200), and (105) planes of the anatase TiO₂. The d spacing values calculated from these images are in close agreement with the standard data of JCPDS card no.841286

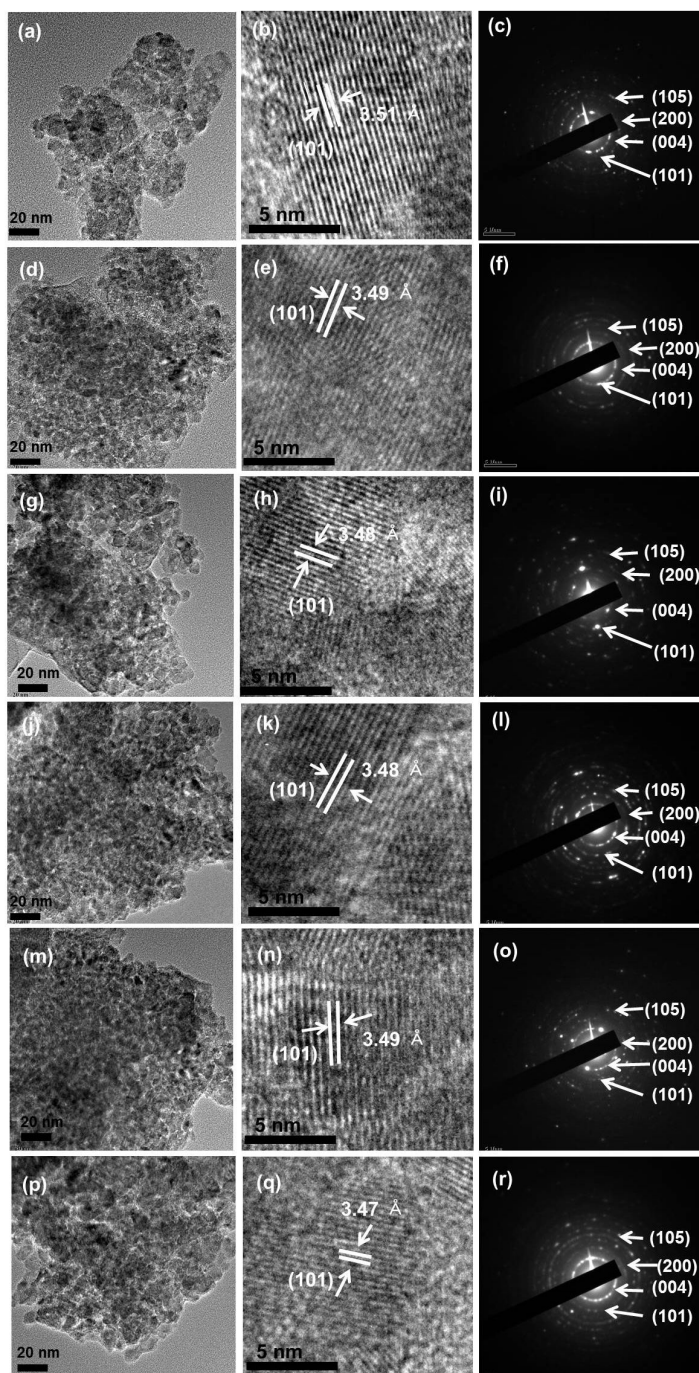


Figure 4.5 HRTEM, SAED images of (a, b, c) TiO_2 , (d,e,f) Al doped TiO_2 , (g,h,i) In doped TiO_2 , (j,k,l) Ga doped TiO_2 , (m,n,o) Sn doped TiO_2 and (p,q,r) Zn doped TiO_2

4.2.2 Electrical Properties of Metal Doped TiO₂

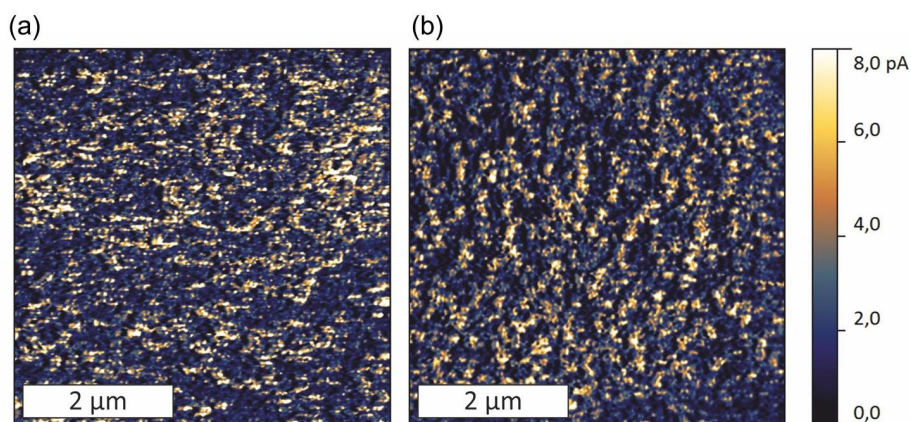


Figure 4.6 The tip-sample current of (a) TiO₂ and (b) Sn doped TiO₂ surfaces measured by conductive AFM (C-AFM) at a sample bias of 550 mV

We carry out the conductive AFM (C-AFM) measurement in order to analyze the electrical conductivity maps of TiO₂ and Sn doped TiO₂ thin films. In C-AFM, a DC voltage is applied to the sample and the electrical tip-sample current is measured. Thereby, the magnitude of the local tip-sample current is a measure of the sample conductance underneath the tip. Current maps of the TiO₂ and Sn doped TiO₂ layer surfaces have been recorded (Figure 4.6). Both qualitatively (concerning the current patterns) and quantitatively, the current patterns do not show any difference: The average current of TiO₂ and Sn doped TiO₂ thin films were almost identical (2.2 pA and 2.4 pA respectively). The results demonstrate that Sn doping did not have a negative effect on the homogeneity of the sample conductivity.

4.2.3 Device Characteristics with Various Metal Doped TiO₂

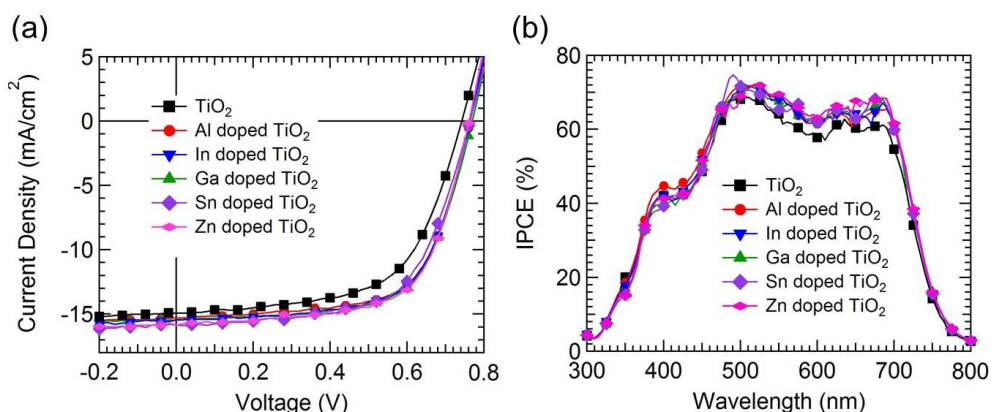


Figure 4.7 (a) J-V characteristics and (b) IPCE spectra of inverted polymer solar cell using pristine TiO₂ and Al, In, Ga, Sn and Zn doped TiO₂

Table 4.2 Device performance of the inverted polymer solar cells with TiO₂ and Al, In, Ga, Sn and Zn doped TiO₂ at 1 at.% doping concentration under AM1.5G illumination with 100 mW/cm² light intensity.

	TiO ₂	Various metal doped TiO ₂ (1 at.%)				
		Al	In	Ga	Sn	Zn
J _{SC} (mA/cm ²)	14.92	15.27	15.45	15.47	15.85	15.84
V _{OC} (V)	0.74	0.76	0.76	0.77	0.76	0.76
FF (%)	60.62	65.69	65.07	64.86	62.77	65.24
PCE (%)	6.79	7.66	7.67	7.72	7.59	7.87
R _s (Ω·cm ²)	7.63	6.01	6.15	6.20	6.39	6.09
R _{sh} (Ω·cm ²)	1003.10	1393.41	1317.80	1302.28	1219.32	1349.45

The current density-voltage (J-V) characteristics of the PTB7:PC₇₀BM based inverted polymer solar cells fabricated using pristine TiO₂ and Al, In, Ga, Sn and Zn

doped TiO₂ are shown in Figure 4.7. The pristine TiO₂ based device exhibits a short circuit current density (J_{SC}) of 14.92 mA/cm², open circuit voltage (V_{OC}) of 0.74 V, fill factor (FF) of 60.62 % and power conversion efficiency (PCE) of 6.70 %. It can be seen that the Al, In, Ga, Sn and Zn doped TiO₂ based inverted polymer solar cells exhibits a little enhanced photovoltaic response with PCE of 7.59 ~ 7.87 %, J_{SC} of 15.27 ~ 15.85 mA/cm², V_{OC} of 0.76 ~ 0.77 V and FF of 62.77 ~ 65.69 %. The results indicate that PCE of the TiO₂ based devices can be improved through metal doping. The enhanced J_{SC} and FF in the inverted polymer solar cells is due to the fact that the series resistance (R_s) in the inverted polymer solar cells with Al, In, Ga, Sn and Zn doped TiO₂ layer is smaller than that of TiO₂ layer, and shunt resistance (R_{sh}) of the inverted polymer solar cells with Al, In, Ga, Sn and Zn doped TiO₂ layer is larger than that TiO₂ layer. The R_s decreases from 7.63 (TiO₂) to 6.01 ~ 6.39 $\Omega \cdot \text{cm}^2$ (doped TiO₂) and R_{sh} increases from 1003.10 (TiO₂) to 1219.32 ~ 1393.41 $\Omega \cdot \text{cm}^2$ (doped TiO₂). The IPCE spectra of PTB7:PC₇₀BM based inverted polymer solar cells are shown in Figure 4.7 (b). It is observed that Al, In, Ga, Sn and Zn doped TiO₂ based device exhibits a maximum IPCE of 72 %, which is higher than 68 % of the TiO₂ device. This indicates that the Al, In, Ga, Sn and Zn doped TiO₂ devices have better carrier extraction properties and carrier collection efficiency. The J_{SC} values have been calculated using the IPCE data with an AM1.5G reference spectrum. The J_{SC} is found to be 13.77 and 14.69, 14.56, 14.52, 14.51 and 14.76 mA/cm² for TiO₂ and Al, In, Ga, Sn and Zn doped TiO₂ respectively. These values match well with those obtained from J-V measurement. However, it is also noted (chapter 4.1) that further increase of the doping concentration to more than 2 at.% leads to the decrease of the device performance with lower J_{SC} and FF (Figure 4.8 and Table 4.3). The reduction in device performance is because higher doping

concentration introduces saturated electron barrier height and more electron trapping sites, which is disadvantageous for photocurrent extraction.

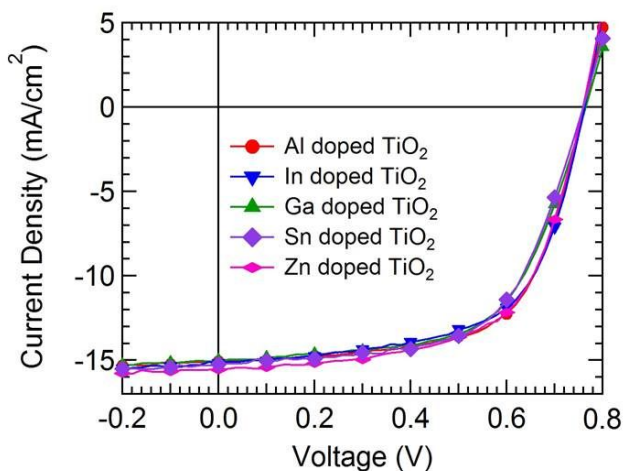


Figure 4.8 J-V characteristics of inverted polymer solar cell using TiO₂ and Al, In, Ga, Sn and Zn doped TiO₂ at 2 at.% doping concentration.

Table 4.3 Device performance of the inverted polymer solar cells with TiO₂ and Al, In, Ga, Sn and Zn-doped TiO₂ at 2 at.% under AM1.5G illumination with 100 mW/cm² light intensity.

	Various metal doped TiO ₂ (2 at.%)				
	Al	In	Ga	Sn	Zn
J _{SC} (mA/cm ²)	15.07	15.18	15.01	15.24	15.55
V _{OC} (V)	0.76	0.76	0.76	0.76	0.76
FF (%)	63.89	61.72	61.39	61.08	62.26
PCE (%)	7.35	7.14	7.05	7.07	7.35

4.2.4 Temperature and Light Intensity Characteristics with Various Metal Doped TiO₂

In order to analysis the influence of doping effect of TiO₂ for inverted polymer solar cell performance, we carried out temperature (T) dependent J-V measurements (100 ~ 350 K) at different light power (P_{Light} , 1 ~ 100 mW/cm²) and analyzed the device characteristics. Figure 4.9 shows the light intensity dependence of J_{SC} at various temperature (100 ~ 350 K) in a log-log plot. The J_{SC} follows a power law dependence ($J_{\text{SC}} = P_{\text{Light}}^{\alpha}$). In the case of the inverted polymer solar cell with the different electron extraction layers, α are 0.932 ~ 0.944 for Al doped TiO₂, 0.921 ~ 0.954 for In doped TiO₂, 0.901 ~ 0.953 for Ga doped TiO₂, 0.930 ~ 0.950 for Sn doped TiO₂ and 0.919 ~ 0.951 for Zn doped TiO₂ in the temperature range of 100 ~ 350 K. The α of all doped TiO₂ is almost similar. However in case of the device using TiO₂, α is 0.810 ~ 0.884 in the temperature range of 100 ~ 350 K, which are much lower than those of all doped TiO₂. This result indicates that the bimolecular recombination process is less in the device with the In, Al, Ga, Sn and Zn doped TiO₂. Therefore, the insertion of the doped TiO₂ layer reduces the bimolecular recombination loss owing to enhanced carrier extraction efficiency, resulting in enhanced device performance [91-92].

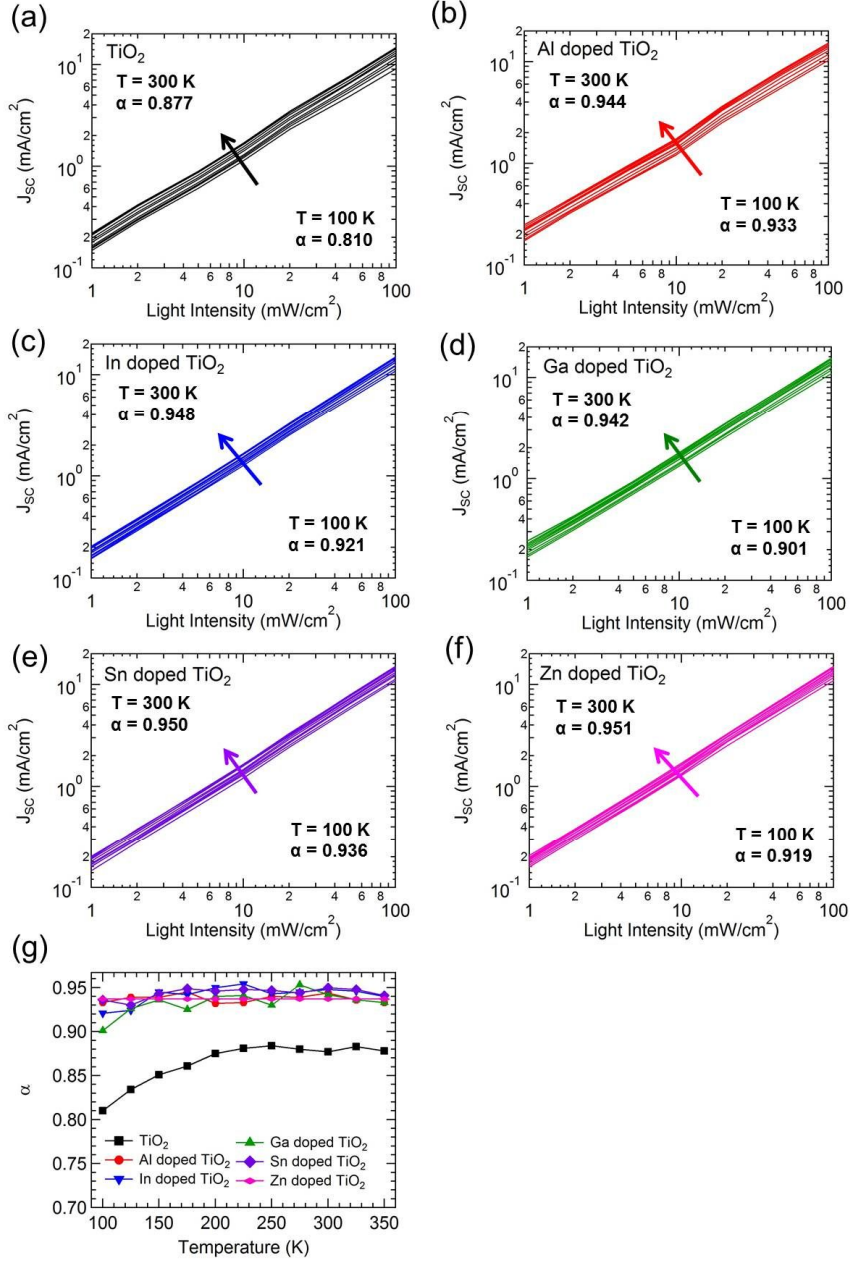


Figure 4.9 J_{SC} as a function of light intensity (1-100 mW/cm^2) for various temperatures (100-350 K) for inverted polymer solar cells (a) TiO_2 (b) Al doped TiO_2 (c) In doped TiO_2 (d) Ga doped TiO_2 (e) Sn doped TiO_2 (f) Zn doped TiO_2 and (g) Recombination coefficient obtained in the temperature range of 100-350 K

Figure 4.10 plots $\ln(J_{sc})$ vs $1000/T$ along with various light intensities ($10 \sim 100 \text{ mW/cm}^2$) and the activation energy Δ is obtained from the slope. The activation energy of the device using doped TiO_2 ($6.50 \sim 7.20 \text{ meV}$, $5.94 \sim 6.68 \text{ meV}$, $6.26 \sim 7.10 \text{ meV}$, $6.52 \sim 6.85 \text{ meV}$ and $6.28 \sim 6.58 \text{ meV}$ for Al doped TiO_2 , In doped TiO_2 , Ga doped TiO_2 , Sn doped TiO_2 and Zn doped TiO_2) is lower than that of the device with TiO_2 ($7.41 \sim 8.81 \text{ meV}$) in the whole illumination intensity range, as depicted in Figure 4.10 (f). This result indicates that the carrier transport and extraction are enhanced in the device with Al, In, Ga, Sn and Zn doped TiO_2 , consistent with the enhanced J_{sc} and FF for the device with Al, In, Ga, Sn and Zn doped TiO_2 shown in Figure 4.7 (a)

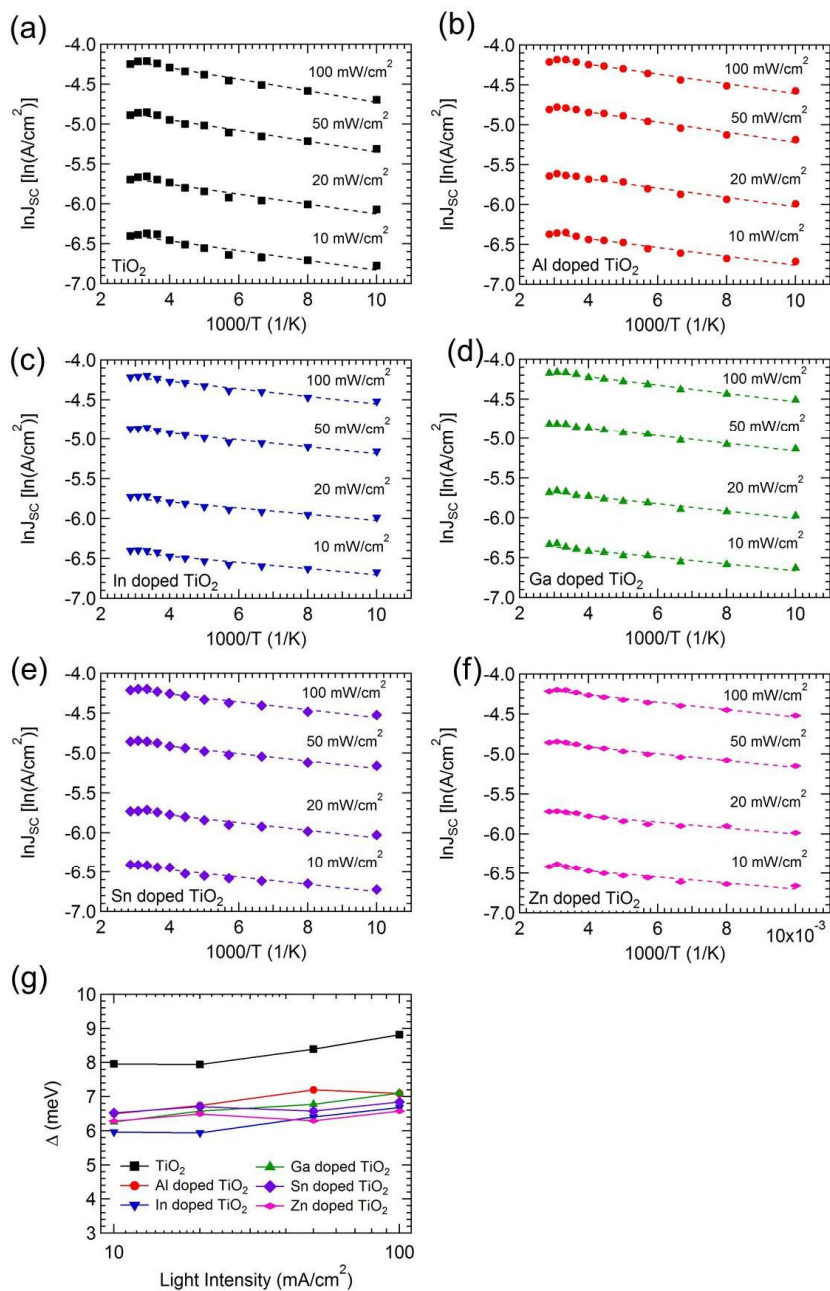


Figure 4.10 Arrhenius plot of J_{SC} against T for the inverted polymer solar cells with different extraction layer (a) TiO₂ (b) Al doped TiO₂ (c) In doped TiO₂ (d) Ga doped TiO₂ (e) Sn doped TiO₂ (f) Zn doped TiO₂ and (g) activation energy extracted from the data shown in (a) to (f).

4.3 Inverted Polymer Solar Cells with Polyethylene Oxide (PEO) Modified TiO_2 as an Electron Extraction Layer

In this part, in order to improve the inverted device performance based on TiO_2 and doped TiO_2 as an electron extraction layer, we report about the development of a generally applicable electron extraction layer by polyethylene oxide (PEO) modification to the TiO_2 and Zn doped TiO_2 (ZTO) surface. The inverted device is ITO / PEO modified TiO_2 or Zn doped TiO_2 / PTB7:PC₇₀BM / MoO_3 / Al shown in Figure 4.11.

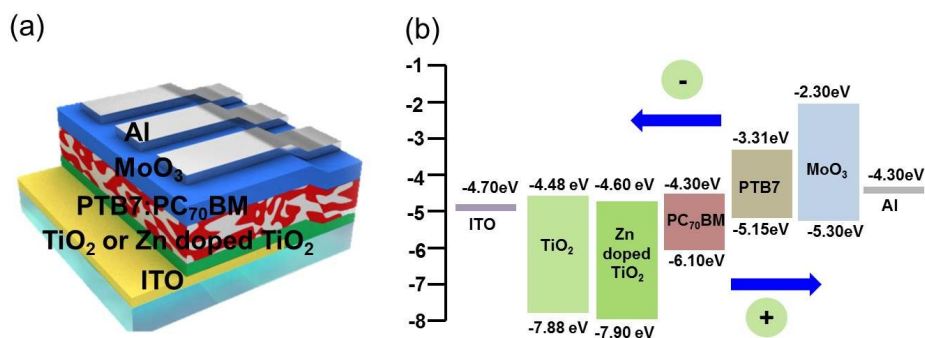


Figure 4.11 (a) Device structure and (b) energy level diagrams of inverted polymer solar cells with TiO_2 and Zn doped TiO_2 as an electron extraction layer

4.3.1 Optical Properties of PEO Modified TiO_2 and Zn doped TiO_2

The work function of TiO_2 , PEO modified TiO_2 (PEO: TiO_2), ZTO and PEO modified ZTO (PEO:ZTO) films were measured by ultraviolet photoelectron spectroscopy (UPS), and band gap (E_g) were obtained from the UV absorption spectra and are as shown in Figure 4.12, Figure 4.13 and Table 4.4.

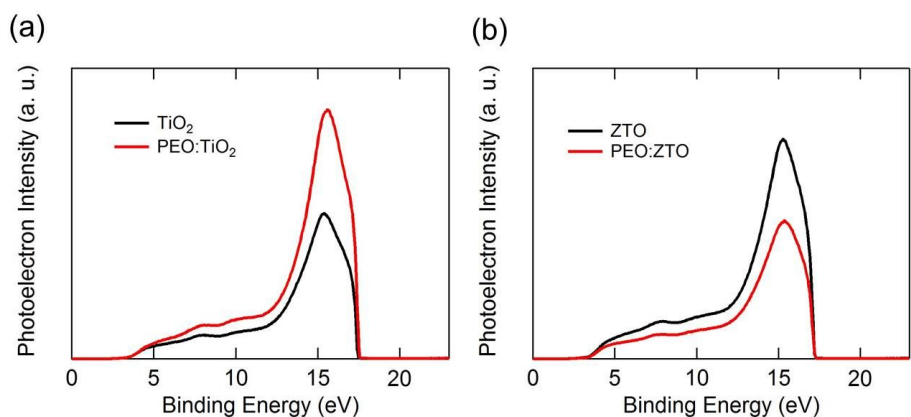


Figure 4.12 UPS spectra of (a) TiO_2 , 0.05 wt.% PEO: TiO_2 and (b) ZTO, 0.05 wt.% PEO:ZTO films

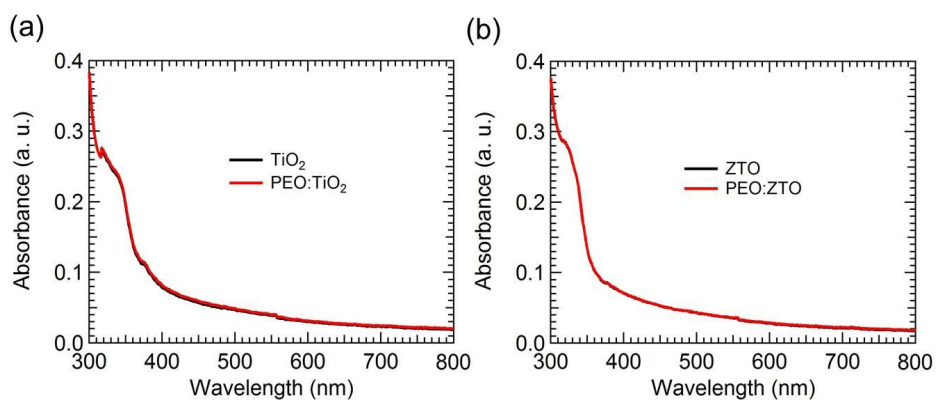


Figure 4.13 Absorption spectra of (a) TiO_2 , 0.05 wt.% PEO: TiO_2 and (b) ZTO, 0.05 wt.% PEO:ZTO films

Table 4.4 Valance band, conduction band and band gap of TiO₂, 0.05 wt.% PEO:TiO₂, ZTO and 0.05 wt.% PEO:ZTO films.

	TiO ₂	0.05 wt.% PEO:TiO ₂	ZTO	0.05 wt.% PEO:ZTO
Valence Band Maximum (VBM) [eV]	-7.66	-7.61	-7.90	-7.92
Conduction Band Maximum (CBM) [eV]	-4.46	-4.41	-4.60	-4.62
Band gap (E _g) [eV]	3.20	3.20	3.30	3.30

In order to study the composition of TiO₂ and ZTO films, the x-ray photoelectron spectroscopy (XPS) measurements were carried out. The XPS spectra of TiO₂ and ZTO films are shown in Figure 4.14. The binding energies of ZTO are 457.02 eV, 462.77 eV and 528.21 eV for Ti2p_{3/2}, Ti2p_{1/2} and O1s respectively. The binding energies are found to be shifted towards the higher energy side compared to TiO₂ (456.6, 462.42 and 527.85 eV for Ti2p_{3/2}, Ti2p_{1/2} and O1s, respectively). This result suggests that zinc is incorporated into the TiO₂ lattice. Figure 4.14 (c) shows the peaks at 1019.89 eV and 1042.86 eV corresponding to the Zn2p_{3/2} and Zn2p_{1/2} binding energy levels of zinc. The chemical constituents present in the sample according to the XPS results are Ti = 24.32 at.%, and O = 75.68 at.% for TiO₂, Ti = 23.50 at.%, O = 74.82 at.%, Zn = 1.68 at.% for ZTO.

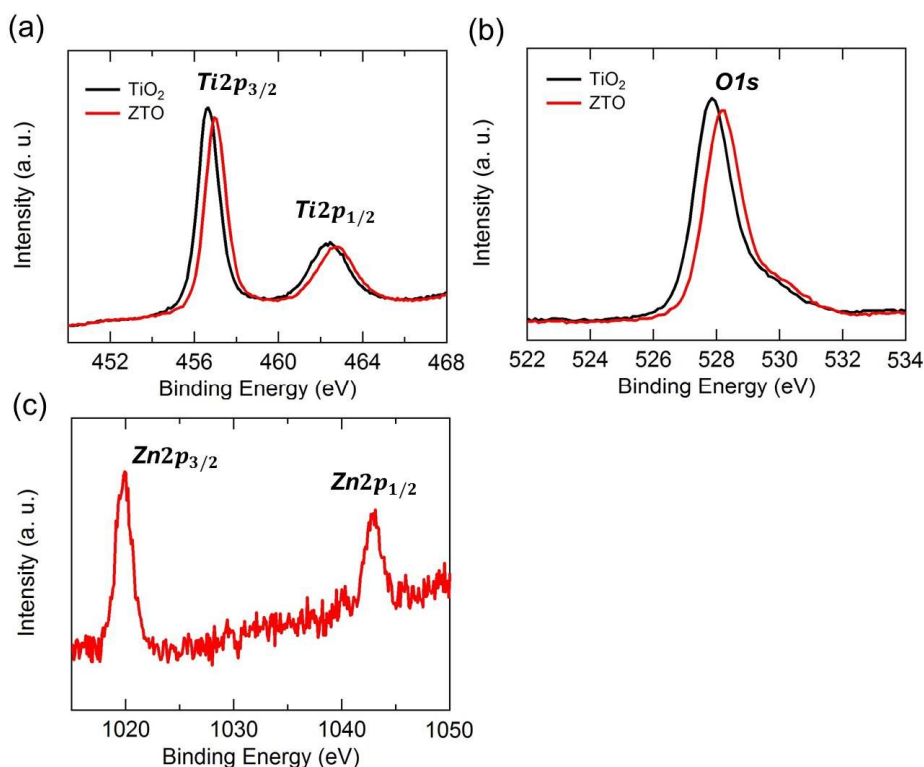


Figure 4.14 XPS spectra of TiO_2 and ZTO films (a) $\text{Ti}2p$, (b) $\text{O}1s$ and (c) $\text{Zn}2p$

Figure 4.15 (a) shows the absorption spectra of PTB7:PC₇₀BM, TiO_2 /PTB7:PC₇₀BM and ZTO/PTB7:PC₇₀BM films. The PTB7:PC₇₀BM blend film exhibits a strong absorption covering a range from 300 to about 750 nm. It is observed that TiO_2 /PTB7:PC₇₀BM and ZTO/PTB7:PC₇₀BM show strong absorption from 450 to 650 nm when compared to that of PTB7:PC₇₀BM film. Moreover, it could also be seen that Zn dopant improved the optical absorption performance of TiO_2 film. Absorption spectra of TiO_2 and ZTO films are shown in Figure 4.15 (b). Absorption spectra of ZTO shows that the absorption edge is slightly shifted towards the shorter wavelength (blue shift) when compared to TiO_2 . This shift towards shorter wavelength indicates the increase of band gap of Zn doping. It is mainly attributed

to the Burstein-Moss effect, since the absorption edge of a degenerate semiconductor is shifted to shorter wavelengths with increasing carrier concentration [67]

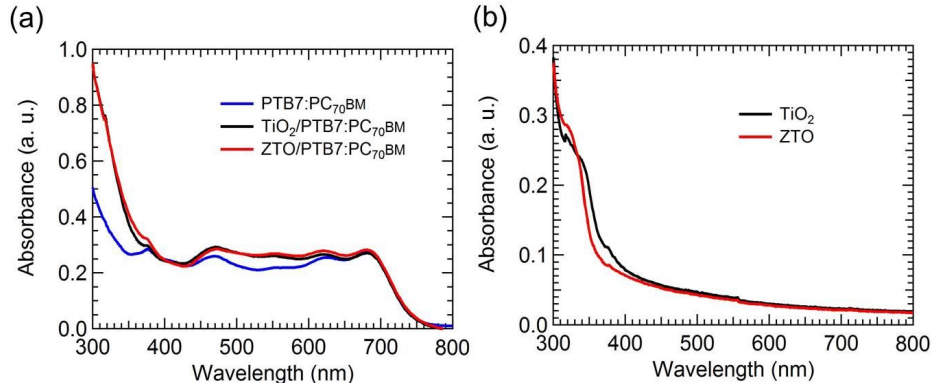


Figure 4.15 Absorption spectra of PTB7:PC₇₀BM, TiO₂/PTB7:PC₇₀BM and ZTO/PTB7:PC₇₀BM films (b) TiO₂ and ZTO films

4.3.2 Electrical Properties of PEO modified TiO₂ and Zn doped TiO₂

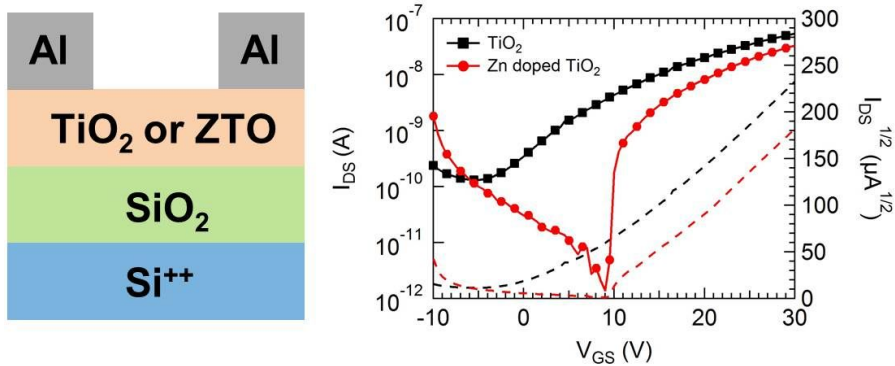


Figure 4.16 TFT device structure and transfer characteristics of TiO₂ and ZTO TFTs

The mobility has been measured by bottom-gate top-contact thin film transistor (TFT) method. The TFT device structure is shown in Figure 4.16. SiO₂ was used as

the gate dielectric layer, and Al was used as the source/drain electrode. The mobility of TiO_2 and ZTO thin films are $3.15 \times 10^{-4} \text{ cm}^2/\text{V}\cdot\text{S}$ and $3.20 \times 10^{-4} \text{ cm}^2/\text{V}\cdot\text{S}$ respectively.

4.3.3 Device Characteristics with PEO Modified TiO_2 and Zn doped TiO_2

The current density-voltage (J-V) characteristics of the PTB7:PC₇₀BM based inverted polymer solar cells fabricated using various PEO:TiO₂ as an electron extraction layer are shown in Figure 4.17 and this has been measured under 100 mW/cm² air mass 1.5 global (AM1.5G) illumination. The solar cell parameters are summarized in Table 4.5. As can be seen, the reference device using pristine TiO₂ shows a J_{SC} of 14.85 mA/cm², V_{OC} of 0.76 V, FF of 62.22 % and PCE of 6.98 %. The device performance was considerably improved when PEO modified TiO₂ was used as the electron extraction layer. The highest efficiency was achieved when 0.05 wt.% PEO modified TiO₂ was used as the electron extraction layer, which exhibited a J_{SC} of 15.51 mA/cm², V_{OC} of 0.76 V, FF of 63.34 % and PCE of 7.51 %. However, as the PEO concentration was further increased, the device performance decreased. When the PEO concentration was increased to 0.3 wt.%, the device showed a reduced J_{SC} of 15.40 mA/cm² and a reduced FF of 61.14 %, giving a PCE of 7.06 %.

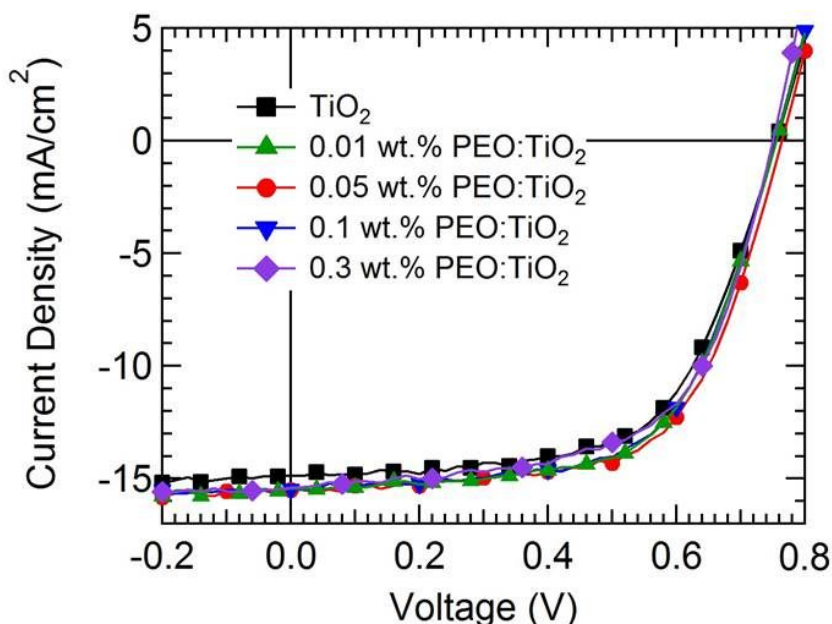


Figure 4.17 J-V characteristics of inverted polymer solar cells based on PTB7:PC₇₀BM using TiO₂ and PEO modified TiO₂

We calculated the series resistance (R_s) and shunt resistance (R_{sh}) from the J-V curve. The reference TiO₂ device shows a R_s of 7.28 $\Omega \cdot \text{cm}^2$ and a R_{sh} of 451.61 $\Omega \cdot \text{cm}^2$, respectively. The 0.05 wt.% PEO:TiO₂ device exhibited the smallest R_s of 6.22 $\Omega \cdot \text{cm}^2$ and highest R_{sh} of 1198.16 $\Omega \cdot \text{cm}^2$. The reduced R_s is favorable for charge extraction and collection, and the increased R_{sh} indicates reduced leakage current as well as restrained recombination loss of carriers, which explains the improved FF and J_{SC} . When the PEO concentration is increased to 0.3 wt.%, the R_s of the device increases to 6.46 $\Omega \cdot \text{cm}^2$, which renders a large energy barrier for charge collection. In this case, many carriers recombine before they are collected at the electrodes. Therefore, small FF and J_{SC} can be expected when charge collection is inefficient due to the presence of large R_s .

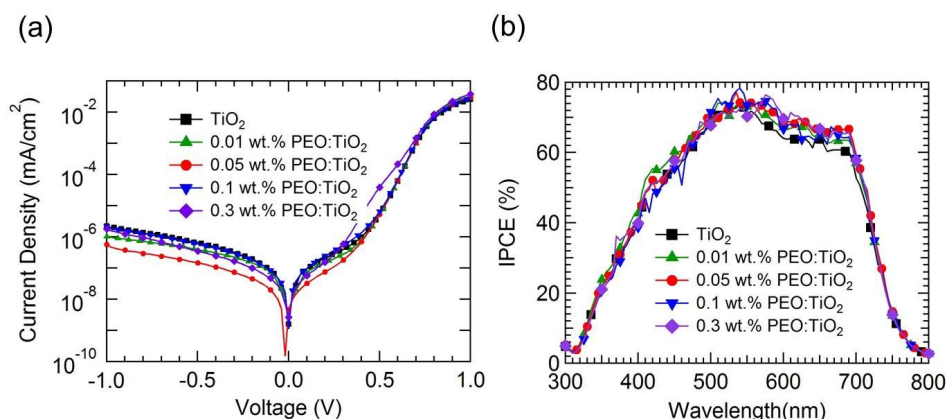


Figure 4.18 (a) dark J-V characteristics and (b) IPCE spectra of inverted polymer solar cells based on PTB7:PC₇₀BM using TiO₂ and PEO modified TiO₂

The dark J-V characteristics shown in Figure 4.18 (a), shows that the 0.05 wt.% PEO:TiO₂ device exhibited excellent diode characteristics and lower leakage current under reverse bias than the device based on the TiO₂. The incident photon to charge carrier efficiency (IPCE) spectra of PTB7:PC₇₀BM based inverted polymer solar cells are shown in Figure 4.18 (b). It is observed that 0.05 wt.% PEO:TiO₂ based device showed a maximum IPCE of 78 %, which is higher than the 72 % of the TiO₂ device. The J_{SC} values have been calculated using IPCE data with an AM1.5G reference spectrum. The J_{SC} is found to be 14.51 and 15.20 mA/cm² for TiO₂ and 0.05 wt.% PEO:TiO₂ respectively. These values match well with those obtained from J-V measurement.

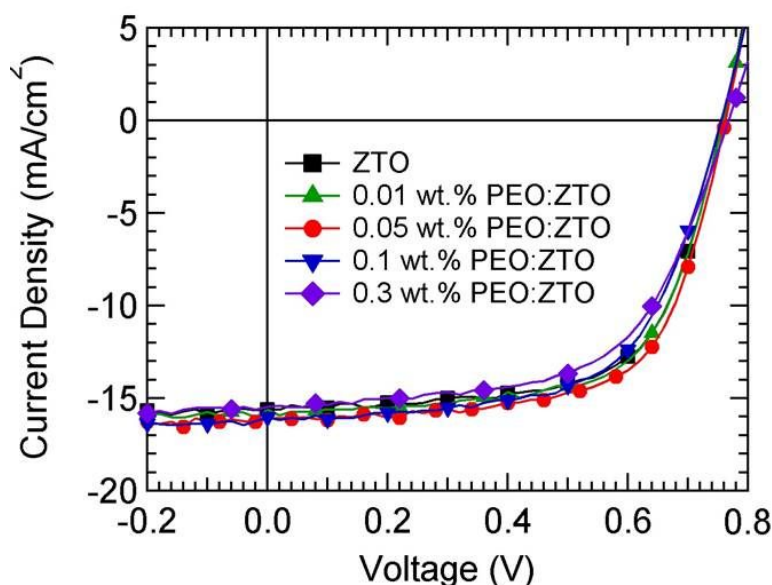


Figure 4.19 J-V characteristics of inverted polymer solar cells based on PTB7:PC₇₀BM using ZTO and PEO modified ZTO

The J-V characteristics of the PTB7:PC₇₀BM based inverted polymer solar cells fabricated using electron extraction layers of ZTO and PEO modified ZTO are shown in Figure 4.19 and Table 4.5. Similar variation in the performance of PEO:ZTO based device was observed as previous PEO:TiO₂ based devices. The 0.05 wt.% PEO modified ZTO device shows considerably improved J_{SC} of 16.14 mA/cm² and FF of 65.83 % as compared to the reference device, which shows a J_{SC} of 15.61 mA/cm² and FF of 64.78 %. Consequently, the device using a 0.05 wt.% PEO modified ZTO layer shows considerable improved PCE of 8.10 % as compared to 7.67 % of the device with the ZTO layer. The IPCE spectra shown in Figure 4.20 (b) confirm the improved J_{SC} of the device based on PEO modified ZTO layer.

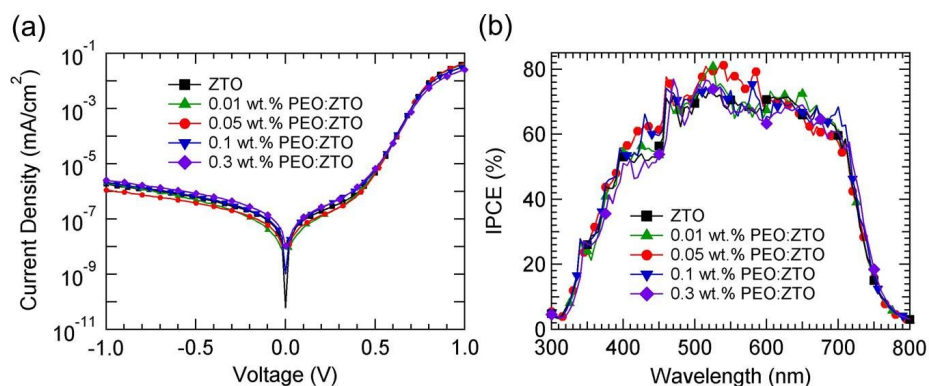


Figure 4.20 (a) dark J-V characteristics and (b) IPCE spectra of inverted polymer solar cells based on PTB7:PC₇₀BM using ZTO and PEO modified ZTO

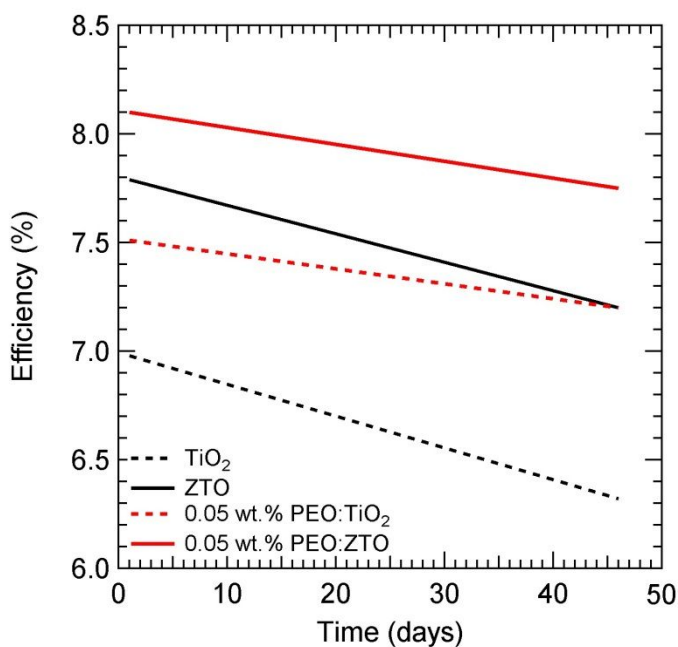


Figure 4.21 The stability of the PTB7:PC₇₀BM based inverted polymer solar cells using TiO₂, 0.05 wt.% PEO:TiO₂, ZTO and 0.05 wt.% PEO:ZTO as an electron extraction layer

Table 4.5 Performance parameters of the devices based on PTB7:PC₇₀BM using PEO:TiO₂ and PEO:ZTO as an electron extraction layers.

	TiO ₂	PEO-modified TiO ₂			
		0.01 wt. %	0.05 wt. %	0.1 wt. %	0.3 wt. %
J _{SC} (mA/cm ²)	14.85	15.43	15.51	15.47	15.40
V _{OC} (V)	0.76	0.76	0.76	0.76	0.75
FF (%)	62.22	62.80	63.34	62.60	61.14
PCE (%)	6.98	7.32	7.51	7.31	7.06
R _s (Ω·cm ²)	7.28	6.39	6.22	6.42	6.46
R _{sh} (Ω·cm ²)	451.61	989.90	1198.16	1026.28	853.46
	ZTO	PEO-modified ZTO			
		0.01 wt. %	0.05 wt. %	0.1 wt. %	0.3 wt. %
J _{SC} (mA/cm ²)	15.61	15.60	16.14	16.02	15.46
V _{OC} (V)	0.76	0.76	0.76	0.76	0.76
FF (%)	64.78	65.80	65.83	62.35	60.06
PCE (%)	7.67	7.79	8.10	7.54	7.13
R _s (Ω·cm ²)	6.33	4.84	4.63	5.88	6.71
R _{sh} (Ω·cm ²)	633.63	1015.10	1376.59	1115.64	997.90

The device performance stability data of TiO₂, 0.05 wt.% PEO:TiO₂, ZTO and 0.05 wt.% PEO:ZTO based devices are shown in Figure 4.21. The solar cells were exposed continuously to air at room temperature (without any encapsulation barrier). We observed that even after 46 days under ambient conditions, TiO₂ and ZTO (without PEO modification) based devices were decreased by ~ 10 % as compared to its original efficiency (6.98 to 6.32% and 7.79 to 7.10% of TiO₂ and ZTO

respectively). On the other hand, 0.05 wt.% PEO:TiO₂ and 0.05 wt.% PEO:ZTO based devices were decreased by ~ 4 % as compared to its original efficiency (7.51 to 7.20 % and 8.10 to 7.75 % for PEO:TiO₂ and 0.05 wt.% PEO:ZTO respectively). This clearly shows PEO modified TiO₂ and ZTO based devices exhibit good stability.

4.3.4 Structural and Morphological Properties of PEO modified TiO₂ and Zn doped TiO₂

To investigate the effect of PEO modification on surface defects of TiO₂ films, photoluminescence (PL) spectra were recorded for various PEO modified TiO₂ films and are as shown in Figure 4.22 (a)

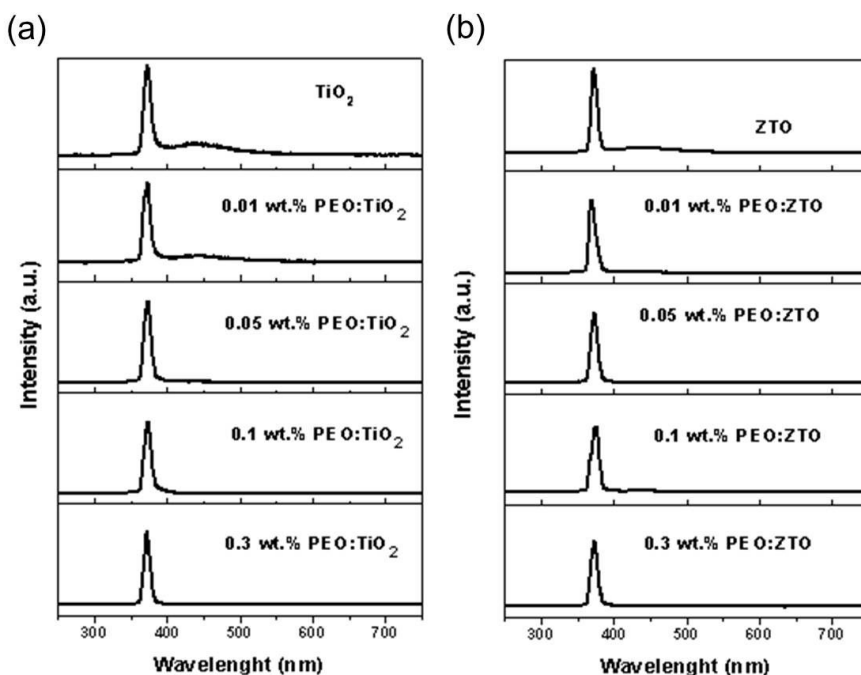


Figure 4.22 PL spectra of (a) TiO₂, PEO:TiO₂ and (b) ZTO, PEO:ZTO

As can be seen, two emission peaks were observed. The narrow emission band at 372nm is attributed to radiative annihilation of excitons, while the intense broad emission around 440nm is assigned to the trap emission. It shows clearly that the defect emission is considerably restrained by surface modification of TiO_2 by PEO, indicating reduced surface traps in TiO_2 after PEO surface modification. It is proposed that PEO species coordinate with TiO_2 by sharing a lone electron pair of oxygen in the PEO backbone, which effectively passivates the surface traps of TiO_2 . The fill-up of surface electron traps of TiO_2 favors the improvement in the conductivity of TiO_2 interlayer, leading to the reduced R_s of the devices. Moreover, the reduction of traps can decrease the possibility of trap-assisted interfacial recombination of carriers and consequently increase the R_{sh} of devices. Both reasons contribute to the improved J_{sc} and FF for the PEO modified TiO_2 based devices when the PEO concentration is less than 0.3 wt.%. Figure 4.22 (b) shows the PL spectra of PEO:ZTO films. Similar variation in the PL spectra of PEO: ZTO films was observed as previous PEO: TiO_2 films.

Another factor influencing the performance of these devices is the interfacial morphology properties. The surface roughness of the TiO_2 , PEO: TiO_2 , ZTO and PEO:ZTO films were investigated by atomic force microscopy (AFM). As shown in Figure 4.23, the root-mean-square (RMS) surface roughness is found to be 0.34 nm and 2.80 nm for TiO_2 and 0.05 wt.% PEO: TiO_2 respectively. As can be seen from Figure 4.24, uniform ZTO and 0.05 wt.% PEO:ZTO films composed of small grains are observed. The surface roughness is found to be 0.22 nm and 0.41 nm for ZTO and 0.05 wt.% PEO:ZTO respectively. However, when the PEO concentration is further increased to 0.3 wt.%, a rough surface is observed in the TiO_2 and ZTO films. The variation in surface morphology may be due to the change in the surface property of TiO_2 and ZTO films after PEO modification.

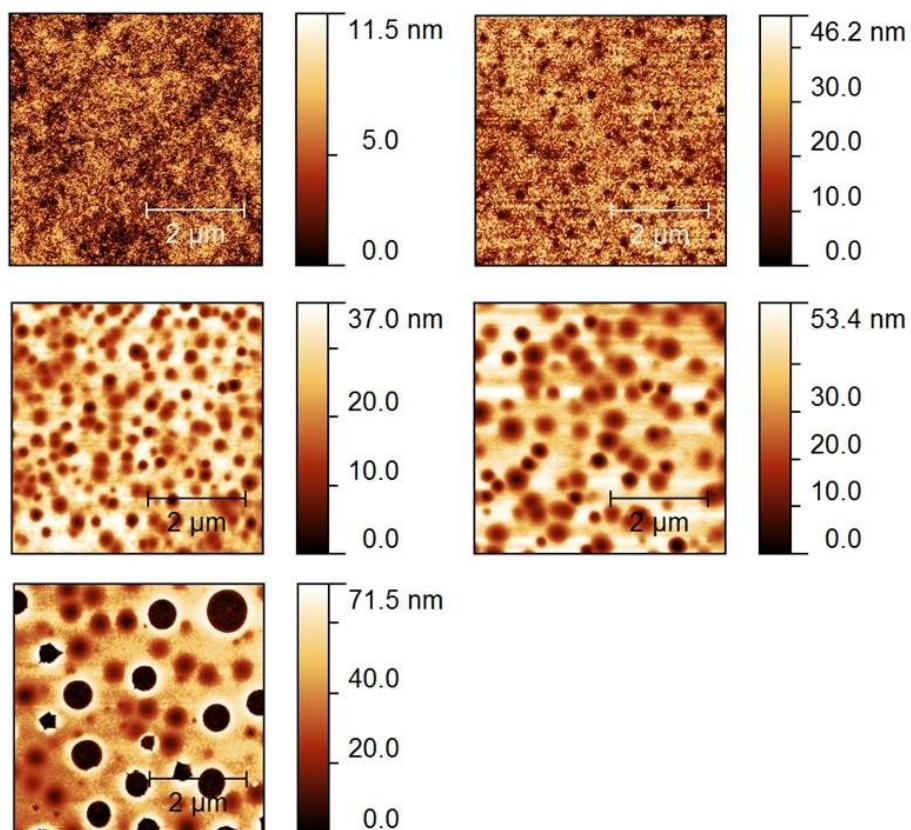


Figure 4.23 AFM images of (a) TiO_2 (b) 0.01 wt.% PEO: TiO_2 (c) 0.05 wt.% PEO: TiO_2 (d) 0.1 wt.% PEO: TiO_2 (e) 0.3 wt.% PEO: TiO_2

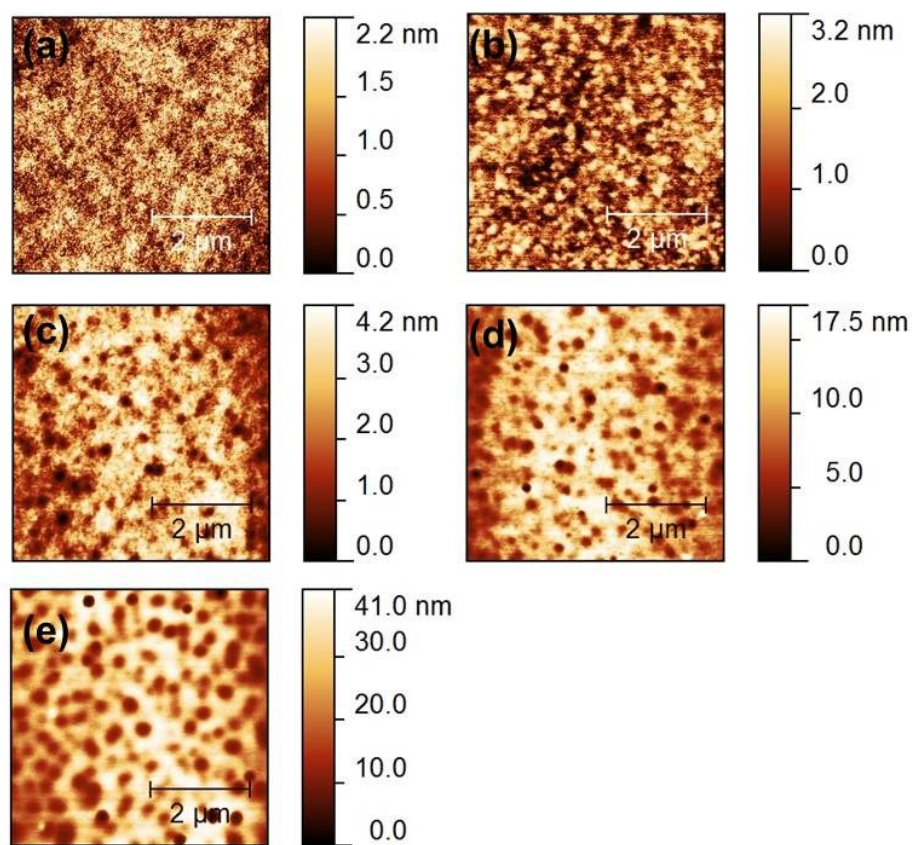


Figure 4.24 AFM images of (a) ZTO (b) 0.01 wt.% PEO:ZTO (c) 0.05 wt.% PEO:ZTO (d) 0.1 wt.% PEO:ZTO (e) 0.3 wt.% PEO:ZTO

4.4 Summary

Inverted polymer solar cells containing TiO_2 and metal (Al, In, Ga, Sn and Zn) doped TiO_2 as an electron extraction layer with the structure of ITO/ TiO_2 or doped TiO_2 / PTB7:PC₇₀BM / MoO_3 / Al were fabricated. The power conversion efficiency of inverted polymer solar cells with Al, In, Ga, Sn and Zn doped TiO_2 (1 at.% doping) are 7.59 ~ 7.87 %, which is higher than that of TiO_2 based device (6.70 %). At 1 at.% doping condition, the dopant and TiO_2 were appropriate combined, which formed the good electron extraction path. The 1 at.% metal doped TiO_2 layer exhibits lower R_s and higher R_{sh} , which attributed to less shunt loss and interfacial charge recombination and hence has better photovoltaic performance. However The PCE of 7.87 % (Zn doped TiO_2) is still low as compared to doped ZnO or IGZO based devices (in the chapter 3). These results are because the electrical properties of TiO_2 such as mobility and conductivity are lower than ZnO. So, in order to improved power conversion efficiency of TiO_2 based devices, we applied PEO modified TiO_2 and Zn doped TiO_2 (ZTO). It is found that PEO modification to the TiO_2 or ZTO film surface can effectively passivate the surface traps present in TiO_2 or ZTO, and suppress the recombination loss of carriers, reduce the series resistance and improve the electrical coupling of TiO_2 /active layer or ZTO/active layer. For PEO: TiO_2 and PEO:ZTO based inverted polymer solar cells, the power conversion efficiencies are significantly improved from the reference 6.98% and 7.51% to 7.67% and 8.10%.

Chapter 5

Conclusion

In this thesis, we have been systematically studied about the effect of doping of metal oxide as an electron extraction layer in the inverted polymer solar cells. The doped metal oxide thin films have been synthesized and deposited by the sol-gel spin coating method. The solar cells were constructed with different polymer as an electron doner such as PCDTBT, PTB7, PTB7-Th and PC₇₀BM as an electron acceptor.

At first, the effect of indium doped zinc oxide (In doped ZnO), aluminum doped zinc oxide (Al doped ZnO), gallium doped zinc oxide (Ga doped ZnO) and amorphous indium gallium zinc oxide (IGZO) on the structural, morphological, optical and electrical properties have been systematically investigated. The grain size and surface roughness values of the doped ZnO thin films are observed to be smaller and electrical properties of doped ZnO were higher than those of the pristine ZnO thin films. The Inverted polymer solar cells with 6.74 at.% In doped ZnO, 5.83 at.% Al doped ZnO, 5.03 at.% Ga doped ZnO films and IGZO (1:1:2.5 with the ratio of In:Ga:Zn) as an electron extraction layer show the high efficiency of 8.53 %, 8.67 %, 8.72 % and 9.60 % based on PTB7-Th:PC₇₀BM active layer. These power conversion efficiencies are 25 ~ 35 % improved values as compared to the inverted

polymer solar cell with pristine ZnO as an electron extraction layer. The improvement of power conversion efficiency may attributed to the enhanced optical, morphological and electrical properties. Moreover, the injection impedance values and activation energy of In, Al, Ga doped ZnO and IGZO were lower than those of pristine ZnO, which indicates that the charge carriers efficiently extracted to the electrode without large recombination and reduced trap states between the interfacial layer and active layer.

We also studied the effect of metal (Al, In, Ga, Sn and Zn) doped titanium dioxide (doped TiO₂) on the structural, morphological, optical and electrical properties and have been fabricated inverted polymer solar cells based on PTB7:PC₇₀BM. The power conversion efficiency of inverted polymer solar cells with doped TiO₂ is 7.6 ~ 7.8 % at 1 at.% doping concentration, which is higher than that of pristine TiO₂ based device (6.70 %). The doped TiO₂ layer exhibits less shunt loss and interfacial charge recombination and hence has better photovoltaic performance. In order to enhance the power conversion efficiency more, we report about the development of a generally applicable electron extraction layer by polyethylene oxide (PEO) modification to the TiO₂ and Zn doped TiO₂ surface. It is found that PEO modification to the TiO₂ or Zn doped TiO₂ film surface can effectively passivated the surface traps present in TiO₂ or Zn doped TiO₂, and suppress the recombination loss of carriers, reduce the series resistance and improve the electrical coupling of TiO₂/active layer or Zn doped TiO₂/active layer. For PEO modified TiO₂ and PEO modified Zn doped TiO₂ based inverted polymer solar cells, the power conversion efficiencies are significantly improved from the reference 6.98% and 7.51% to 7.67% and 8.10%.

This approach is believed that could be applied not only other polymer:fullerene bulk hetrojunction solar cells but also other kinds of solar cells

such as polymer-NC hybrid solar cells, perovskite solar cells and other kind of optoelectronic devices.

Bibilography

- [1] M. J. Ring, D. Lindner, E. F. Cross *et al.*, “Causes of the Global Warming Observed since the 19th Century”, *Atmospheric and Climate Sciences*, Vol. 2, no. 4, pp. 401-415, 2012
- [2] C. N. Hoth, P. Schilinsky, S. A. Choulis *et al.*, “Printing Highly Efficient Organic Solar Cells”, *Nano Lett*, Vol. 8, no. 9, pp. 2806-2813, 2008
- [3] S. E. Shaheen, R. Radspinner, N. Peyghambarian *et al.*, “Fabrication of bulk heterojunction plastic solar cells by screen printing”, *Appl. Phys. Lett*, Vol. 79, no. 18, pp. 2996-2998, 2001
- [4] C. J. Brabec, N. S. Sariciftci and J. C. Hummelen “Plastic Solar Cells”, *Adv. Funct. Mater*, Vol. 11, no. 1, pp. 15-26, 2001
- [5] J. You, L. Dou, K. Yoshimura *et al.*, “A polymer tandem solar cell with 10.6% power conversion efficiency”, *Nat. Commun*, Vol. 4, no. 1446, pp. 1-10, 2013
- [6] J. You, C. -C. Chen, Z. Hong *et al.*, “10.2% Power Conversion Efficiency Polymer Tandem Solar Cells Consisting of Two Identical Sub-Cells”, *Adv. Mater*, Vol. 25, no. 29, pp. 3973-3978, 2013
- [7] M. Jørgensen, K. Norrman, F. C. Krebs “Stability/degradation of polymer solar cells”, *Sol. Energy Mater. Sol. Cells*, Vol. 92, no. 7, pp. 686-714, 2008

- [8] A. K. K. Kyaw, X. W. Sun, C. Y. Jiang *et al.*, “An inverted organic solar cell employing a sol-gel derived ZnO electron selective layer and thermal evaporated MoO₃ hole selective layer”, *Appl. Phys. Lett*, Vol. 93, no. 22, pp. 221107-1 - 221107-3, 2008
- [9] L. -M. Chen, Z. Hong and Y. Yang “Recent Progress in Polymer Solar Cells: Manipulation of Polymer:Fullerene Morphology and the Formation of Efficient Inverted Polymer Solar Cells”, *Adv. Mater*, Vol. 21, no. 14-15, pp. 1434-1449, 2009
- [10] S. C. J. Meskers, J. K. J. van Duan and R. A. J. Janssen, “Thermally Induced Transient Absorption of Light by Poly (3,4 ethylenedioxythiophene):Poly (styrene sulfonic acid) (PEDOT:PSS) Films : A Way to Probe Charge-Carrier Thermalization Processes”, *Adv. Funct. Mater*, Vol. 13, no. 10, pp. 805-810, 2003
- [11] Y. -H. Kim, S. -H. Lee, J. Noh *et al.*, “Performance and stability of electroluminescent device with self-assembled layers of poly (3,4 ethylenedioxythiophene) - poly (styrenesulfonate) and polyelectrolytes”, *Thin Solid Films*, Vol. 510, no. 1-2, pp. 305-310, 2006
- [12] V. Shrotriya, G. Li, Y. Yan *et al.*, “Transition metal oxides as the buffer layer for polymer photovoltaic cells”, *Appl. Phys. Lett*, Vol. 88, no. 7, pp. 073508-1 - 073508-3, 2006
- [13] M. D. Irwin, D. B. Buchholz, A. W. Hains *et al.*, “p-Type semiconducting nickel oxide as an efficiency-enhancing anode interfacial layer in polymer bulk-heterojunction solar cells”, *P. Natl. Acad. Sci. USA*, Vol. 105, no. 8, pp. 2783-2787, 2008
- [14] S. -I. Na, D. -W. Park, S. -S. Kim *et al.*, “ITO-free flexible polymer solar cells with ink-jet-printed Ag grids”, *Semicond. Sci. Technol*, Vol. 27, no. 12, pp. 125002, 2012

- [15] Y. Sahin, S. Alem, R. de Bettignies *et al.*, “Development of air stable polymer solar cells using an inverted gold on top anode structure”, *Thin Solid Films*, Vol. 476, no. 2, pp. 340-343, 2005
- [16] G. Li, C. -W. Chu, V. Shrotriya *et al.*, “Efficient inverted polymer solar cells”, *Appl. Phys. Lett*, Vol. 88, no. 25, pp. 253503-1 - 253503-3, 2006
- [17] H. -H. Liao, L. -M. Chen, Z. Mu *et al.*, “Highly efficient inverted polymer solar cell by low temperature annealing of Cs_2CO_3 interlayer”, *Appl. Phys. Lett*, Vol. 92, no. 17, pp. 173303-1 - 173303-3, 2008
- [18] Z. Xu, L. -M. Chen, G. Yang *et al.*, “Vertical Phase Separation in Poly(3-hexylthiophene): Fullerene Derivative Blends and its Advantage for Inverted Structure Solar Cells”, *Adv. Funct. Mater*, Vol. 12, no. 8, pp. 1227-1234, 2009
- [19] J. Y. Kim, S. H. Kim, H. -H. Lee *et al.*, “New Architecture for High-Efficiency Polymer Photovoltaic Cells Using Solution-Based Titanium Oxide as an Optical Spacer”, *Adv. Mater*, Vol. 18, no. 5, pp. 572-576, 2006
- [20] C. Waldauf, M. Morana, P. Denk *et al.*, “Highly efficient inverted organic photovoltaics using solution based titanium oxide as electron selective contact”, *Appl. Phys. Lett*, Vol. 89, no. 23, pp. 233517-1 - 233517-3, 2006
- [21] C. S. Kim, S. S. Lee, E. D. Gomez *et al.*, “Transient photovoltaic behavior of air-stable, inverted organic solar cells with solution-processed electron transport layer”, *Appl. Phys. Lett*, Vol. 94, no. 11, pp. 113302-1 - 113302-3, 2009
- [22] C. Tao, S. Ruan, X. Zhang *et al.*, “Performance improvement of inverted polymer solar cells with different top electrodes by introducing a MoO_3 buffer layer”, *Appl. Phys. Lett*, Vol. 93, no. 19, pp. 193307-1 - 193307-3, 2008
- [23] J. Gilot, L. Barbu, M. M. Wienk *et al.*, “The use of ZnO as optical spacer in polymer solar cells: Theoretical and experimental study”, *Appl. Phys. Lett*, Vol. 91, no. 11, pp. 113520-1 - 113520-3, 2007

- [24] S. K. Hau, H. -L. Yip, N. S. Baek *et al.*, “Air-stable inverted flexible polymer solar cells using zinc oxide nanoparticles as an electron selective layer”, *Appl. Phys. Lett*, Vol. 92, no. 25, pp. 253301-1 - 253301-3, 2008
- [25] P. de Bruyn, D. J. D. Moet and P. W. M. Blom “A facile route to inverted polymer solar cells using a precursor based zinc oxide electron transport layer”, *Org. Electron*, Vol. 11, no. 8, pp. 1419-1422, 2010
- [26] Y. Sun, J. H. Seo, C. J. Takacs *et al.*, “Inverted Polymer Solar Cells Integrated with a Low- Temperature-Annealed Sol-Gel-Derived ZnO Film as an Electron Transport Layer”, *Adv. Mater*, Vol. 23, no. 14, pp1679-1683, 2011
- [27] B. -Y. Yu, A. Tsai, S. -P. Tsai *et al.*, “Efficient inverted solar cells using TiO₂ nanotube arrays”, *Nanotechnology*, Vol. 19, no. 25, pp255202, 2008
- [28] S. K. Hau, H. -L. Yip, O. Acton *et al.*, “Interfacial modification to improve inverted polymer solar cells”, *J. Mater. Chem*, Vol. 18, no. 42, pp 5113-5119, 2008
- [29] H. -L. Yip, S. K. Hau, N. S. Beak *et al.*, “Polymer Solar Cells That Use Self-Assembled-Monolayer- Modified ZnO/Metals as Cathodes”, *Adv. Mater*, Vol. 20, no. 12, pp 2376-2382, 2008
- [30] Z. He, C. Zhong, S. Su *et al.*, “Enhanced power-conversion efficiency in polymer solar cells using an inverted device structure”, *Nat. Photon*, Vol. 6, no. 9, pp 591-595, 2012
- [31] T. Yang, M. Wang, C. Duan *et al.*, “Inverted polymer solar cells with 8.4% efficiency by conjugated polyelectrolyte”, *Energy Environ. Sci*, Vol. 8, no. 8, pp 8208-8214, 2012
- [32] S. M. Yoon, S. J. Lou, S. Loser *et al.*, “Fluorinated Copper Phthalocyanine Nanowires for Enhancing Interfacial Electron Transport in Organic Solar”, *Nano. Lett*, Vol. 12, no. 12, pp 6315-6321, 2012

- [33] D. C. Lim, K. -D. Kim, S. -Y. Park *et al.*, “Towards fabrication of high-performing organic photovoltaics: new donorpolymer, atomic layer deposited thin buffer layer and plasmonic effects”, *Energy Environ. Sci*, Vol. 5, no. 12, pp 9803-9807, 2012
- [34] C. -S. Kao, F. -C. Chen, C. -W. Liao *et al.*, “Plasmonic-enhanced performance for polymer solar cells prepared with inverted structures”, *Appl. Phys. Lett*, Vol. 101, no. 19, pp. 193902-1 - 193902-4, 2012
- [35] J. Wang, Y. -J. Lee, A. S. Chadha *et al.*, “Effect of Plasmonic Au Nanoparticles on Inverted Organic Solar Cell Performance”, *J. Phys. Chem. C*, Vol. 117, no. 1, pp. 85-91, 2013
- [36] D. Zhang, W. C. H. Choy, F. Xie *et al.*, “Plasmonic Electrically Functionalized TiO₂ for High- Performance Organic Solar Cells”, *Adv. Funct. Mater. C*, Vol. 23, no. 34, pp. 4255-4261, 2013
- [37] M. N. Kamalasanan, S. Chandra, “Sol-gel synthesis of ZnO thin films”, *Thin Solid Films*, Vol. 288, no. 1-2, pp. 112-115, 1996
- [38] Q. -B. Ma, Z. -Z. Ye, H. -P. He *et al.*, “Substrate temperature dependence of the properties of Gadoped ZnO films deposited by DC reactive magnetron sputtering”, *Vacuum*, Vol. 82, no. 1, pp. 9-14, 2007
- [39] M. Wang, K. E. Lee, S. H. Hahn *et al.*, “Optical and photoluminescent properties of sol-gel Al-doped ZnO thin films”, *Mater. Lett*, Vol. 61, no. 4-5, pp. 1118-1121, 2007
- [40] V. Shelke, M. P. Bhole and D. S. Patil, “Open air annealing effect on the electrical and optical properties of tin doped ZnO nanostructure”, *Solid. State. Sci*, Vol. 14, no. 6, pp. 705-710, 2012

- [41] B. Panigrahy, M. Aslam and D. Bahadur, "Effect of Fe doping concentration on optical and magnetic properties of ZnO nanorods", *Nanotechnology*, Vol. 23, no. 11, pp. 115601, 2012
- [42] P. K. Nayak, J. Jang, C. Lee *et al.*, "Effects of Li doping on the performance and environmental stability of solution processed ZnO thin film transistors", *Appl. Phys. Lett*, Vol. 95, no. 6, pp. 193503-1 - 193503-3, 2009
- [43] S. Y. Park, B. J. Kim, K. Kim *et al.*, "Low-Temperature, Solution-Processed and Alkali Metal Doped ZnO for High-Performance Thin-Film Transistors", *Adv. Mater*, Vol. 24, no. 6, pp. 834-838, 2012
- [44] J. -H. Park, K. -J. Ahn, S. -I. Na *et al.*, "Effects of deposition temperature on characteristics of Ga-doped ZnO film prepared by highly efficient cylindrical rotating magnetron sputtering for organic solar cells", *Sol. Energy Mater. Sol. Cells*, Vol. 95, no. 2, pp. 657-663, 2011
- [45] k. -T. Hung, H. -T. Wu, S. -W. Fu *et al.*, "Improving efficiency of organic solar cells by preparing aluminum-doped zinc oxide films by ion beam-assisted sputtering", *Org. Electron*, Vol. 14, no. 1, pp. 182-186, 2013
- [46] H. W. Choi. K. -S. Lee. N. D. Theodore *et al.*, "Improved performance of ZnO nanostructured bulk heterojunction organic solar cells with nano wire-density modified by yttrium chloride introduction into solution", *Sol. Energy Mater. Sol. Cells*, Vol. 95, pp. 173-278, 2013
- [47] P. K. Nayak, J. Yang, J. Kim *et al.*, "Spin-coated Ga-doped ZnO transparent conducting thin films for organic light-emitting diodes", *J. Phys. D: Appl. Phys*, Vol. 42, no. 13, pp. 035102, 2009
- [48] A. Puetz, T. Stubhan, M. Reinhard *et al.*, "Organic solar cells incorporating buffer layers from indium doped zinc oxide nanoparticles", *Sol. Energy Mater. Sol. Cells*, Vol. 95, no. 2, pp. 579-585, 2011

- [49] T. Stubhan, H. Oh, L. Pinna *et al.*, “Inverted organic solar cells using a solution processed aluminum-doped zinc oxide buffer layer”, *Org. Electron*, Vol. 12, no. 9, pp1539-1543, 2011
- [50] A. K. K. Kyaw, Y. Wang, D. W. Zhao *et al.*, “The properties of sol–gel processed indium-doped zinc oxide semiconductor film and its application in organic solar cells”, *Phys. Status Solidi A*, Vol. 208, no. 11, pp 2635-2642, 2011
- [51] T. Stubhan, M. Salinas, A. Ebel *et al.*, “Increasing the Fill Factor of Inverted P3HT:PCBM Solar Cells Through Surface Modification of Al-Doped ZnO via Phosphonic Acid-Anchored C₆₀ SAMs”, *Adv. Energy Mater*, Vol. 2, no. 5, pp 532-535, 2012
- [52] K. -S. Shin, K. -H. Lee, H. H. Lee *et al.*, “Enhanced Power Conversion Efficiency of Inverted Organic Solar Cells with a Ga-Doped ZnO Nanostructured Thin Film Prepared Using Aqueous Solution”, *J. Phys. Chem. C*, Vol. 114, no. 37, pp 15782-15785, 2010
- [53] Y. Zhang, H. Zhou, J. Seifter *et al.*, “Molecular Doping Enhances Photoconductivity in Polymer Bulk Heterojunction Solar Cells”, *Adv. Mater*, Vol. 25, No. 48, pp. 7038-7044, 2013
- [54] Z. He, C. Zhong, S. Su *et al.*, “Enhanced power-conversion efficiency in polymer solar cells using an inverted device structure”, *Nat. Photonics*, Vol. 6, No. 20, pp. 591-595, 2012
- [55] S. -H. Liao, H. -J. Jhuo, Y. -S. Cheng *et al.*, “Fullerene Derivative-Doped Zinc Oxide Nanofilm as the Cathode of Inverted Polymer Solar Cells with Low-Bandgap Polymer (PTB7-Th) for High Performance”, *Adv. Mater*, Vol. 25, No. 34, pp. 4766-4771, 2013

- [56] J. Y. Kim, S. Noh, D. Lee *et al.*, “Solution-Processable Zinc Oxide for the Polymer Solar Cell Based on P3HT:PCBM”, *J. Nanosci. Nanotechnol*, Vol. 11, No. 7, pp. 5995-6000, 2011
- [57] S. Bai, Z. Wu, X. Xu *et al.*, “Inverted organic solar cells based on aqueous processed ZnO interlayers at low temperature”, *Appl. Phys. Lett*, Vol. 100, No. 7, pp. 203906-1 - 203906-4, 2012
- [58] K. Lee, J. Y. Kim, S. H. Park *et al.*, “Air-Stable Polymer Electronic Devices”, *Adv. Mater*, Vol. 19, No. 18, pp. 2445 -2449, 2007
- [59] S. K. Hau, H. -L. Yip, H. Ma *et al.*, “High performance ambient processed inverted polymer solar cells through interfacial modification with a fullerene self-assembled monolayer”, *Appl. Phys. Lett*, Vol. 93, No. 23, pp. 233304 -1 - 233304-3, 2008
- [60] N. Zhou, X. Guo, R. Ponce *et al.*, “Bithiophene Imide and Benzodithiophene Copolymers for Efficient Inverted Polymer Solar Cells”, *Adv. Mater*, Vol. 24, No. 17, pp. 2242-2248, 2012
- [61] H. Karaagac, E. Yengel and M. S. Islam, “Physical properties and heterojunction device demonstration of aluminum-doped ZnO thin films synthesized at room ambient via sol–gel method”, *J. Alloys Compd*, Vol. 521, No. 25, pp. 155-162, 2012
- [62] A. Puetz, T. Stubhan, M. Reinhard *et al.*, “Organic solar cells incorporating buffer layers from indium doped zinc oxide nanoparticles” *Sol. Energy Mater. Sol. Cells*, Vol. 95, No. 2, pp. 579-585, 2011
- [63] A. P. Rambu, N. Iftimie and V. Nica “Effect of In incorporation on the structural, electrical, and gas sensing properties of ZnO films” *J. Mater. Sci*, Vol. 47, No. 19, pp. 6979-6985, 2012

- [64] R. Yousefi, F. J. Sheini, A. K. Zak *et al.*, “Effect of indium concentration on morphology and optical properties of In-doped ZnO nanostructures” *Ceram. Inter.*, Vol. 38, No. 8, pp. 6295-6301, 2012
- [65] A. Tubtimtae and M. -W. Lee “ZnO nanorods on undoped and indium-doped ZnO thin films as a TCO layer on nonconductive glass for dye sensitized solar cells” *Superlattices Microstruct.*, Vol. 52, No. 5, pp. 987-996, 2012
- [66] T. Ratana, P. Amompitoksuk, T. Ratana *et al.*, “The wide band gap of highly oriented nanocrystalline Al doped ZnO thin films from sol–gel dip coating” *J Alloys Compd.*, Vol. 470, No. 1-2, pp. 408-412, 2009
- [67] E. Burstein “Anomalous Optical Absorption Limit in InSb” *Physiol Rev.*, Vol. 93, No. 3, pp. 632-633, 1954
- [68] T. S. Moss “The Interpretation of the Properties of Indium Antimonide” *Proc. Phys. Soc. B.*, Vol. 67, No. 10, pp. 775-782, 1954
- [69] Q. Wang, Y. Yang, H. He *et al.*, “One-Step Synthesis of Monodisperse In-Doped ZnO Nanocrystals” *Nanoscale. Res. Lett.*, Vol. 5, No. 5, pp. 882-888, 2010
- [70] Y. R. Park, D. Jung, K. -C. Kim *et al.*, “Physical properties of transparent conducting indium doped zinc oxide thin films deposited by pulsed DC magnetron sputtering” *J. Electroceram.*, Vol. 23, No. 2-4, pp. 536-541, 2009
- [71] S. S. Shinde, P. S. Shinde, C. H. Bhosale *et al.*, “Optoelectronic properties of sprayed transparent and conducting indium doped zinc oxide thin films” *J. Phys. D: Appl. Phys.*, Vol. 41, No. 10, pp. 1-6, 2008
- [72] Z. Zhang, C. Bao, W. Yao *et al.*, “Influence of deposition temperature on the crystallinity of Al-doped ZnO thin films at glass substrates prepared by RF magnetron sputtering method” *Superlattices Microstruct.*, Vol. 49, No. 6, pp. 644-653, 2011

- [73] Z. Q. Xu, H. Deng, Y. Li *et al.*, “Characteristics of Al-doped c-axis orientation ZnO thin films prepared by the sol–gel method” *Mater. Res. Bull.*, Vol. 41, No. 2, pp. 356-358, 2006
- [74] Y. Caglar, M. Caglar and S. Ilcan “Microstructural, optical and electrical studies on sol gel derived ZnO and ZnO:Al films” *Curr. Appl. Phys.*, Vol. 12, No. 3, pp. 963-968, 2012
- [75] G. Kresse and J. Hafner “Ab initio molecular dynamics for liquid metals” *Phy. Rev. B*, Vol. 47, No. 1, pp. 558-561, 1993
- [76] P. E. Blöchl “Projector augmented-wave method” *Phy. Rev. B*, Vol. 50, No. 24, pp. 17953-17979, 1994
- [77] J. P. Perdew, K. Burke and M. Ernzerhof “Generalized Gradient Approximation Made Simple” *Phy. Rev. Lett.*, Vol. 77, No. 18, pp. 3865-3868, 1996
- [78] P. Palacios, K. Sánchez and P. Wahnón *et al.*, “Ab-initio valence band spectra of Al, In doped ZnO” *Thin Solid Films*, Vol. 517, No. 7, pp. 2448-2451, 2009
- [79] A. Kalaivanan, S. perumal, N. Pillai *et al.*, “Characteristics of Gallium Doped ZnO Thin Films Deposited by Sol Gel Dip Coating” *ECS. Trans.*, Vol. 19, No. 27, pp. 65-70, 2009
- [80] J. K. Kim, S. J. Yun, J. M. Lee *et al.*, “Effect of rf-power density on the resistivity of Ga-doped ZnO film deposited by rf-magnetron sputter deposition technique” *Curr. Appl. Phys.*, Vol. 10, No. 3, pp. S451-S454, 2010
- [81] G. H. Lee, Y. Yamamoto, M. Kourogi *et al.*, “Blue shift in room temperature photoluminescence from photo-chemical vapor deposited ZnO films” *Thin Solid Films*, Vol. 386, No. 1, pp. 117-120, 2001
- [82] S. -W. Yoon, J. -H. Seo, T. -Y. Seong *et al.*, “Ga Ordering and Electrical Conductivity in Nanotwin and Superlattice-Structured Ga-Doped ZnO” *Cryst. Growth Des.*, Vol. 12, No. 3, pp. 1167-1172, 2012

- [83] B. Joseph, P. K. Manoj, V. K. Vaidyan, "Studies on the structural, electrical and optical properties of Al-doped ZnO thin films prepared by chemical spray deposition" *Ceram. Int*, Vol. 32, No. 5, pp. 487-493, 2006
- [84] Y. -D. Ko, K. -C. Kim, Y. -S. Kim, "Effects of substrate temperature on the Ga-doped ZnO films as an anode material of organic light emitting diodes" *Superlattices Microstruct*, Vol. 51, No. 6, pp. 933-941, 2012
- [85] P. K. Nayak, T. Busani, E. Elamurugu *et al.*, "Zinc concentration dependence study of solution processed amorphous indium gallium zinc oxide thin film transistors using high-k dielectric" *Appl. Phys. Lett*, Vol. 97, No. 18, pp. 183504-1 - 183504-3, 2010
- [86] Y. -H. Yang, S. S. Yang, C. -Y. Kao *et al.*, "Chemical and Electrical Properties of Low-Temperature Solution-Processed In-Ga-Zn-O Thin-Film Transistors" *IEEE Electron Dev. Lett*, Vol. 31, No. 4, pp. 329-331, 2010
- [87] J. H. Choi, S. M. Hwang, C. M. Lee *et al.*, "Effect of Ga content and sintering time on electrical properties of InGaZnO thin film transistors fabricated by sol-gel process" *J. Cryst. Growth*, Vol. 326, No. 1, pp. 175-178, 2011
- [88] G. H. Kim, W. H. Jeong, H. J. Kim "Electrical characteristics of solution-processed InGaZnO thin film transistors depending on Ga concentration" *Phys. Status Solidi A*, Vol. 207, No. 7, pp. 1677-1679, 2010
- [89] M. Meier, S. Karg and W. Riess, "Light-emitting diodes based on poly-p-phenylene-vinylene: II. Impedance spectroscopy" *J. Appl. Phys*, Vol. 82, No. 4, pp. 1961 - 1966, 1997
- [90] C. K. Suman, S. Noh, S. Kim *et al.*, "Electrical Impedance Studies of the Effect of a Buffer Layer on Organic Bulk Hetrojunction Solar Cells" *J. Korean. Phys. Soc*, Vol. 53, No. 6, pp. 3278 - 3282, 2008

- [91] I. Riedel and V. Dyakonov, "Influence of electronic transport properties of polymer-fullerene blends on the performance of bulk heterojunction photovoltaic devices" *Phys. Stat. Sol.*, Vol. 201, No. 6, pp. 1332 - 1341, 2004
- [92] P. Schilinsky, C. Waldauf and C. J. Brabec, "Recombination and loss analysis in polythiophene based bulk heterojunction photodetectors " *Appl. Phys. Lett.*, Vol. 81, No. 20, pp. 3885 - 3887, 2002
- [93] L. J. A. Koster, V. D. Mihailetschi, H. Xie *et al.*, "Origin of the light intensity dependence of the short-circuit current of polymer/fullerene solar cells" *Appl. Phys. Lett.*, Vol. 87, No. 20, pp. 203502-1 - 203502-3, 2005
- [94] D. Chirvase, Z. Chiguvare, M. Knipper *et al.*, "Temperature dependent characteristics of poly,,(3 hexylthiophene) - fullerene based heterojunction organic solar cells" *J. Appl. Phys.*, Vol. 93, No. 6, pp. 3376 - 3383, 2003
- [95] G. Garcia-Belmonte, "Temperature dependence of open-circuit voltage in organic solar cells from generation–recombination kinetic balance" *Sol. Energy Mater. Sol. Cells*, Vol. 94, No. 12, pp. 2166 - 2169, 2010
- [96] C. Voz, J. Puigdollers, J. M. Asensi, *et al.*, "Analysis of the dynamic short-circuit resistance in organic bulk-heterojunction solar cells: relation to the charge carrier collection efficiency," *Organic Electronics*, Vol. 14, No. 6, pp.1643-1648, 2013.
- [97] C. Hof, N. Wyrsh and A. Shah, "Influence of Electrical Field Distortion and i-layer Quality on the Collection Function of Drift-driven a-Si:H Solar Cells," *J. Non-Crystalline Solids*, vol. 266-269, No. pp.1114-1118, 2000
- [98] J. Zhang, W. Peng, Z. Chen *et al.*, "Energy band tunable $\text{Ti}_x\text{Sn}_{1-x}\text{O}_2$ photoanode for efficient non-TiO₂ type dye sensitized solar cells" *J. Mater. Chem. A*, Vol. 1, No. 29, pp. 8453-8463, 2013

[99] S. Ponia, S. Sathasivam, N. Chadwick *et al.*, “Aerosol assisted chemical vapour deposition of hydrophobic $\text{TiO}_2\text{--SnO}_2$ composite film with novel microstructure and enhanced photocatalytic activity” *J. Mater. Chem. A*, Vol. 1, No. 20, pp. 6271-6278, 2013

Publication

[1] International Journals

1. D. Lee, J. Park, S. Noh, **J. Y. Kim**, S. Lee and C. Lee, “Effect of Solution Processed Salt Layers on the Device Performances of Polymer Solar Cells,” *Thin Solid films*. Vol. 518, no. 2, pp. 541-544, 2009.
2. **J. Y. Kim**, S. Noh, D. Lee and C. Lee “Organic Tandem Solar Cell Using a Semi-transparent Top Electrode for Both-side Light Absorption”, *J. Korean Phys. Soc.* Vol. 57, no. 6, pp. 1852-1855, 2010.
3. Y. Park, S. Noh, D. Lee, **J. Y. Kim** and C. Lee “Study of the Cesium Carbonate (Cs_2CO_3) Inter Layer Fabricated by Solution Process on P3HT:PCBM Solar Cells”, *Mol. Cryst. Liq. Cryst.* Vol. 538, no. 1, pp. 20-27, 2011.
4. **J. Y. Kim**, S. Noh, D. Lee, P. K. Nayak, Y. Hong and C. Lee “Solution-Processable Zinc Oxide for the Polymer Solar Cell Based on P3HT:PCBM”, *J. Nanosci. Nanotechnol.* Vol. 11, no. 7, pp. 5995-6000, 2011.
5. Y. Park, S. Noh, D. Lee, **J. Y. Kim** and C. Lee “Temperature and Light Intensity Dependence of Polymer Solar Cells with MoO_3 and PEDOT:PSS as a

- Buffer Layer”, *J. Korean Phys. Soc.* Vol. 59, no. 2, pp. 362-366, 2011.
6. S. Noh, D. Lee, **J. Y. Kim**, Y. Park, C. Lee and J. J. Amsden “Area and Light Intensity Dependence of Buffer Layers on P3HT:PCBM Solar Cells”, *J. Korean Phys. Soc.* Vol. 59, no. 2, pp. L207-L210, 2011.
 7. J. Y. Kim, S. Noh, Y. M. Nam, **J. Y. Kim**, J. Roh, M. Park, J. J. Amsden, D. Y. Yoon, C. Lee and W. H. Jo “Effect of Nanoscale SubPc Interfacial Layer on the Performance of Inverted Polymer Solar Cells Based on P3HT/PC₇₁BM”, *ACS Appl. Mater. Interfaces*. Vol. 3, no. 11, pp. 4279-4285, 2011.
 8. H. Lee, **J. Y. Kim** and C. Lee “Improvement of Power Efficiency in Phosphorescent White Organic Light-Emitting Diodes Using p-Doped Hole Transport Layer”, *Int. J. Photoenergy*. Vol. 2012, pp. 581421, 2012.
 9. **J. Y. Kim**, J. Kwak, S. Noh and C. Lee,” Enhanced Performance of SubPC/C₆₀ Solar Cells by Annealing and Modifying Surface Morphology” *J. Nanosci. Nanotechnol.* Vol. 12, no. 7, pp. 5724-5727, 2012.
 10. **J. Y. Kim**, H. Lee, J. H. Park, D. Lee, H. -J. Song, J. Kwak, and C. Lee “Effect of Sol-Gel Derived ZnO Interfacial Layer on the Photovoltaic Properties of Polymer Solar Cell”, *Jap. J. Appl. Phys.* Vol. 51, no. 10, pp. 10NE29-1 - 10NE29-4, 2012.
 11. M. Thambidurai, N. Muthukumarasamy, D. Velauthapillai, C. Lee and **J. Y. Kim** “Synthesis of ZnO nanorods and their application in quantum dot sensitized solar cells”, *J. Sol-Gel. Sci. Technol.* Vol. 64, no. 3, pp. 750-755, 2012.
 12. **J. Y. Kim**, S. Noh, J. Kwak, and C. Lee “Analysis of Annealing Process on

- P3HT:PCBM-Based Polymer Solar Cells Using Optical and Impedance Spectroscopy”, *J. Nanosci. Nanotechnol.* Vol. 13, no. 5, pp. 3360-3364, 2013.
13. M. Thambidurai & **J. Y. Kim (co-first)**, J. Song, Y. Ko, H. -J Song, C. -M. Kang, N. Muthukumarasamy, D. Velauthapillaic and C. Lee “High performance inverted organic solar cells with solution processed Ga-doped ZnO as an interfacial electron transport layer”, *J. Mater. Chem. C*, Vol. 1, no. 48, pp. 8161-8166, 2013.
 14. H. -J. Song, **J. Y. Kim**, D. Lee, J. Song, Y. Ko, J. Kwak, and C. Lee “Origin of the Mixing Ratio Dependence of Power Conversion Efficiency in Bulk Heterojunction Organic Solar Cells with Low Donor Concentration”, *J. Nanosci. Nanotechnol.* Vol. 13, no. 12, pp. 7982-7987, 2013.
 15. M. Thambidurai, J. Y. Kim, J. Song, Y. Ko, N. Muthukumarasamy, D. Velauthapillaic and C. Lee “Nanocrystalline Ga-doped ZnO thin films for inverted polymer solar cells”, *Sol. Energy*, online publish, 2013.
 16. M. Thambidurai & **J. Y. Kim (co-first)**, C. -M. Kang, N. Muthukumarasamy, H. -J. Song, J. Song and C. Lee “Enhanced photovoltaic performance of inverted organic solar cells with In-doped ZnO as an electron extraction layer” *Renewable Energy*. Vol. 66, pp. 433-442, 2014.
 17. K. Jung, H. -J. Song, G. Lee, Y. Ko, K. Ahn, H. Choi, **J. Y. Kim**, K. Ha, S. Song, J. -K. Lee, C. Lee and M. Choi, “Plasmonic organic solar cells employing nanobump assembly via aerosol-derived nanoparticles”, *ACS Nano*, Vol. 8, no. 3, pp. 2590-2601, 2014.

[2] International Conferences

1. **J. Y. Kim**, S. Noh, D. Lee and C. Lee, “Organic tandem solar cell using semi-transparent top electrode for both side light absorption”, International Conference on Advanced Materials and Devices (ICAMD), Poster, 2009.
2. **J. Y. Kim**, P. K. Nayak, S. Noh, D. Lee, Y. Hong and C. Lee, “Zinc oxide as an optical spacer for the polymer solar cell based on P3HT:PCBM”, 2010 MRS Spring meeting, Poster HH10.27, 2010.
3. **J. Y. Kim**, S. Noh, D. Lee, P. K. Nayak, Y. Hong and C. Lee, “Solution Processible Zinc Oxide for the Polymer Solar Cell Based on P3HT:PCBM”, IEEE Nano 2010 & Joint Symposium with Nano Korea 2010, Poster, 2010.
4. **J. Y. Kim**, J. H. Park, S. Noh and C. Lee, “Enhanced Efficiency of Polymer Bulk Heterojunction Solar Cells Using Zinc Oxide Layer as an Optical Spacer”, International Conference on Electroluminescence & Organic Optoelectronics (ICEL 2010), Poster, 2010.
5. **J. Y. Kim**, J. Kwak, S. Noh and C. Lee “Enhanced Performance of SubPC/C₆₀ Solar Cells by Annealing and Modifying Surface Morphology”, Nano Korea 2011, Poster, 2011
6. **J. Y. Kim**, S. Noh, D. Lee, J. J. Amsden and C. Lee “The Effect of Post-annealing Process in Polymer Solar Cell Based on P3HT:PCBM”, International Conference on Advanced Electromaterials (ICAE), Poster, 2011.
7. **J. Y. Kim**, S. Noh, D. Lee and C. Lee “Effect of Sol-Gel Derived ZnO Interfacial Layer on the Photovoltaic Properties of Polymer Solar Cells”, 21st International Photovoltaic Science and Engineering Conference (PVSEC),

Poster, 2011.

8. **J. Y. Kim**, J. Park, D. Lee, H. -J. Song, H. J. Syn, J. Song, Y. Ko and C. Lee
“Effects of active layer thickness and thermal annealing based on PCDTBT:PCBM bulk heterojunction solar cells”, Global Photovoltaic Conference (GPVC), Poster, 2012.
9. **J. Y. Kim**, J. J. Amsden, I. Park, D. Lee, H. -Jun Song, D. Y. Yoon and C. Lee
“Temperature and Light Intensity Study of Poly(phenylene vinylene):ZnO Hybrid Bulk Hetrojunction Solar Cells with Semiconducting Surfactants”, MRS Fall meeting, Poster, 2012.
10. **J. Y. Kim**, M. Thambidurai, H. -Jun Song, D. Lee, J. Song, Y. Ko, H. J. Syn and C. Lee
“Enhanced photovoltaic performance of inverted polymer solar cells with doped ZnO interfacial layer”, The 5th International Conference on Hybrid and Organic Photovoltaics (HOPV), Oral, 2013.
11. **J. Y. Kim**, M. Thambidurai, D. Lee, H. -Jun Song, J. Song, Y. Ko, H. J. Syn and C. Lee
“Enhanced photovoltaic performance of inverted polymer solar cells with Al-doped zinc oxide interfacial layer”, 8th German-Korean Polymer Symposium, Poster, 2013.

[3] Domestic Conferences

1. **J. Y. Kim**, M. Thambidurai, H. -J. Song, Y. Ko, J. Song, H. Lee, J. H. Kim and C. Lee, “Improved Device Performance of Inverted Polymer Solar Cells with Metal-doped ZnO as an Electron Extraction Layer”, Korea Photovoltaic Society 2014, Oral, 2014.

한글 초록

역구조 형태의 고분자 태양전지는 정구조 형태의 고분자 태양전지 보다 소자의 수명 및 공기중의 안정성이 뛰어나다는 장점이 있다. 이러한 역구조 형태의 고분자 태양전지에서는 효과적인 전자 추출을 돕기 위한 전자 추출층이 반드시 사용되어야 한다. 그 중에서 산화아연, 이산화 티타늄 등의 산화물은 투명하고 전하이동도가 빠르며, 제조가 용이하고 친 환경적이기 때문에 전자 추출층으로의 적용이 용이하다. 최근에 역구조 형태의 고분자 태양전지 연구는 대부분 이러한 산화물을 전자 추출층으로 사용한 연구가 주를 이루어 보고되고 있다. 하지만 오직 이러한 산화물을 사용하는 것은, 역구조 고분자 태양전지 소자의 성능을 높이는 것에 대한 한계이다.

따라서 본 학위 논문에서는 역구조 고분자 태양전지의 성능을 높이기 위한 방법론을 제시하였다. 특히 전자 추출층으로 금속 물질이 도핑된 산화물의 사용에 초점을 맞추어 진행하였다. 금속 물질이 도핑된 산화물의 물성을 분석하고, 이를 역구조 고분자 태양전지의 전자 추출층으로 적용하였을 때에, 태양전지 특성 및 그의 상관관계에 대해서 체계적으로 분석하였다.

제 1 장에서는, 한가지 원소가 도핑된 산화아연 (인듐 도핑된 산화아연, 알루미늄 도핑된 산화아연, 갈륨 도핑된 산화아연) 그리고 두가지 원소가 도핑된 산화아연 (인듐과 갈륨 동시에 도핑된 산화아연)을 역구조 고분자 태양전지의 전자 추출층으로 사용하였다. 먼저 한가지 원소가 도핑된 산화아연의 최적화된 도핑농도를 찾기 위해서 이들에 대한 물성 분석을 (전기·광학적 특성분석, 구조적

특성 분석, 형태학적 특성분석) 진행 한 후, PCDTBT: PC₇₀BM 기반의 역구조 고분자 태양전지의 전자 추출 층으로 적용하였다. 그 결과 도핑을 함으로써 전기·광학적 특성 개선, 표면 형태학적 특성 개선 및 구조적 특성이 개선되며, 특히 5~6 at.%의 도핑 농도에서 최적의 역구조 태양전지 특성을 보였다. 태양전지의 효율을 더욱 높이기 위해서 PTB7, PTB7-Th 물질을 광활성층으로 사용한 결과, 도핑된 산화아연을 사용하는 것이 도핑되지 않은 산화아연을 사용하는 것 보다 전력변환 효율을 약 25~35% 정도 증가시킬 수 있었다. 특히 인듐과 갈륨이 동시에 도핑된 산화아연에서 전력변환효율은 9.6%를 나타내었다. 증가된 원인을 분석하기 위하여, 태양전지 소자의 온도별 (100~350 K)·빛 세기별 (1~100 mW/cm²) 전류-전압 측정으로 내부 활성화 에너지 및 재결합률을 계산하였고, 임피던스를 측정하였다. 그 결과 도핑된 산화아연을 사용하게 되면, 내부 활성화 에너지 및 재결합률을 낮출 수 있고, 전자 추출저항을 줄일 수 있다는 것을 확인하였다. 이 결과는 도핑된 산화아연을 사용하게 되면 역구조 고분자 태양전지 소자 내에서 전자 추출 특성을 크게 향상시킬 수 있다는 것을 의미합니다.

제 2 장에서는, 산화아연 대신에 이산화 티타늄을 사용하였고 도판트로는 인듐, 알루미늄, 갈륨, 주석 그리고 아연을 사용하였다. 산화 아연과는 다르게 이산화 티타늄에서는 약 ~1 at.% 의 작은 도핑농도에서 최적의 효율을 보였으며 (7.6~7.8 %), 이는 도핑되지 않은 이산화 티타늄을 사용하는 것과 대비하여 약 10% 증가된 결과이다. 도핑된 이산화 티타늄을 사용한 태양전지의 효율을 더욱

높이기 위해서 Polyethylene oxide (PEO)를 첨가한 이산화 티타늄을 적용해 보았다. PEO 를 첨가하게 되면 이산화 티타늄 내부의 트랩 에너지를 낮출 수 있으며, 이를 통해 원활한 전자 수집을 유도할 수 있다. 그 결과 8.10 %의 전력변환 효율을 나타내었다.

이상의 연구 결과는 단일 소자의 역구조 고분자 태양전지의 효율을 높이기 위한 방법론을 제시한다. 앞으로 더욱 뛰어난 고분자 물질이 개발되고 이를 기반으로 하는 역구조 태양전지를 제작할 때에, 본 연구 논문에서 제시한 전자추출층을 사용한다면 더욱 높은 효율을 지닌 태양전지를 개발 할 수 있을 것으로 기대된다. 또한 태양전지에 한정되지 않고, 유기물 및 산화물 기반의 전자 소재에도 적용될 수 있을 것으로 생각된다.

주요어: 고분자 태양전지, 역구조, 산화아연, 이산화 티타늄, 도핑, 전자 추출층, PCDTBT, PTB7, PTB7-Th, PC₇₀BM

학번: 2010-30979